ANNEALING MECHANISMS OF POINT DEFECTS IN SILICON CARBIDE

A Theoretical Investigation

Dissertation
zur Erlangung des akademischen Grades

Doktor der Naturwissenschaften (Dr. rer. nat.)

anerkannt von der Fakultät für Naturwissenschaften
der Universität Paderborn

Dipl. Phys. Eva Rauls

Paderborn, 2003

Contents

List of Figures

List of Tables

Introduction

Silicon carbide (SiC) is a very promising material in semiconductor technology. Its hardness, its high temperature stability and many other properties which will be described in Chapter 1 give it a wider range of application than silicon. As a comparably new material, there are, however, still many aspects of the material that are not fully understood and which hinder its technological breakthrough in semiconductor industry. Understanding and controlling the electronic properties of SiC is, therefore, the aim of current research in this field.

Most electronic properties of semiconductors are determined by the kind and amount of defects in the material. The surfaces of the crystal, interfaces to other materials or dislocations in the bulk material influence the electronic properties of the material as well as point defects of either intrinsic or extrinsic nature. The periodicity is broken by any kind of defect, the lattice is locally distorted, electronic states may be changed or newly induced as a consequence.

The origin of defects is manifold: the termination of a surface e. g. depends on the environmental conditions during growth or e. g. oxidation, on the concentration of each species and on the temperature. Dislocations can for example result from a lattice mismatch at the interface with another material[1].

Point defects are on the one hand unavoidably built in already during growth, on the other hand, they are intentionally brought into the material in a special procedure in order to tailor the electronic properties of the material.

For the fabrication of electronic devices, as e. g. field effect transistors, p-type and n-type material is needed. This is created by doping with elements of the neighboring groups in the periodical system. For SiC as a compound semiconductor of two group IV elements, p-type material can be created by doping with group III elements, as boron or aluminum, whereas n-type doping is achieved by implantation with group V elements, like nitrogen or phosphorus.

But also intrinsic defects like vacancies or antisites affect the electronic properties of the material, either in form of isolated defects or after complex formation with other intrinsic defects or dopant atoms.

To understand how the electronic properties depend on the outer conditions and how tailoring of the electronic properties can be done most efficiently, defect dynamics have to be investigated.

Experimental investigations alone can only supply incomplete information, and it is a promising possibility to complement them with atomistic simulations. In many cases, such simulations are, however, very costly, so that there were only few simulations in the past, which could provide information that was useful to interpret experimental data. Due to limited resources very approximative simulation schemes had to be used, and, consequently, a satisfying accuracy could often not be reached. More elaborate simulation methods, which

---

[1]This makes it, e. g., difficult to grow SiC on silicon substrate, where the ratio of 4:5 in the (110) planes causes dislocations and thereby unavoidably electrically active interface states.

can provide the desired accuracy, are first now with increasing computing capacities getting capable of supplying the results needed for the explanation of experimental observations.

This theoretical work deals with the behavior of selected point defects in SiC that can be expected to be created during implantation and annealing processes commonly used for the doping of SiC. Migration and aggregation of defects are covered with a special focus on the understanding of the experimentally observed annealing phenomena. As a method for atomistic simulations, a density-functional based tight-binding scheme has been used, which is considerably more accurate than empirical tight-binding methods, but, especially concerning the description of the electronic structure of defects, less accurate than first principle methods. Its efficiency offers the possibility of a systematic investigation of the defect dynamics, which in spite of today's computing facilities is much too time consuming for first principle methods. For more detailed investigations of selected defects, i. e. the calculation of occupation levels or hyperfine interactions, various first principle methods have been used, additionally.

Outline of this Work

In the first chapter, the investigated material, silicon carbide, is characterized. In a brief historical sketch, the fabrication of SiC and with the improvement of material quality the growing range of application is outlined. Silicon carbide's characteristic property of crystallizing in various crystal structures is discussed as well as current problems with doping SiC in order to use it as a device material.

Subject of the second chapter are the possibilities to treat such problems theoretically. Some general aspects of point defects, useful for the discussion in later chapters, are shown up in the first section. In the following sections, the computational method, its theoretical basis and algorithms for the calculation of diffusion paths or vibrational frequencies are briefly described. The last section of this chapter is dedicated to the calculation of entropies, needed for the description of high temperature processes. Various test calculations, also for silicon and diamond, are presented, here.

The third chapter summarizes the results of our calculations for formation and migration energies of vacancies and interstitials in SiC. On the one hand, some reference calculations allow a comparison of the results obtained within our method with literature data, and thus an estimate of the expectable accuracy. On the other hand, the basic processes needed in the following two chapters, i. e. the sublattice migration of vacancies and carbon split-interstitials, are discussed. Antisites and the creation of pairs and larger aggregates of them are investigated in the fourth chapter. Several mechanisms for aggregation of antisites to one-, two- or three-dimensional structures and the influence of the vibrational entropy on the activation energies for these processes are discussed.

The fifth chapter deals with the problem of n-type doping of SiC with nitrogen. Experimental observations concerning the carrier concentration in the implanted sample are tentatively explained by a split-interstitial based migration mechanism of nitrogen and the formation of inactive complexes. Also for the recovery of the saturated charge carriers we discuss an atomistic model, and finally try to correlate our calculated activation energies with annealing temperatures. A brief section points out the differences in the behavior of phosphorus and nitrogen as n-type dopant.

Chapter 1

Some Facts about Silicon Carbide

1.1 Historical Facts and Applications

In recent years, silicon carbide (SiC) has become more and more important for the semiconductor industry. This field of application is, though, certainly not what people thought of when the Swedish researcher Jöns Jacob Berzelius (see Fig. 1.1) discovered SiC in 1824 while trying to synthesize diamond. In 1891, Edward Goodrich Acheson found a possibility to synthesize SiC, melting carbon and aluminumsilicate. He named the material "Carborundum", believing it consisted of molten aluminum, which in mineralogy is called *Corundum*. When he realised that it consisted of silicon and carbon, this name had already been adopted into the language (and patented in 1893). Later on, Acheson used carbon and sand to fabricate "Carborundum" – a melting process that is still used today, though in an improved way, and known as *Acheson method*.

However, this method is due to insufficient crystal quality not used for device fabrication, but for emery, abrasives and polishing material. In metallurgy, silicon carbide is, furthermore, used for sintering or as a mean for desoxidation or alloys. In the field of ceramics, SiC is widely used because of its hardness. Today, it is used as the basis for especially high power ceramics where not only its hardness but also its high melting point is needed. Other applications of SiC are certain kinds of gaskets, heating rods, overvoltage arresters, and last but not least high temperature transistors and light emitting diodes (LEDs), just to name two of the most common applications in the electronic industry. First achievements were already made in the 1960s, and since then persistently new or improved semiconductor devices based on extremely pure SiC have been presented by industry. For these applications, an extremely good material quality is required. For this aim, a sublimation process

Figure 1.1: The ones who found SiC: J. J. Berzelius and H. Moissan

Figure 1.2: The upper picture shows three moissanite crystals (0.12 ct) in nearly colorless till light yellowish. The bottom picture shows (from left to right) a synthetic moissanite, a brilliant, and a synthetic zirkonia.[1]

invented by J.A. Lely (1955) or a modification of it (Y.M.Tairov, 1977) is employed, which results in monocrystallites with a very low defect density.

Siliconcarbide is not only a synthetical material, but occurs also (rarely) in nature. In 1904, Henry Moissan (see Fig. 1.1) found some small, dark, hexagonal crystallites next to some small diamond crystallites when investigating meteorites in Canyon Diablo, Arizona. He analyzed these crystallites as silicon carbide. As it requires extremely high temperatures to be formed, SiC has only been found in meteoritic or volcanic stone, the so called *"Kimberlit"*, in the USA, in the former CSFR, and in Sibiria. Mineralogists named the material *"Moissanite"* in honor of its discoverer. This name is still in use today, and leads us to a field of application not named so far, where this name of SiC is commonly used: jewelry.

SiC has a Mohs hardness of 9.6, that is very close to that of diamond (10), and its density is slightly lower than that of diamond. A high dispersion and refraction and a brilliance only slightly less than in diamond make grinded SiC-stones look extremely similar to brilliants, see Fig. 1.2. Since the late 1990s the American company C3, Inc., North Carolina, managed to fabricate achromatic moissanite of gemstone quality. Now that it is possible to control the color, high quality grinded moissanites of 0.1 - 2.0 ct. in yellowish, greenish or brownish colors as well as colorless are grown as monocrystals. The increasing perfection of these crystals make it more and more difficult to prevent malpractice [1] in spite of many cleverly thought-out characterization methods .

In spite of this wide range of application of silicon carbide, this work will focus on SiC as a device material, only. While as a jewel, SiC is always compared to diamond[1], in this area, silicon is the material chosen most often for comparison. Today, for electronic applications, silicon based devices are most widely-used. Due to intensive research, most of the technologically relevant problems are already solved on this field. However, silicon

---

[1]The investigations of nitrogen–related complexes in Chapter 5 of this work benefit from earlier studies on N in diamond, as well.

is rather limited in its use for high-temperature and high-frequency applications. SiC is, here, one of the most promising alternatives, because it has all the desired properties. Furthermore, it is based on silicon – a very common material with yet widely developed and understood technology. This is for compatibility reasons important for the construction of Si/SiC-heterostructures.
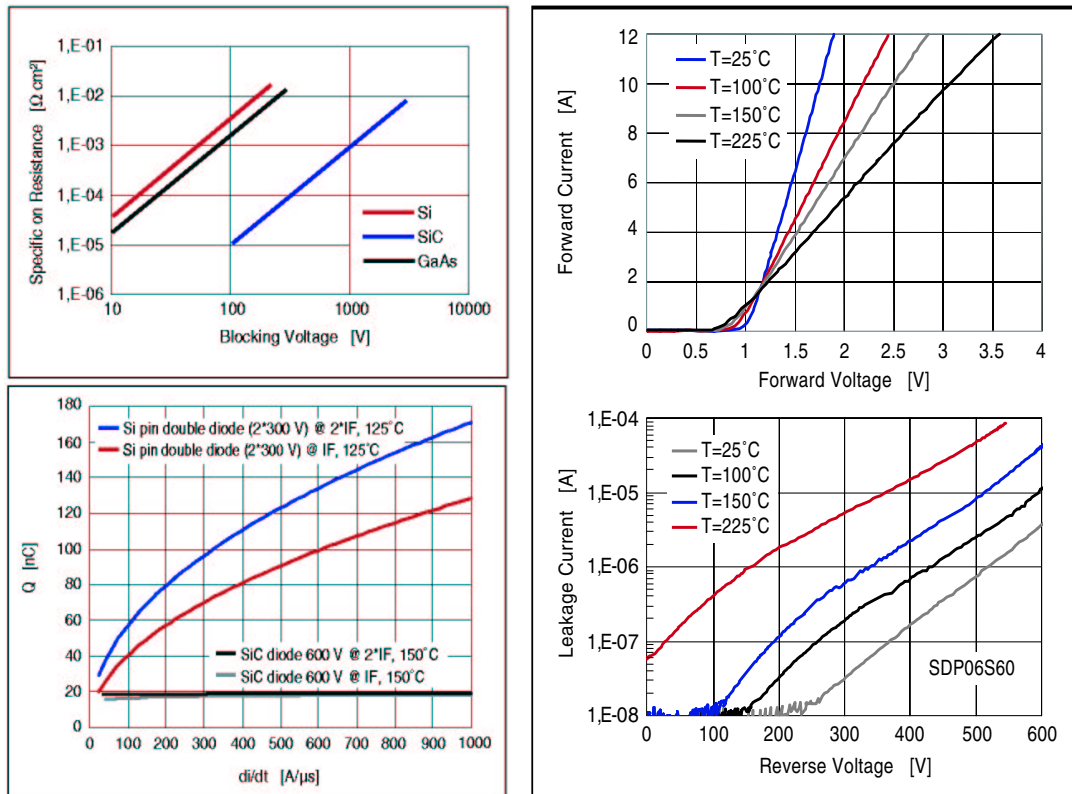
Figure 1.3: The diagrams in the left column show a comparison of the specific on-resistances and blocking voltages of Si, SiC, and GaAs Schottky diodes. On the right hand side, the temperature dependence of forward and reverse characteristics of a 6 A/600 V SiC Schottky diode is shown. Data taken from Ref. [2]

In 1983, S. Nishino et al. succeeded in growing SiC heteroepitaxially on silicon substrate. Some years later, in 1987, the first SiC/Si heterobipolartransistor was built. In the following years, the growth procedure of bulk SiC was permanently improved, such that ever larger monocrystals of device quality could be grown.

In the 1990s, the semiconductor industry concentrated strongly on the realization of unipolar devices, especially Schottky diodes on the basis of SiC. About two years ago, Infineon Technologies was among the first to fabricate SiC high power devices which are smaller and cheaper than conventional power diodes on the basis of silicon or gallium arsenide (GaAs) technology and, furthermore, do not require cooling devices or fans.

Additionally, SiC devices offer high switching frequencies with low losses and high reliability. The Schottky barrier of SiC is higher than in the conventional device materials, the breakdown field strength is by a factor of ten higher than in silicon, and the heat conductivity is comparable to that of copper, resulting in high current densities and low specific on-resistances and leakage currents, compare Fig. 1.3. The upper left diagram in Fig. 1.3

shows the lower specific on-resistances compared to Si or GaAs at higher blocking voltages. The diagrams on the right hand side illustrate typical forward and blocking characteristics of a 600 V SiC Schottky diode at several temperatures. The leakage current increases much less with increasing temperature than in Si or GaAs Schottky diodes. The bottom diagram on the left hand side shows that the capacitive reverse charge Q_c is nearly independent from the temperature and dI/dt. A detailed discussion of these characteristics is beyond the scope of this work. Here, these diagrams shall only illustrate the different behavior of SiC devices and conventional Si or GaAs devices. Consequences for applications of these devices are described in great technological detail in Ref. [2].

Schottky diodes based on silicon or GaAs reach their limits at about 200 V or 250 V, with SiC, though, blocking voltages of 300 V up to 3500 V can be realized [2]. While the maximum switching frequencies were with conventional materials restricted to less than 100 kHz, the new SiC-Schottky diodes make frequencies of more than 500 kHz possible. Consequently, the number and size of passive components in integrated devices, i. e. coils and capacitors, and thereby the costs of the total system, can be reduced.

All these properties make SiC an ideal material for the design of future electronic devices. There are, as expected for a material that is still – compared to silicon – very new in this field of application, unsolved problems. One problem to name here is the growth of high quality crystals with low densities of micropipes and other extended defects. Another problem is the doping of SiC for the creation of n-type and p-type material as is needed for device fabrication. Because of the low diffusivities in SiC, doping has to be done by ion implantation, which, though, damages the crystal lattice dramatically in the implanted region. "Repairing" the lattice is commonly done by post implantation annealing, but this has to be done carefully, if the dopants shall not be removed again from their intended sites. A lack of understanding of the processes in the annealing phase can be traced back to a lack of understanding of the behavior of point defects, both intrinsic defects (created as "damage" by implantation) and dopant atoms. It is the aim of this work to bring some light into this field and investigate some of the processes that are supposed to happen directly after implantation.

In the remaining two sections of this chapter, some currently unsolved problems concerning unidentified (most probably) intrinsic defects and n-type doping are discussed. Then the structural principle of the various crystal structures of SiC and the consequences for the investigations in this work are described.

1.2   Doping of SiC

Due to low defect diffusivities, SiC is commonly doped by ion implantation. Subsequently, an annealing process reduces the lattice damage created and activates the dopants electrically (i.e. promotes them to substitutional sites). The implantation/annealing procedure has to be chosen in a way that unwelcome side effects, as e. g. the formation of electrically inactive complexes, are kept at minimum. Therefore, the investigation of the annealing behavior of intrinsic defects and dopant atoms is crucial for the optimization of the doping procedure.

Early spectroscopic studies have revealed a multitude of radiation-induced intrinsic defect centers, but their origin and structure are in many cases still unclear, hindering the understanding of the dynamics of their creation and annihilation.

Intrinsic defects

Among the intrinsic point defects, the properties of vacancies [3, 4, 5, 6, 7, 8, 9, 10] and the divacancy [11] have been already studied theoretically in great detail. The migration barriers of vacancies and self-interstitials have also been investigated on the zero-temperature potential energy surface [12, 13].
Experimentally, the annealing of vacancies has been studied since decades ago, based on their EPR signals [14]. Such studies resulted in an annealing temperature of $200°C$ for carbon vacancies (V_C) and of $750°C$ for silicon vacancies (V_{Si}) in as-irradiated samples [15, 16]. Based on a new assignment for V_C, the annealing temperature of V_C has been modified to $500°C$ [17, 18, 19, 20]. These values are valid, however, only in the presence of self-interstitials, when the annihilation of vacancies can occur by recombination. In cases where only out-diffusion of vacancies is relevant (i.e. in as-grown samples), V_{Si} disappears above $1400°C$ and V_C can still be detected at temperatures as high as $1600°C$ [21]. In addition to single vacancies also divacancies $V_C V_{Si}$ are common intrinsic defects in SiC. Earlier works identified the P6/P7 signal (photoluminescence spectrum) with the divacancy. Recent EPR-measurements and theoretical results could, however, show that this signal is rather caused by an antisite-vacancy pair $V_C C_{Si}$, as described in more detail in Chapter 3.

In contrast to vacancies, antisite defects received less attention although their formation energies are even lower than those of vacancies [22, 23, 24, 25]. In fact, the carbon antisite (C_{Si}) appears to have the lowest formation energy among all intrinsic point defects, but, according to theoretical predictions, it is electrically, optically and magnetically inactive and, therefore, experimentally almost invisible. In contrast, the calculations predict gap levels related to the silicon antisite (Si_C) in the vicinity of the valence band maximum (VBM) and the possible existence of paramagnetic states [24].

Experimentally, the presence of Si_C was inferred in Au-irradiated samples based on channeling results [26], and Si_C has also been suggested to be the origin of the EI6 electron paramagnetic resonance (EPR) center in electron-irradiated SiC [27]. The latter assignment has, however, been challenged based on the theoretical calculation of the hyperfine constants [13]. Still, it is inevitable that antisites are present after irradiation which unavoidably creates vacancies and self-interstitials. Namely, the recombination of the latter during annealing can not only lead to the perfect lattice structure, but also to antisites, compare Chapter 3. Thus isolated vacancies, interstitials, antisites, and their complexes will coexist in the crystal in the early stages of annealing.

One of the oldest known irradiation induced intrinsic defect is the so-called D_I center [28] observed in 1972 with photoluminescence spectroscopy (mostly in irradiated material but also in as grown samples quenched to room temperature). In Ref. [28], it was shown that the center which survives annealing temperatures as high as $1700 °C$ has to be of intrinsic nature, and the authors suggested the divacancy as atomistic model. Based on calculations of the local vibrational modes, recent theoretical studies [29, 30] suggested, instead, the antisite pair as the origin of D_I. The creation of such antisite pairs and also larger antisite complexes is discussed in Chapter 4.

n-type dopants in SiC

Implantation of SiC with nitrogen (N) is commonly used for the creation of n-type material. In this work, the experimentally observed problem of the saturation of the free charge

carrier concentration at high nitrogen concentrations [31, 32] is investigated. According to Hall- and DLTS-measurements, no concentrations higher than $\approx 10^{19}$ cm^{-3} can be reached for the free charge carriers by further nitrogen implantation. A post implantation treatment consisting of further implantation with boron or aluminum and further annealing at high temperatures can lead to a recovery of the carrier concentration [32, 33].

The processes connected with these observations, complex formation and migration mechanisms of the involved defects are subject of Chapter 5.

Phosphorus, which is used as alternative n-type dopant or also as a co-dopant together with nitrogen in SiC, shows a completely different behavior than nitrogen [31]. In contrast to nitrogen, our calculations show that phosphorus does not tend to form inactive complexes (see Section 5.4). Thus higher concentrations of free charge carriers can be reached and the post-implantation annealing process may be facilitated by using phosphorus instead of nitrogen.

In Chapter 5, we show how the observation of the different behavior of nitrogen and phosphorus can be explained on the atomic scale. Based on investigations of possible mechanisms of their creation, we also suggest some defect complexes that may cause the observed EPR-signals, the interpretation of which is not yet clear.

The problem of interpreting signals measured with various methods and identifying them with atomistic models raises the demand for a combined approach of experimental and theoretical methods. Using and combining various methods is obviously mandatory to improve the knowledge in defect physics.

On the experimental side, besides annealing studies, measurements of hyperfine constants by electron paramagnetic resonance (EPR) and related methods, photoluminescence (PL) spectroscopy, deep level transient spectroscopy (DLTS), and measurements of the Hall constants give information about the nature and the properties of a defect center, see next chapter.

A unique identification of the observed defect centers with atomistic models is, however, most often not possible without augmenting and interpreting the experimental results by theoretical investigations, which approach the identification problem from the other side by starting with the atomistic model and deducing the properties which are measured by various experimental methods.

Due to its ability of simulating large defect structures, the method used in this work (SCC-DFTB) is suitable for a systematic investigation of migration and aggregation mechanisms. In order to obtain an accurate description of the electronic structure of selected defect complexes, a first principle method should be chosen, additionally. To this aim, additional calculations within the plane-wave based code of the Fritz-Haber-Institute (FHI) [34], the Gaussian orbital based AIMPRO code ("Ab initio modelling programm") [35], and the Green's function based LMTO-ASA code [36, 37] ("Linear muffin tin orbitals in atomic spheres approximation") were performed.

1.3   Crystal Structure: the Polytypes of SiC

In SiC, the badly needed understanding of defects is hampered by its characteristic property of not crystallizing in a unique crystal structure. Unlike most common materials, e. g. its constituents Silicon and Carbon, SiC can take various structures, the so-called "polytypes". Many different polytypes are known (up to now more than 200), whereof the technologically most important ones are the cubic 3C and the hexagonal 4H and 6H. This polytypism was

already observed by H. Baumhauer in 1912, a detailed investigation of this effect was, however, first made by B.G. Dubrovskii in 1971. All polytypes have the same local order with fourfold coordinated, sp^3-bonded Si- and C-atoms, but differ from each other by the way, in which the SiC-bilayers, i. e. {111} (cubic polytype) or {0001} planes (hexagonal polytypes), respectively, are stacked upon each other.
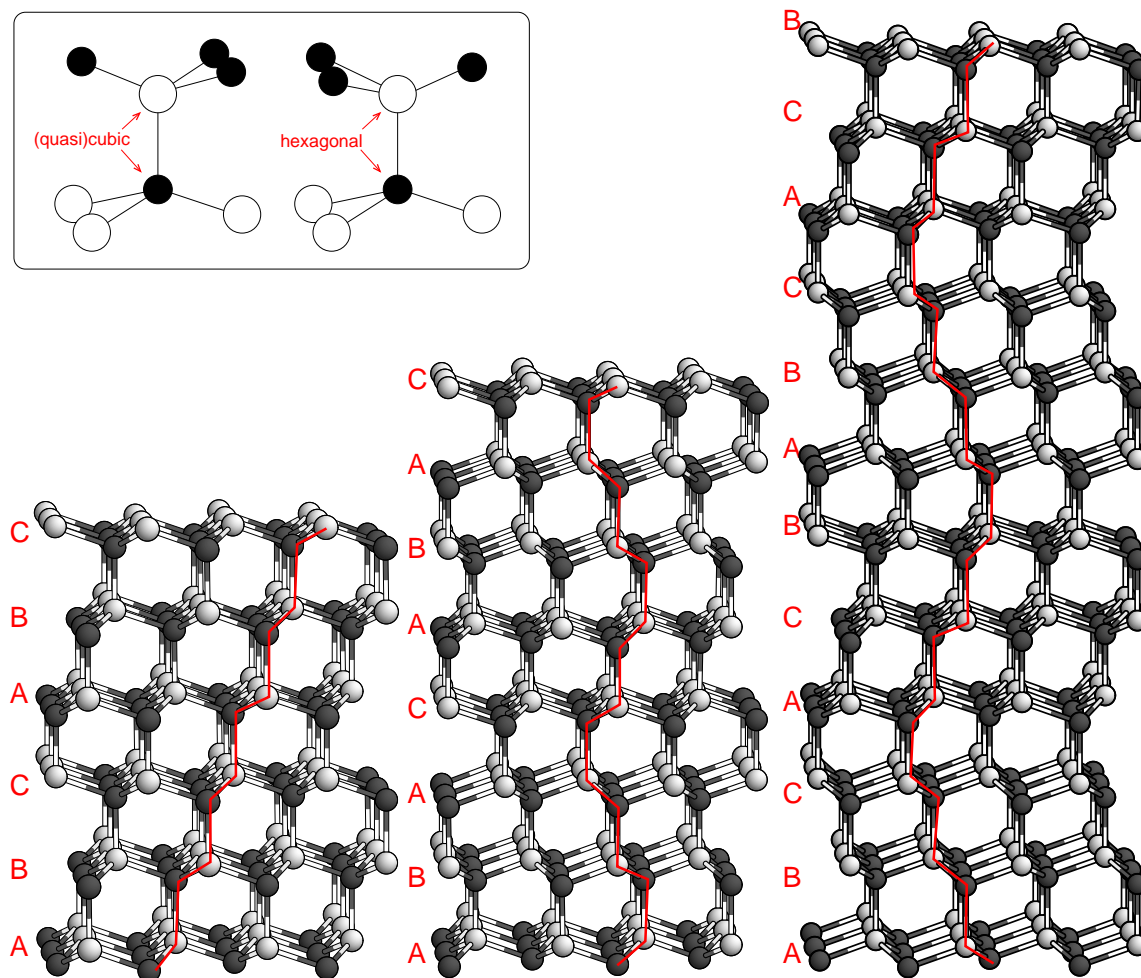
Figure 1.4: The most common polytypes of SiC (from left to right): 3C, 4H, 6H. The red line illustrates the stacking order of the SiC-bilayers along the vertically shown [0001] direction. *Inlet:*Local structure of (quasi)cubic (*left*) and hexagonal (*right*) sites in a binary lattice.

In the 3C-polytype, all the bilayers have the same orientation, resulting in a zinkblende structure, stacking order ABC(ABC...). The 3C–lattice is shown in the left part of Fig. 1.4. In the figure, the [0001] direction[2] is shown vertically, the view-plane is of {11$\bar{2}$0} type. In the figure, two unit cells along the [0001] direction are shown, since the stacking order leads to a periodicity of three bilayers. As a guide to the eye, the red line illustrates the stacking sequence of the SiC-bilayers.

Before stacking the bilayers upon each other, they can as well be rotated by 60° around the [0001] axis. Performing this operation in defined ways leads to other polytypes with certain stacking orders. The 4H-polytype, shown in the center of Fig. 1.4 has a periodicity of four bilayers with the stacking sequence ABCB(ABCB...). On the right, the 6H-polytype

---

[2]For better readability, the cubic [111] axis shall be denoted by the hexagonal notation [0001], as well, which is equivalent but only differs in the choice of the crystallographic unit system.

Table 1.1: Properties of the three most common SiC-polytypes. The values are taken from Ref. [38]. The polytype 2H, wurtzite structure, does not exist but is listed for reasons of completeness. Defining a hexagonality via the percentage of hexagonal lattice-sites, 3C and 2H are the limits of the scale, 4H lying in the middle.

Polytype (Ramsdell)	Stacking-sequence	Atoms per unit cell	Latticeparameter a[Å]	c[Å]	Bandgap [eV]	Hexagonality [%]
3C	ABC	6	4.3596	4.3596	2.39	0
2H	AB	4	3.0763	5.0480	3.33	100
4H	ABCB	8	3.0730	10.0530	3.26	50
6H	ABCACB	12	3.0806	15.1173	3.08	33

with a periodicity of six bilayers and the stacking sequence ABCACB(ABCACB...) is shown.

There exist other polytypes, e. g. the 15R with rhombohedral symmetry and the stacking sequence ABCACBCABACABCB(AB...), but all the polytypes do not differ much in their energetical stability, and the main difference comes up already between 3C and 4H or 6H.

Due to the rotation of a bilayer, the local order changes for the second neighbor surrounding of a lattice site. As a consequence, the lattice sites can be divided into (quasi-)cubic (no rotation of the bilayer) and hexagonal (60° rotation) sites. The local structure of the different sites is shown in the small inlet in Fig. 1.4. While the 3C polytype consists of cubic sites only, there are equal numbers of cubic and hexagonal sites in 4H-SiC. In 6H, one third of the lattice sites is hexagonal, the other sites can be divided into two different cubic sites, according to their next neighborhood.

For the investigation of surfaces of the material, especially the nonpolar ($10\bar{1}0$)-surfaces, the polytypes have to be treated separately, since completely different reconstruction mechanisms can happen at the surfaces of the same direction in the different polytypes, as we have investigated for the clean surfaces [39, 40] as well as for surfaces with adstructures. The passivation of differently oriented surfaces with oxygen has been investigated in [41, 42]. For not so widely extended defects, as point defects and small complexes of them, the calculated differences between the polytypes turn out to be very small in many cases. Reflecting on the migration mechanisms of point defects in 4H or 6H, a change between cubic and hexagonal sites is unavoidable for long-range diffusion processes. A defect that migrates along the hexagonal axis of the crystal will move from a cubic to a hexagonal site and so on (consider e. g. migration along the red line in Fig. 1.4). During migration inside a (0001) plane, i. e. perpendicular to the hexagonal axis, however, migration leads either from cubic to cubic or from hexagonal to hexagonal sites. Migration barriers vary slightly because of this difference, but test calculations have shown that these energy differences are usually small and often below the accuracy of the method.

Most of the investigations that are presented in this work were performed in 3C and 4H. Variations concerning the symmetry of a small defect complex are most often as small as the local deviation of 4H from C_{3v} symmetry. Where it turned out to give more insight or where significant differences appeared, a distinction is made, otherwise the results are just

described for one polytype.

This does, of course, not mean that for the description of point defects a distinction between the polytypes is not needed in general. Attention has e. g. to be paid to the electronic structure. Table 1.1 shows that the band gap in 3C-SiC is much smaller than in 4H and 6H. This can affect the number of existing charge states of a defect: A localized defectlevel that is induced in the band gap by a defect in 4H or 6H can already lie in the conduction band for the same defect in 3C, such that the number of existing charge states of a defect can change with the polytype.

Chapter 2

Theoretical Description of Defect Dynamics

How the problems revealed in the previous chapter can be treated on a theoretical basis is subject to this chapter. Before the method of calculation used for atomistic simulations is described, some general aspects of point defects are summarized as far as they play a role for our investigations described in the following chapters. This is done on the one hand with the object of showing up how much information about a problem can be gained already before starting an atomistic simulation, and on the other hand to make clear which effects cannot be covered by such simulations. This applies e. g. to the influence of high defect concentrations on migration processes and charge state effects. Many general statements, though, can be made material independent, and for a qualitative understanding, an atomistic simulation of a specific material is not needed.
Next, a brief overview of the used computational method and its theoretical background, density functional theory, is given. The last two sections of this chapter are dedicated to a description of how migration paths, vibrational spectra and free energies can be calculated with this method. The latter requires the calculation of entropies, for which extensive test calculations are presented, which give a classification of the accuracy expected for the method of calculation as compared to first principle calculations.

2.1 Some General Aspects of Point Defects

Although it is usually spoken about *one* defect, there is hardly ever only *one* defect in a crystal, not even only one kind of defect. How many defects there are in a piece of material is described by thermodynamics. This is, however, only true in thermodynamic equilibrium. As discussed in Section 2.1.2, an implantation process violates this assumption.

2.1.1 Point defects at thermodynamic equilibrium

In thermodynamic equilibrium, the concentration of the defects at a given temperature is a function of their free energy of formation. For low defect concentrations, the different kinds of defects can be treated independently, so that the number n_i of each type i of a defect at the temperature T is determined by the free energy of formation $\Delta G_i^{\mathrm{form}}$ of this

defect only [43]:

$$n_i = Z_i N \cdot e^{-\frac{\Delta G_i^{\mathrm{form}}}{k_B T}} \quad . \tag{2.1}$$

Here, N denotes the number of available sites in the lattice, while Z_i accounts for the number of equivalent configurations the defect could take[1]. Realistic defect concentrations are most often too high to justify a total neglect of interactions between the defects. Those are of various origin. The fact that many defects exist in non-neutral charge states for a given Fermi level results e. g. in a long-range Coulomb interaction between two defects of unequal charges. This can support the formation of pairs of single defects with unequal charges, or at least enhance a migration process of them towards each other.

Pair formation can also be caused by short-range interactions between two defects, if e. g. the local lattice distortion can be reduced in this way. Considering such effects leads to an expression for the number of pairs of defects that are present in thermodynamic equilibrium. Since a detailed knowledge of the distribution of the various kinds of defects is missing and is not even accessible, several assumptions have to be made. In any case, expressions of the form of Eq. 2.1 can be derived for the number of vacancies, interstitials or pairs of them, with the factor Z_i adjusted to the described problem. For pairs of a vacancy and an interstitial as an example, it becomes $Z_i = \frac{n_{\mathrm{vac}} \cdot n_{\mathrm{int}}}{N^2}$. In case of pairs, $\Delta G_i^{\mathrm{form}}$ is the binding free energy between the constituents [43].

2.1.2   The situation after an implantation process

Ion implantation is used to create special point defects intentionally. In Chapter 5, the n-type doping of SiC with nitrogen is discussed in more detail. Actually, the aim of the implantation procedure is to bring N-atoms into the SiC-lattice, thereby forming substitutional point defects on the carbon sublattice (N_C). There they are known to act as shallow donors, which are required as a source for free charge carriers.

It is, however, not possible to carry out this procedure without creating other intrinsic defects at the same time. In addition to those defects that are present due to the equilibrium concentrations under the given circumstances[2], the bombardment process creates besides the implanted species also vacancies and interstitials in equal amounts. Thus, in the implanted region of the crystal, usually a rectangular profile, the defect concentration is substantially larger than the thermodynamic equilibrium concentration, as given by Eq. 2.1.

Implantation is usually followed by an annealing phase. This phase is intended to supply the energy needed to activate mechanisms for the disappearance of the unwanted by-products of the implantation process, i. e. recombination or migration towards sinks at surfaces or dislocations. At the same time the dopant atoms have to be promoted to their intended positions and kept there if once built in.

In this post-implantation annealing process, the implanted sample is heated up either gradually (isochronal) or in a procedure called RTA, rapid isothermal annealing, in which the sample is rapidly heated up to a given temperature that is then kept constant for a while, typically one half till one hour. The fact that during such an annealing phase also new defect complexes can evolve can have unpleasant consequences, as discussed e. g. for the process of nitrogen doping in Chapter 5.

---

[1]A substitutional defect with a D_{2d} symmetry can e. g. occur in three different configurations on a site with originally T_d-symmetry.

[2]that means defects that have already been created during growth
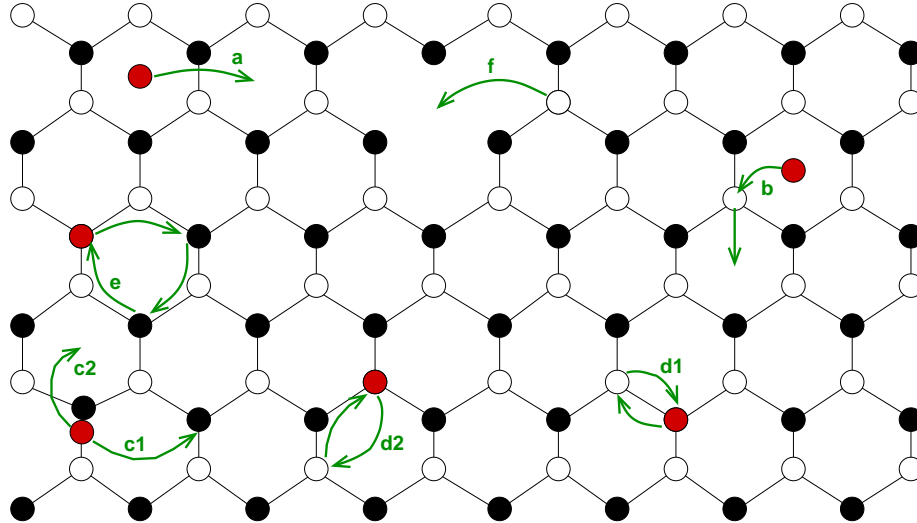
Figure 2.1: Principle ways how migration of point defects can take place in a binary material. The red circles denote defect atoms, i. e. of intrinsic or extrinsic type, and are supposed to move along the green arrows. See text for details.

2.1.3 Migration of defects

Regardless of the details of the annealing mechanism, the movement of atoms will consist of one or a combination of several of the mechanisms that are schematically shown in Fig. 2.1[3]. Probably among the lowest energy migration mechanisms is the process labelled with (a), where an atom moves from one interstitial site to a neighboring one. Since there are different kinds of interstitial sites in the polytypes of SiC with either hexagonal or tetrahedral character, compare Fig. 1.4, the interstitial can move to an equivalent site or to a different one. More complicated is the mechanism (b), where an interstitial kicks out a substitutional atom to an interstitial site that in a next step may kick into another substitutional site (*kick-in/kick-out mechanism*). The processes labelled with (c1) and (c2) are based on *split-interstitial* mechanisms[4]. One of the two atoms sharing one lattice site can either move to an equivalent position (c1) (or change to the other sublattice) or it can move to an interstitial site (c2).

A substitutionally built in atom can migrate by *exchange processes* with either a direct (d1) or a second (d2) neighbor. In the latter case only one sublattice is involved, while a direct exchange mixes the sublattices. Another indirect exchange process is the basis of the ring mechanism (e), in which several atoms simultaneously change places. Due to its rather complicated structure requiring three atoms to move in a defined way, this mechanism is not very likely to be among the most important mechanisms for the diffusion of a certain defect.

The *vacancy assisted mechanism* (f), finally, consists of jumps of defect atoms into a vacancy. Like the exchange process this can happen on one sublattice exclusively or go along with a change of the sublattice, depending on the capture radius of the vacancy (see also Section 3.3). A directed long-range diffusion of a defect via vacancy jumps can then be imagined as the three step sequence of a jump of the defect atom into the vacancy, the dissociation of the vacancy from the defect and the arrival of a new vacancy. Alternatively – especially in case of high binding energies between the defect atom and the vacancy – a

---

[3]The lattice shown here is of the cubic 3C-type, but of course the same holds for any crystal lattice.

[4]In Chapter 5 it will be shown that such split-interstitials play an important role for the mobility of nitrogen in SiC.

ring-like movement of the vacancy around the defect atom is conceivable[5].

2.1.4 Jump probabilities

It depends on the activation energy, which of the mechanisms discussed in the previous section describes the migration of a certain defect, or at least is the main mechanism responsible for a certain observation. Decisive are, i. e., the migration energy barriers for the process and the probability that all necessary conditions for the process are fulfilled. For the sublattice movement of an interstitial (Fig. 2.1 (a)) or a vacancy (Fig. 2.1 (f)) no further assumptions are required, thus the jump probability is given by

$$K = \nu \cdot e^{-\frac{\Delta G_{\text{act}}}{k_B T}} \tag{2.2}$$

with the height $\Delta G_{\text{act}} = \Delta U - T \cdot \Delta S + p \cdot \Delta V$ of the free energy migration barrier and an "effective frequency" ν for the jump [43].
The more complicated mechanisms require, additionally, the presence of other atoms or vacancies, such that e. g. for the vacancy assisted mechanism the probability for a jump is given by

$$K = \nu \cdot e^{-\frac{\Delta G_{\text{act}}}{k_B T}} e^{-\frac{\Delta G_{\text{vac}}^{\text{form}}}{k_B T}} \quad . \tag{2.3}$$

In this case, the jump probability depends on the free energy of formation of the assisting vacancy.
For a migration process with equivalent start- and end-configurations, the rate constant K can be further evaluated. The mainly on classical mechanics based *rate theory* leads to the expression

$$\nu = \nu_0 \cdot e^{\frac{\Delta S_{\text{mig}}}{k_B}} \tag{2.4}$$

for the effective frequency ν [43]. It depends exponentially on the migration entropy ΔS_{mig}, i. e. the difference in entropy between the equilibrium- and the saddle point geometries. ν_0 is the vibration frequency of the migrating atom in the equilibrium position.
For selected processes leading from a start-configuration to an equivalent end-configuration, the jump probabilities and diffusivities have been calculated in Chapters 4 and 5.

2.1.5 Charge state effects on the migration of defects

The Fermi level determines, in which charge state a defect is stable. In thermal equilibrium, it is constant, but especially in the implanted region, the Fermi level varies locally due to an inhomogeneous distribution of the various defects, and consequently a defect can exist in several charge states q_1, q_2 with concentrations $\alpha_1 N$, $\alpha_2 N$ determined by the energetical distance between the localized defect level E_D and the Fermi level E_F. The fraction α_1 of defects in charge state q_1 compared to the fraction $\alpha_2 = 1 - \alpha_1$ of defects in charge state q_2 is then

$$\frac{\alpha_1 N}{\alpha_2 N} = \frac{\alpha_1}{1 - \alpha_1} = g_D \cdot e^{\frac{E_D - E_F}{k_B T}} \tag{2.5}$$

where the factor g_D accounts for the degeneracy of the defect level E_D [43].
The migration enthalpy is changed accordingly, and as a consequence also the jump probability. Considering the coexistence of two charge states as above, the (total) jump probability can be written as the sum of the probabilities for a jump in each charge state:

$$K_{\text{tot}} = \alpha_1 K_1 + \alpha_2 K_2 = \alpha_1 K_1 + (1 - \alpha_1) K_2 \tag{2.6}$$

---

[5]The vacancy assisted processes play an important role for the mobility of antisites in SiC, see Chapter 4.

The effect of the lowering of an activation energy due to a change of a defect into another charge state is known as "ionization enhanced migration" and can in some cases have a strong influence on the diffusion rate.

As in common literature in this work, migration of defects is only investigated for a non-changing charge state during the process. Such charge state effects as well as the hindering or enhancement of a migration process by the presence of other defects can not be accounted for in a satisfying way, because such effects strongly vary with the environmental conditions and do, therefore, not allow to deduce a general picture. Nevertheless, a superposition of various competing and partly contrasting effects on the activation energies has to be expected, such that the analysis of the pure processes might give a good description of the average behavior of the investigated defect.

The considerations of the previous sections provide a qualitative understanding, especially for *general* (i. e. not material dependent) information about the behavior of defects in solids. Quantitative statements require, though, the use of more sophisticated methods. In this work, an approximative method, based on density functional theory (see next section), has been used for atomistic simulations. This method, the density functional based tight binding (*DFTB*), has been described in great detail in various publications, see Ref. [44, 45, 46], thus only a brief sketch of the idea shall be given here. The extensions made in SCC-DFTB (selfconsistent charge-) are illustrated in Ref. [47].

2.2   Density Functional Theory

In quantum mechanics, the properties of a crystal are usually described by a wavefunction $\Psi(R_1, R_2, \ldots, R_{N_{\mathrm{nuc}}}; r_1, r_2, \ldots, r_{N_{\mathrm{el}}})$ that depends on the coordinates R_i of N_{nuc} nuclei and r_j of N_{el} electrons. It is practically impossible to find the ground state of such a system by minimizing the total energy of this many-body system , since a Schrödinger equation for these $3N_{\mathrm{nuc}} + 3N_{\mathrm{el}}$ coordinates would have to be solved[6]. The most well-known approximation that is made to reduce this problem is the *Born-Oppenheimer approximation* [48], where it is utilized that the motion of the nuclei due to their larger masses happens on a substantially larger time-scale than the motion of the electrons. In other words, the electrons follow the movement of the nuclei practically immediately. The motion of the nuclei can therefore be decoupled from that of the electrons, and the key problem remains to determine the electronic wavefunction for a given configuration of nuclei. In spite of this reduction, for practical applications the number of parameters has to be reduced further on[7]. One possibility to achieve this is to use the *density functional theory* (DFT). Instead of using a wave function, the key quantities of the system are expressed in terms of a particle density

$$n(\mathbf{r}) = \langle \Psi | \sum_i \delta(\mathbf{r} - \mathbf{r_i}) | \Psi \rangle \ . \tag{2.7}$$

The total energy of a quantummechanical system can then be written as a functional of the electron density

$$E = E[n(\mathbf{r})] \ . \tag{2.8}$$

---

[6]Consider that in a crystal a typical order of magnitude are $\approx 10^{23}$ atoms!

[7]For N particles the computing time grows $> N^5$. Chosing twice the number of atoms in the model leads therefore to a 32 times longer computing time.

That this is uniquely possible for a (non-degenerate) ground state of a system of electrons has been shown by Hohenberg and Kohn [49].

For a system of N electrons, E has – in atomic units – the form

$$E[n] = T[n] + \frac{1}{2} \iint \frac{n(\mathbf{r_1})n(\mathbf{r_2})}{|\mathbf{r_1} - \mathbf{r_2}|} d\mathbf{r}_1 d\mathbf{r}_2 + \int n(\mathbf{r})V_{\text{ext}}(\mathbf{r})d\mathbf{r} \; , \tag{2.9}$$

where $T[n]$ is the kinetic energy of N interacting electrons, the second term is the Coulomb interaction of all electrons, and the third term accounts for the external potential V_{ext} for the given configuration of the nuclei.

The kinetic energy $T[n]$ is generally unknown, thus further approximations have to be made. Starting with the kinetic energy of N *non-interacting* electrons

$$T_0[n] = \sum_{i=1}^{N} \int \Phi_i^\star(\mathbf{r}) \left[-\frac{\nabla^2}{2} \right] \Phi_i(\mathbf{r})d\mathbf{r} \tag{2.10}$$

with

$$n(\mathbf{r}) = \sum_{i=1}^{N} |\Phi_i(\mathbf{r})|^2 \; , \tag{2.11}$$

Kohn and Sham proposed to inherit this density for the description of *interacting* electrons [50] and include the many-body effects in $T[n]$ then by adding the so-called *exchange–correlation functional* $E_{\text{xc}}[n]$

$$T[n] = T_0[n] + E_{\text{xc}}[n] \; . \tag{2.12}$$

Most, but not all systems can be treated like this, but the validity of Eq. 2.11 is limited to those states that can be expressed in a single Slater determinant. In cases where this is not possible, other theories, e. g. Hartree-Fock methods, have to be used to obtain an exact description of the electronic structure. This is, however, not always required, and at least some properties of interest can also be obtained within the DFT description.

The wave functions $\Phi_i(\mathbf{r})$, the *Kohn-Sham orbitals*, can be obtained by the variation of $E[n]$ with respect to $\Phi_i(\mathbf{r})^\star$ and under the condition of constant particle number N. This leads to the *Kohn-Sham equations*

$$\left[-\frac{\nabla^2}{2} + V_{\text{eff}}[n(\mathbf{r})] \right] \Phi_i(\mathbf{r}) = \varepsilon_i \Phi_i(\mathbf{r}) \tag{2.13}$$

with the Lagrange parameters[8] ε_i of the constraint of constant N and the effective potential

$$V_{\text{eff}} = V_{\text{ext}}(\mathbf{r}) + \int \frac{n(\mathbf{r}')}{|\mathbf{r} - \mathbf{r}'|} d\mathbf{r}' + \frac{\delta E_{\text{xc}}[n(\mathbf{r})]}{\delta n(\mathbf{r})} \; . \tag{2.14}$$

Equations 2.13 are coupled via the effective potential V_{eff} and the exchange–correlation potential $V_{\text{xc}} = \delta E_{\text{xc}}[n(\mathbf{r})]/\delta n$, which depend on *all* Kohn-Sham orbitals $\Phi_i(\mathbf{r})$, such that a self–consistent solution is required.

The exchange correlation contribution to the total energy is generally unknown, but for special cases of only small variations of this contribution, approximations based on a homogeneous electron gas can be used. Today, the most common approximation is the *local*

---

[8]Only if Koopman's theorem is valid, i. e. if the removal of one electron does not lead to a change in the Φ_i of the remaining N-1 electrons, the ε_i can be interpreted as single particle energies. For large numbers N of electrons, it is probable that this presumption holds approximately. In general, this is, however, not valid.

density approximation (LDA)[51, 52, 53], which assumes that E_{xc} can be expressed as a functional the integral core of which only locally depends on the density $n(\mathbf{r})$

$$E_{xc}[n] = \int n(\mathbf{r})\, V_{xc}[n(\mathbf{r})]d\mathbf{r} \approx \int n(\mathbf{r})\, V_{xc}^{LDA}(n(\mathbf{r}))d\mathbf{r} \ . \tag{2.15}$$

This approximation is well established and its limits as well as certain possible improvements are known. As the probably most common example of disadvantages, the incorrect description of the band gap in semiconductors has to be named. LDA usually underestimates its width, which can lead to problems with the decision whether a certain charge state of a defect exists or not. The Scissor operator [54] or the Baraff–Schlüter correction [55] are examples of techniques to account for this failure.

Inserting the expressions for the exchange–correlation contribution and the kinetic energy into Eq. 2.9 and considering the energy contribution of the nuclei, the final expression for the total energy reads

$$E_{tot} \ = \ \sum_j^{occ} n_j\langle\Phi_j|\hat{H}|\Phi_j\rangle - \frac{1}{2}\int\int\frac{n(\mathbf{r_1})n(\mathbf{r_2})}{|\mathbf{r_1}-\mathbf{r_2}|}d\mathbf{r}_1 d\mathbf{r}_2 - \int n(r)V_{xc}[n(\mathbf{r})]d\mathbf{r} \tag{2.16}$$

$$+E_{xc}[n(\mathbf{r})] + \frac{1}{2}\sum_{I,J}^{N_{nuc}}\frac{Z_I\cdot Z_J}{|\mathbf{R_I}-\mathbf{R_J}|} \ .$$

The terms in Eq. 2.16 have been slightly rearranged in order to obtain E_{tot} in the form needed in the following. The hamiltonian $\hat{H}$ in the first term contains the kinetic energy part, the external potential, the Hartree energy and the exchange and correlation potential,

$$\hat{H} = -\frac{1}{2}\nabla^2 + V_{ext} + \int\frac{n(\mathbf{r}')}{|\mathbf{r}-\mathbf{r}'|}d\mathbf{r}' + V_{xc}[n(\mathbf{r})] \ , \tag{2.17}$$

the second and third term in Eq. 2.16 correct for the double counting terms within this hamiltonian. The fourth term of Eq. 2.16 is the exchange correlation energy, the last term accounts for the nuclear repulsion, $E_{ion-ion}$.

In principle, point defects, extended defects, surfaces, etc. could be described by first principles within LDA-based DFT as presented here. For the description of larger defects, i. e. not only extended defects as e. g. dislocations but also complexes of point defects, this pure DFT is much too elaborate. Although the time scaling behavior could be reduced from $> N^5$ in many-body theory [56] to $\sim N^3$ in LDA-DFT, the required resources exceed most often the capacity of today's advanced computing facilities. Molecular dynamical simulations or as well static calculations of migration paths of defects – both procedures which are in principle based on a large number of single total energy calculations –, are much too time consuming in pure DFT.

Anyway, in many cases the good accuracy of this pure DFT is not needed, and more approximative methods can be used. Many different approaches have been made to develop DFT-based methods with a good performance on the one hand and a low loss of accuracy compared to pure DFT. A great variety of computer codes exists – the main difference between them is the basis set used for the wave functions. Very common is the use of a plane wave basis, as e. g. in the FHI-code [34], which has been used as a reference for some calculations in this work. These methods are commonly considered to have a very high accuracy, although, of course, also here typical drawbacks are known.

Considerably more approximative are tight-binding methods, which use a local basis set.

Most of these methods are, however, not based on density functional theory but are so-called semi-empirical methods, i. e. depend on parameters obtained by fitting certain quantities to experimental data. A clearly lower accuracy and often a bad transferability of the parametrized description characterize many of these semi-empirical tight-binding codes.

Both approaches have their advantages and disadvantages, and the method used in this work (DFTB) tries to combine the accuracy of DFT-based methods and the high efficiency of tight-binding approaches. Generally, the accuracy of this method, in which no empirical parametrization is used, comes closer to that of first principle codes than that of conventional empirical tight-binding methods. The basic ideas are described in the following section, while for a detailed description, the reader is referred to Refs. [45, 46, 47].

2.3   SCC–DFTB

Starting with expression 2.16, the total energy used in DFTB can be derived, following an idea of Foulkes and Haydock [57]: They suggested to expand the total energy E_{tot} at a reference density $n_0(\mathbf{r})$. Fluctuations $\delta n(\mathbf{r}) = n(\mathbf{r}) - n_0(\mathbf{r})$ are then treated as perturbation. With this, Eq. 2.16 becomes

$$
\begin{aligned}
E_{\text{tot}} \;=\; & \sum_j^{occ} n_j \langle \Phi_j | \hat{H}_0 | \Phi_j \rangle - \frac{1}{2} \iint \frac{n_0(\mathbf{r_1}) n_0(\mathbf{r_2})}{|\mathbf{r_1} - \mathbf{r_2}|} d\mathbf{r}_1 d\mathbf{r}_2 - \int n(\mathbf{r}) V_{\text{xc}}[n_0] d\mathbf{r} + E_{\text{xc}}[n_0] + E_{\text{ion-ion}} \\
& + \frac{1}{2} \iint \left(\frac{1}{|\mathbf{r_1} - \mathbf{r_2}|} + \frac{\partial^2 E_{\text{xc}}}{\partial n(\mathbf{r_1}) \partial n(\mathbf{r_2})} |_{n_0} \right) \delta n(\mathbf{r_1}) \delta n(\mathbf{r_2}) d\mathbf{r}_1 d\mathbf{r}_2 \qquad\qquad (2.18)
\end{aligned}
$$

with the "bandstructure term" (first term in the first row) and all the other terms of Eq. 2.16 depending only on the reference density $n_0(\mathbf{r})$, and a second order term (second row) quadratically depending on the density fluctuations $\delta n(\mathbf{r})$. Expressions linear in $\delta n(\mathbf{r})$ cancel exactly in the expansion. This equation can be rewritten as

$$
E_{\text{tot}} \approx \sum_j^{occ} n_j \langle \Phi_j | \hat{H}_0 | \Phi_j \rangle + E_{rep} + \frac{1}{2} \sum_\mu \sum_\nu \gamma_{\mu\nu} \Delta q_\mu \Delta q_\nu \qquad\qquad (2.19)
$$

with the repulsive potential E_{rep} and the second order term, depending on the Mulliken charges. This term will be discussed later in this section.

In the standard formulation of the method, *DFTB*, only the first two terms were considered, while higher order corrections were neglected, and especially for homonuclear systems a good description of various material properties was achieved. For systems consisting of more than one species, and especially in case of strong charge transfer between the different atoms (strong ionic bonding character), the extended version of the method, *SCC-DFTB*, where 'SCC' stands for 'self–consistent charge' and the second order term is calculated, yields clearly improved results [9].

The main distinction of the DFTB method from other (semi-empirical) tight-binding methods is the way how the hamiltonian for the bandstructure term and the repulsive interactions are treated. In the original tight binding formulation of Slater and Koster [58], the exact many-body hamiltonian operator is expressed with a parametrized hamilton matrix.

---

[9]In this work SCC-DFTB was used throughout.

While the matrix elements were then obtained from fits to the experimentally determined electronic structure of reference systems, in the DFTB method any empirical parameterization is avoided. Instead, the hamiltonian and the overlap matrices are obtained from preceding selfconsistent LDA-DFT calculations of suitable reference systems. The repulsive potential is then as a superposition of short-range repulsive two-particle potentials constructed as the difference of the cohesive energy calculated within SCF-LDA and the bandstructure energy calculated in the tight-binding approximation. The quality of the obtained parameterization depends, of course, on the choice of the reference structures. They should, therefore, be chosen carefully in a way to describe as many different properties of the material as well as possible. The advantage of this procedure over empirically parametrized tight-binding methods is a substantially better transferability and results closer to first principle calculations.

To evaluate the expression in Eq. 2.18, an initial density n_0 has to be known. In DFTB, this initial or reference density is constructed as the superposition of atomic-like densities n_0^α centered at the atoms α:

$$n_0 = \sum_\alpha n_0^\alpha \ . \tag{2.20}$$

The Kohn-Sham wavefunctions Φ_i are expanded in localized Slater-type orbitals φ_ν:

$$\Phi_i = \sum_\nu c_{\nu i} \, \varphi_\nu(\mathbf{r} - \mathbf{R}_\alpha) \ , \tag{2.21}$$

where the φ_ν are obtained from the solution of a modified Schrödinger equation:

$$[\hat{T} + V_{\text{eff}}[n_0^\alpha] + \left(\frac{r}{r_0}\right)^2] \varphi_\nu(\mathbf{r}) = \varepsilon_\nu \, \varphi_\nu(\mathbf{r}) \tag{2.22}$$

with a compression radius r_0 depending on the covalent radius of the atom[10]. In numerous calculations in various materials [59], the basis functions φ_ν obtained with the compression term $(\frac{r}{r_0})^2$ have been shown to yield a better description of the energy and the geometrical quantities, i. e. bond lengths and angles, than without this compression[11][59].

The coefficients $c_{\nu i}$ in the expansion of the φ_i are obtained as solution of the secular equation

$$\sum_\nu c_{\nu i}(H_{\mu\nu}^0 - \varepsilon_\nu S_{\mu\nu}) = 0 \tag{2.23}$$

which is obtained from the variation of the energy with respect to the $c_{\nu i}$. $H_{\mu\nu}^0$ and $S_{\mu\nu}$ are the hamiltonian and overlap matrices: $H_{\mu\nu}^0 = \langle \varphi_\mu | \hat{H}_0 | \varphi_\nu \rangle$ and $S_{\mu\nu} = \langle \varphi_\mu | \varphi_\nu \rangle$. The diagonal elements of $H_{\mu\nu}^0$ are the energies of free atoms ε_μ^{atom}.

In the first versions of this method, the starting density n_0 was expressed as a superposition of the potentials of the (pseudo-)atoms. Later on, it turned out that a superposition of the electron densities of these (pseudo-)atoms leads to a better description [45]. The parameters used in this work were all created by the superposition of densities[12]. In any case, the matrix elements $H_{\mu\nu}^0$ and $S_{\mu\nu}$ depend only on the reference density n_0 and can be tabulated with respect to the distance of two atoms. The repulsive potential constructed as mentioned above can similarly be tabulated depending on this distance, so that the

---

[10]The standard value is $r_0 \approx 1.85 \cdot r_{\text{covalent}}$. The indices μ and ν in the summation are an abbreviation for the quantum numbers n, l, and m that appear in the expression for the Slater-type orbitals.

[11]This holds not only for solids but also for the description of molecules.

[12]For the parameterization of silicon, a wavefunction and a density compression radius r_0 of 6.7 and 3.3 was used, for carbon 7.0 and 2.7, for nitrogen 11.0 and 2.2, and for phosphorus 9.0 and 3.8 (in a_{Bohr}).

solution of Eq. 2.23 with these tabulated values yields the DFTB-energy of the system.

The second order term in Eq. 2.18 is calculated from the Mulliken charges $\Delta q_\alpha = q_\alpha - q_\alpha^0$ with

$$q_\alpha = \frac{1}{2} \sum_i^{occ} n_i \sum_{\mu \in \alpha} \sum_\nu^N (c_{\mu i}^* c_{\nu i} S_{\mu\nu} + c_{\nu i}^* c_{\mu i} S_{\nu\mu}) . \tag{2.24}$$

The function $\gamma_{\alpha\beta}$ in Eq. 2.19 denotes the monopole approximation of an expansion of the density fluctuations δn in this second order term in a series of radial and angular functions. The analytic expression for $\gamma_{\alpha\beta}$ is derived in Ref. [60]. In the limit of large atom distances $R \longrightarrow \infty$, $\gamma_{\alpha\beta}$ describes the Coulomb-interaction between two point charges, $\gamma_{\alpha\beta} \longrightarrow \frac{1}{R}$. For one atom, i. e. $R = 0$, $\gamma_{\alpha\beta} = \gamma_{\alpha\alpha}$ has the value of the Hubbard Parameter U_α (for details see Refs. [45, 60]).
This construction of the second order correction necessitates a self-consistent treatment in the energy calculation.
The interatomic forces for use in the conjugate gradient scheme or in molecular dynamic simulations are obtained by taking the derivative of the total energy of Eq. 2.18 with respect to the nuclear coordinates.

In the past, SCC-DFTB has been used successfully for the description of systems containing up to approximately 700 atoms. The tabulation of the matrix elements make the performance ideal for molecular dynamics simulations and diffusion processes. Such problems can hardly be treated by first-principle methods. The accuracy of SCC-DFTB has to be classed between that of usual tight-binding and first-principle methods. Although the description of geometries and total energies can compete with that of ab initio calculations, the electronic structure is clearly less accurate. It has therefore turned out to be a good approach to combine several methods, such that the time-consuming investigation of many different structures, molecular dynamics simulations, and diffusion mechanisms are done within SCC-DFTB. For selected structures, ab initio calculations can then be used to calculate the electronic structure, occupation levels, excitation energies, hyperfine parameters etc., more accurately. This procedure has successfully been used in several of our works, see e. g. Refs. [10, 61, 62, 63].

2.4   Modeling of Defects

What is desired from theory, is information about the properties of a *single* defect in an otherwise perfect crystal. Although today's computer facilities and the efficiency of the methods generally applied to the modeling of defects are continually growing, the number of atoms that these methods can treat is far from that in a real crystal. For the description of an isolated defect, the simulation of an infinitely extended crystal would come closest to realistic conditions. Except for the perfect crystal, this is, however, impossible within usual atomistic simulations[13]. Only a bounded area around the defect can be described, for which there are several possibilities.
The most common two possibilities are on the one hand the use of clusters and on the other hand the use of periodic boundary conditions, compare Fig. 2.2.
   In a cluster consisting of a part of the investigated material and a surface passivated with (pseudo-)hydrogen atoms one isolated defect can be modeled. The passivation of the

---

[13]An exception is the elaborate Green's functions approach [36, 37], where the infinite crystal can be described with a Green's function, so that a really isolated defect can then be modeled.
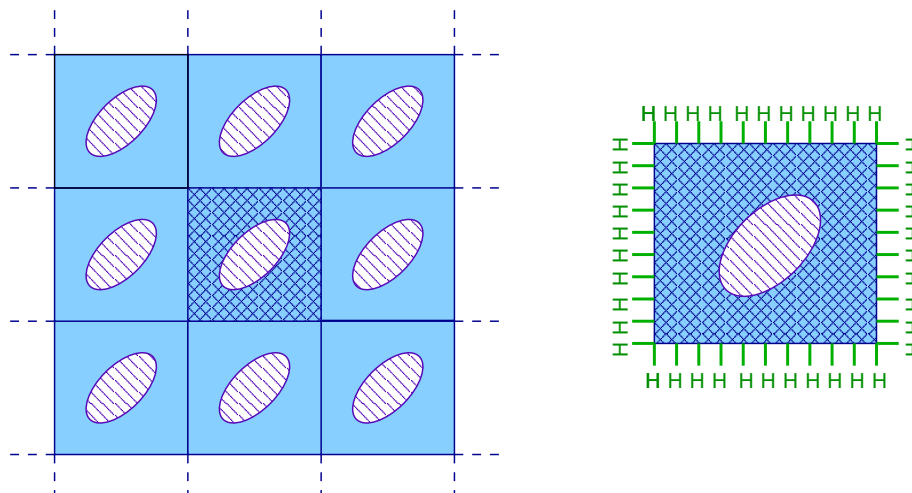
Figure 2.2: A defect modeled in a supercell (*left*) or in a (pseudo)hydrogen passivated cluster (*right*).

cluster surface is necessary to prevent the dangling bonds of the surface atoms. Since only bulk material shall be simulated, the geometric positions and the charge transfer between the outer atoms are modeled to be as they are in ideal bulk. This is achieved by defining so-called pseudo-hydrogen atoms, which then have to be put in the right position to serve their purpose. Nevertheless, the results usually depend on the symmetry of the cluster and on the position of the defect[14]. Variations of the geometric relaxation and the energy of the structure due to different distances of the defect to the passivated cluster-surface may not be underestimated. Using a sufficiently large cluster can, of course, help to keep such artificial effects small, but result in large numbers of atoms, also at the cluster-surface.

The other approach is to use periodic boundaries. This is usually achieved by using the supercell concept, in which it is assumed that all margin atoms at one side of the cell are neighbors to those atoms at the opposite side of the cell. Like this, interactions of all atoms across the supercell boundaries are accounted for and no artificial surfaces as in the cluster approach evolve. As a price, the risk of unphysical defect-defect interactions between defects in "neighboring cells" due to the created periodic images rises, since no longer an isolated defect but rather a periodic grid of defects (with a "lattice constant" induced by the supercell vectors) is modeled, compare Fig. 2.2. Also here, using a large supercell helps to reduce such influences till they are negligible. Because of the high computational costs, especially first principle methods are limited to rather small numbers of atoms, which consequently sets a limit to the size of defect complexes that can be described in these methods.

The influences of periodic images in case of supercells or of passivated surfaces in case of clusters can also be kept small by allowing only the atoms in a "core region" around the defect to relax while all outer atoms are kept fixed at their bulk positions. This, however, can put unphysical constraints on the defect and its surrounding, thus a good compromise has to be found in choosing such "boundary conditions".

In this work, all defect structures were modeled in supercells. The convergence has been tested at several examples, and according to these results the supercells for further use have been chosen. Calculations performed for the isolated vacancy in silicon have shown

---

[14]It is often difficult to position larger defects with an unsymmetric relaxation into a cluster, which preferably should have spherical symmetry because of its surface.

a clearly better convergence of the results (geometry and formation energy) with the size of the supercell in SCC-DFTB [61] than in the reference calculations with a plane wave code [64]. Obviously, the long-range effects responsible for the interaction between periodic images are suppressed more strongly in the tight-binding approach than in the plane wave description (compare also the discussion in Chapter 3). This implies that the quality of a result obtained in different methods but with the same boundary conditions cannot in general be assumed to be similar. Independent from how elaborate the used method is, there is always a need for test calculations and convergence checks. In Chapter 3 formation energies and migration energies of vacancies (and pairs of them) in 3C-SiC and 4H-SiC have been calculated in various supercells with varying boundary conditions, in Chapter 4 the same has been done for antisites.

In numerical simulations, the integrals over periodic functions in real space (compare the expressions in the previous sections) are most often evaluated by summation over their Fourier transforms in the reciprocal space. A k-point sampling of the Brillouin zone is the basis of this summation, which corresponds to an integration over the whole real space. Utilizing symmetries the number of k-points by which a good description of the system is achieved can be reduced substantially. The larger the structure in real space, the less points are needed for the sampling in reciprocal space. Especially first principle methods which are limited to smaller numbers of atoms in the simulations make, therefore, use of larger k-point schemes together with small supercells. For large supercells, a small number of k-points suffices to obtain a good description, so that very often only one k-point, namely the Γ-point $k = 0$, is used[15].

For selected structures the dependence on the k-point scheme has been checked for the SCC-DFTB calculations, but differences were usually below 0.1 eV in energy and also the geometrical differences were very small if only the Γ-point or an optimized special k-point scheme was used. Tests were made for the common ($2\times2\times2$) Monkhorst-Pack scheme[16] [65]. The plane wave and the AIMPRO reference calculations used either a small cell of 64 atoms with this special k-point scheme or a bigger cell with 128 or in selected cases also 216 atoms and only the Γ-point. In this work, the Γ-point was used throughout.

Unless otherwise stated, a ($3\times3\times3$) supercell, containing 216 atoms, was used for 3C-SiC, and a ($5\times6\times1$) supercell with 240 atoms was used for 4H-SiC. Usually, as many atoms as possible were allowed to relax.

2.5 The Diffusion Algorithm

When a defect complex has been calculated to be stable against dissociation (under certain environmental conditions), the next question that arises is, how it can be created, or, how it will behave during e. g. an annealing process. At which annealing temperature a defect complex dissociates or a vacancy or an interstitial starts to migrate through the crystal lattice is determined by the change in total energy of the structure during the migration process. Thus, the initial and the final structure of the migration process are known, and what is in demand is the saddle point geometry that separates them and whose energy difference to the initial structure defines the activation energy of the process.

---

[15] The Γ-point has also some advantages compared to other k-points. Band dispersion and broken degeneracy of localized defect levels at k-points other than the Γ-point make it difficult to detect the position of these levels relative to the valence band physically correct.

[16] Monkhorst and Pack have shown that the integration of periodic functions of a Bloch wave function over the entire Brillouin zone can be reduced to an integration over "special points" chosen in a special way for each crystal lattice, so that the computational effort is reduced essentially [65].

Starting with the initial structure, the geometrical path of all atoms in the defective region has to be determined in order to find the way that leads over the lowest energy barrier on the potential energy surface, i. e. the saddle point geometry, towards the final structure. While a minimum energy structure can in principle be obtained by relaxation of the system using a simple conjugate gradient scheme based on the minimization of the forces, some constraints have to be applied to the system for the calculation of migration paths.

Two different techniques were used in this work and are briefly described in the following paragraphs.

2.5.1 The constrained relaxation technique

The following algorithm [66] is a possibility to calculate the whole migration path of an atom from its position in the initial structure to its position in the final structure. It puts constraints onto selected atoms that are supposed to undergo the largest changes during the process, while all other atoms are allowed to relax freely.

1. Conjugate gradient relaxation of initial and final structures (DFTB) $\Rightarrow \mathbf{r}_{\text{diff}}$ (3N-dim)
2. Move mass center of *selected atoms* by $\Delta \mathbf{r}_{\text{diff}}$
3. Constrained conjugate gradient relaxation in planes $\perp \mathbf{r}_{\text{diff}}$ (DFTB)
4. Calculate new $\mathbf{r}_{\text{diff}}$ to final structure
5. Repeat (2)-(4) until final structure is reached
6. Calculation of the vibrational spectrum of the saddle point geometry
7. If required steepest descent relaxation from saddle point geometry to equilibrium geometries
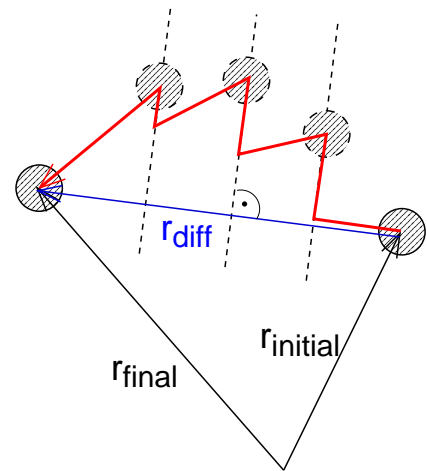
The number of steps to take between the two equilibrium positions depends on the shape of the potential energy surface. For a migration path along a rather flat energy surface, less steps are required to find the saddle point geometry with the same accuracy as for a migration path on an energy surface with large curvature in the range of the saddle point[17]. The number of atoms which are constrained during the relaxation varies. In many cases it is sufficient to constrain only one atom, e. g. for the sublattice migration of vacancies the atom that changes its site with the vacancy. If more atoms are supposed to perform a simultaneous movement, it can become necessary to constrain all these atoms. The activation energies obtained like this can be higher due to these constraints, so that the calculation possibly has to be refined in the region around the saddle point until the correct saddle point geometry has been found. That a saddle point geometry has been reached can be checked by calculating the vibrational spectrum of this structure. For a saddle point structure, the spectrum will show one imaginary mode, belongig to the migrating atom and indicating the direction of migration towards the two equilibrium structures.

From a saddle point geometry found with this technique, a steepest descent relaxation without constraints is performed to obtain the whole migration path. With a very small

---

[17]This is one point where the efficiency of the method pays off. The large number of calculations along the migration path with first principles, e. g. plane wave, codes is very time-consuming or requires parallelization and the use of supercomputers, while SCC-DFTB-calculations can be performed on common workstations in acceptable time.

movement of the constrained atoms in the positive and negative directions of the vibrational mode belonging to the saddle point, relaxation will automatically lead to the equilibrium geometries.

There are cases in which this technique is not very successful, and finding the saddle point geometry is hindered by the applied constraints. In these cases, the technique described in the following paragraph might help.

2.5.2   The activation relaxation technique (ART)

An alternative technique to determine the saddle point geometry is the *activation relaxation technique* (ART) [67]. In contrast to the technique described above, no information about the whole path is obtained, but a steepest descent relaxation is required afterwards.

Starting with an equilibrium geometry, the atoms are moved slightly in the direction of the saddle point [18]. A new force $\mathbf{G}$ can be defined with the 3N-dimensional force vector $\mathbf{F}$ of the current structure and the 3N-dimensional unit vector $\Delta\mathbf{x}$ pointing from the (initial) equilibrium structure to the current configuration:

$$\mathbf{G} = \mathbf{F} - (1 + \alpha)(\mathbf{F} \cdot \Delta\mathbf{x})\Delta\mathbf{x} \; . \tag{2.25}$$

Like in the usual conjugate gradient calculation, this redefined force $\mathbf{G}$ is calculated and the atoms moved according to it (instead of $\mathbf{F}$ in the usual relaxation). The component of $\mathbf{G}$ that is parallel to $\Delta\mathbf{x}$ has the opposite sign of $\mathbf{F}$, so that the system is forced to perform a valley up-hill movement in the energy landscape until the saddle point geometry is reached. At this point, both forces $\mathbf{G}$ and $\mathbf{F}$ are zero. The positive constant α can be varied in order to accelerate the convergence behavior, usually $\alpha = 1$ is a good choice. After this *activation* phase, a *relaxation* phase yields the path from the saddle point structure into the equilibrium configuration. As described in the previous paragraph, a small movement of selected atoms along both directions of the saddle point vibrational mode and steepest descent relaxation leads the system to the equilibrium structures. In contrast to the algorithm described afore, only the activation energy for the process is obtained directly in the first step, while the migration path has to be calculated separately in a second step.

2.6   Lattice Vibrations and Free Energies

For the calculation of formation energies of defects or activation energies of migration processes, the energies of different structures have to be compared. This is most often done by simply comparing the total energies E_{tot} obtained from e. g. supercell calculations. Spoken thermodynamically, however, the crystal (with the defect) is a great canonical ensemble, and it would be thermodynamically correct to compare the Gibbs free enthalpies

$$G = U - T \cdot S + p \cdot V + \sum_i \mu_i N_i \tag{2.26}$$

of the structures. The last term accounts for the change in particle number N_i with the chemical potential μ_i. [19]   In this work, calculations have been performed at constant

---

[18]Having a rough idea of the saddle point geometry is of advantage, since it can abbreviate the calculation time massively to have a good initial configuration. Being too far from the saddle point geometry can in some cases result in a loop around this configuration instead of converging towards the saddle point.

[19]In a diffusion process, in which the particle number remains constant, this term does not contribute, but only e. g. for the calculation of the formation energy of a defect from perfect bulk. Since it does not

pressure and volume, so the pressure- and volume dependent term pV is not relevant, here. The internal energy U consists of two parts:

$$U = E_{\text{tot}} + U_{\text{vib}} \tag{2.27}$$

The first term, the static part, is the total energy E_{tot}, as obtained from the SCC-DFTB calculation. The term U_{vib} is caused by lattice vibrations. Assuming a Planck-distribution of harmonic oscillators, U_{vib} can be written as

$$U_{\text{vib}} = \sum_{i=1}^{3N} \left\{ \frac{\hbar\omega_i}{exp(\hbar\omega_i/k_BT) - 1} + \frac{1}{2}\hbar\omega_i \right\} \ , \tag{2.28}$$

following the Einstein model in statistical physics [71]. Here, ω_i are the eigenfrequencies obtained from the calculation of the vibrational spectrum of the defect. T is the temperature.

The entropy S in Eq.2.26 is usually neglected. This is justified in many cases by the similarity of the structures that are compared, so that the change in entropy, ΔS is, indeed, very small. In some cases, as e. g. strong rearrangements of the lattice, it is, however, important to consider the term $T \cdot S$, especially at high temperatures (compare Section 4).

The entropy S consists of the configurational, the electron-hole-pair and the vibrational entropy. The configurational term is given by the number of possible configurations in which the defect can exist. The second term is usually negligible small and shall also not be discussed further. The prevailing contributions come from the lattice vibrations and can have a non-negligible influence on the energetics – depending on the temperature.

As described in detail in Appendix B, we can with

$$\left(\frac{\partial S}{\partial U} \right)_{\text{V,N}} = \frac{1}{T} \tag{2.29}$$

and U_{vib} from Eq. 2.28 derive an expression for the vibrational entropy S_{vib}. The entropy then takes the form

$$S_{\text{vib}} = k_B \sum_{i=1}^{3N} \left\{ \frac{\hbar\omega_i}{k_BT} \left[exp\left(\frac{\hbar\omega_i}{k_BT} \right) - 1 \right]^{-1} - \ln\left[1 - exp\left(\frac{-\hbar\omega_i}{k_BT} \right) \right] \right\} \ . \tag{2.30}$$

The frequencies ω_i are the local vibrational modes of the defect structure. The vibrational frequencies ω_i can be calculated within SCC-DFTB from the dynamical (Hessian) matrix

$$D_{ij} = \frac{1}{\sqrt{m_k m_l}} \frac{\partial^2 E}{\partial r_{ik} \partial r_{jl}} \tag{2.31}$$

that is defined by the second derivatives of the energy, having the eigenvalues ω_i^2. For the calculation, each atom in the defective region is slightly displaced by a distance $\pm\Delta r_i$ in three directions. Based on the finite differences in the forces in these slightly different geometries, the Hessian matrix can be built up. Its diagonalization yields the desired frequencies.

---

change anything in the derivation and we mainly will apply this formalism to diffusion processes, we leave this term in the following for clarity.

Unfortunately, the entropy is not easily accessible, neither theoretically[20] nor experimentally, making a comparison difficult. Only a few reference values, mostly force field calculations and partly of doubtful quality, are available, and the discrepancies between these values are in some cases larger than the error due to a neglect of the entropy term. However, a classification of the quality of the calculated vibrational frequencies and of the calculated entropies can be made for the vacancy in silicon. This requires the calculation of the vibrational spectra of the perfect lattice and the lattice with the vacancy.

Before this will be done, it might be meaningful to investigate the quality of the calculated vibrational spectrum of only one structure (instead of comparing two of them). First, the vibrational spectrum of ideal bulk 3C-SiC will be discussed and the SCC-DFTB-result compared to other methods, then the specific heat will be calculated for different materials, for which experimental values are available in the literature.

2.7 Applications and Test Calculations

2.7.1 The vibrational spectrum of 3C-SiC bulk

At the example of a supercell of 3C-SiC containing 64 atoms, the vibrational spectrum calculated within SCC-DFTB in Γ-point approximation has been compared to the spectra obtained within AIMPRO [35, 68] and FHI[34, 69]. These spectra, broadened with 10 cm^{-1} are shown in Fig. 2.3. The quantities discussed in the following sections were calculated using the original frequencies as done with the SCC-DFTB-spectra. The gap

Figure 2.3: The vibrational density of states for 3C-SiC, calculated using three different methods: FHI(black line), AIMPRO(blue line), and SCC-DFTB(red line). For better clearness, the result of FHI has been drawn to the positive ordinate, while for the other two curves the sign has been chosen opposite.

---

[20]The calculation of vibrational spectra is very time consuming, limiting ab initio methods to small defective regions. Other, more approximative, methods often do not reach the accuracy in the description of the forces, which is required for the calculation of vibrational frequencies.

Table 2.1: Uppermost phonon modes below and lowest phonon modes above the frequency gap (3C-SiC). The results of the different methods and the experimental values [70] are given. The values are given in [meV], values in parentheses are in [cm^{-1}].

Method	Atoms	ω_1	ω_2	Gap
SCC-DFTB	64	78.8 (635.5)	105.1 (847.7)	26.3 (212.1)
SCC-DFTB	216	78.7 (634.8)	106.4 (858.2)	27.7 (223.4)
AIMPRO	64	67.3 (542.8)	91.3 (736.4)	23.9 (192.8)
FHI	64	79.3 (639.6)	91.0 (734.0)	11.7 (94.4)
Experiment		76.5 (617.0)	91.0 (734.0)	14.5 (117.0)

between the acoustical and optical modes is described even better by the calculation with the FHI-code[34], if a (2×2×2) Monckhorst-Pack k–point scheme [65] is used. Table 2.1 compares the results for the uppermost phonon modes below and lowest phonon modes above the frequency gap are compared for the different methods and the experimental data. A comparison of the states below the gap shows a very good agreement between the SCC-DFTB-results and these FHI-results. Above all, the frequencies of the two highest modes below this gap are at the correct position. The modes above the gap, i. e. the optical modes have too high frequencies. The AIMPRO-results show a different behavior: the optical modes are described correctly, while the frequencies of the modes below the gap are too low. By a multiplication with a factor ≈ 0.9, the SCC-DFTB-frequencies can nearly exactly be transformed into the AIMPRO-frequencies. A correction of the size of the gap towards the experimental value can neither in SCC-DFTB nor in AIMPRO be achieved by a simple scaling factor.

For 4H-SiC, the vibrational frequencies below the frequency gap are described as well

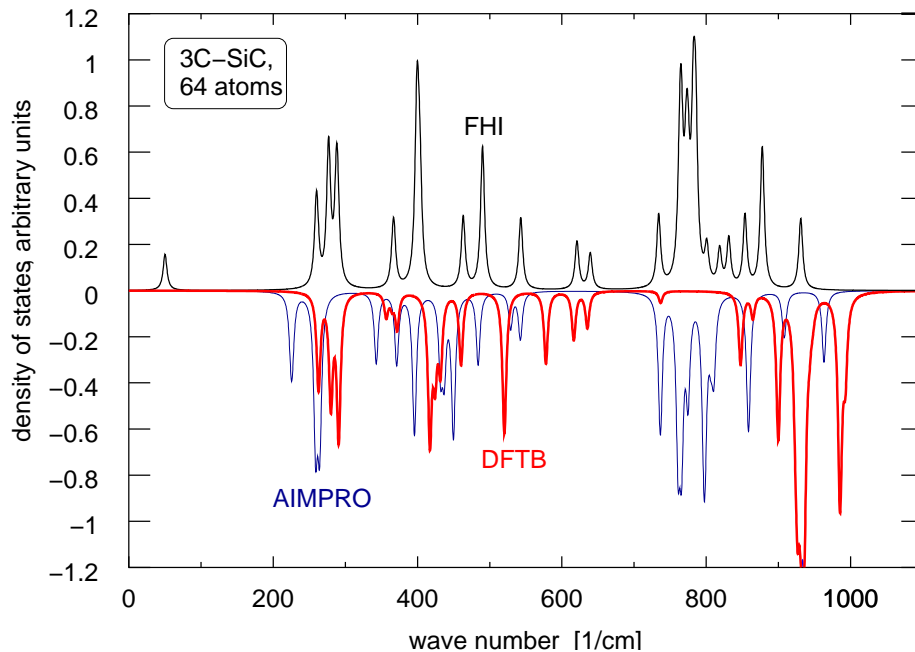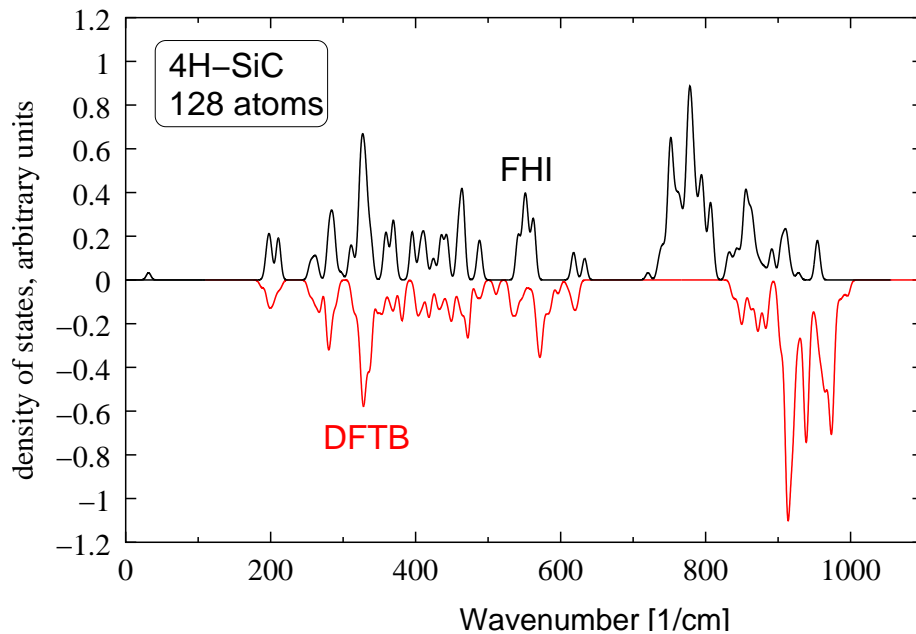**Figure 2.4:** The vibrational density of states for 4H-SiC, calculated in two different methods: FHI(black line) and SCC-DFTB(red line). For better clearness, the result of FHI, has, again, been drawn to the positive ordinate, while the SCC-DFTB result is mirrored to the negative ordinate.

as for 3C-SiC in SCC-DFTB compared to the FHI calculation, while, again, the higher frequencies are overestimated, compare Fig. 2.4. For these calculations, a 4H-SiC super-cell containing 128 atoms was used in both methods. In this case, also for the ab initio calculation only the Γ-point was used. It can, therefore, not be attributed to the use of the Γ-point approximation that the frequency gap is too large in the SCC-DFTB- and AIMPRO-calculations. A reason for the better result of the FHI-calculation may be found in the use of a plane-wave basis in FHI, in contrast to localized basis sets used in SCC-DFTB and AIMPRO. The collective character of the vibrational frequencies might be better described within this extended basis.

The qualitative agreement is sufficient for the purpose of this work, where only integrated quantities are needed[21]. How these are affected by the deviations between the different methods is subject to the following two sections.

2.7.2 Heat capacity of diamond, silicon, and SiC

The heat capacity C_v at constant volume can be calculated from Eq. 2.28 as the derivative of U with respect to T:

$$C_\mathrm{v} = \left(\frac{\partial U_\mathrm{vib}}{\partial T} \right)_\mathrm{V} = \sum_{i=1}^{3N} \left\{ k_B \left(\frac{\hbar\omega_i}{k_B T} \right) \frac{exp\left(\frac{\hbar\omega_i}{k_B T} \right)}{(exp\left(\frac{\hbar\omega_i}{k_B T} \right) - 1)^2} \right\} \tag{2.32}$$

For high temperatures, C_v approaches $3Nk_B$, in agreement with the rule of Dulong and Petit[22].
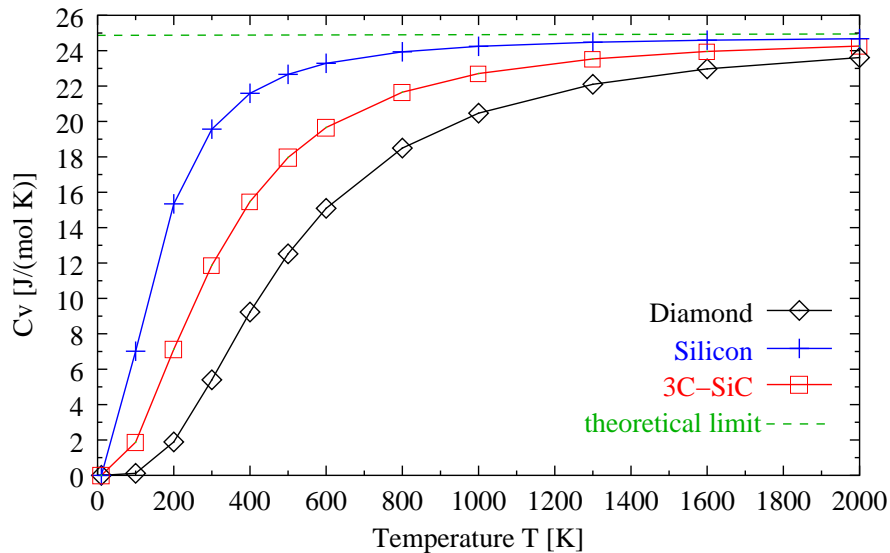
Figure 2.5: Temperature dependence of C_v for diamond, silicon, and 3C-SiC. The dashed line denotes the theoretical limit of $3Nk_B$, which is reached by any solid for temperatures above the material dependent Debye temperature Θ_D.

---

[21]Further calculations have shown a correct description of localized modes due to defects in the lattice. A nearly perfect agreement between AIMPRO and SCC-DFTB has e. g. been found for the modes induced by the antisite pair, see Chapter 4.

[22]For very low temperatures, i. e. $T < 0.1 \cdot \Theta_D$, the description becomes wrong, and the Debye model [71] has to be used. In this work, however, only the high temperature range is of interest
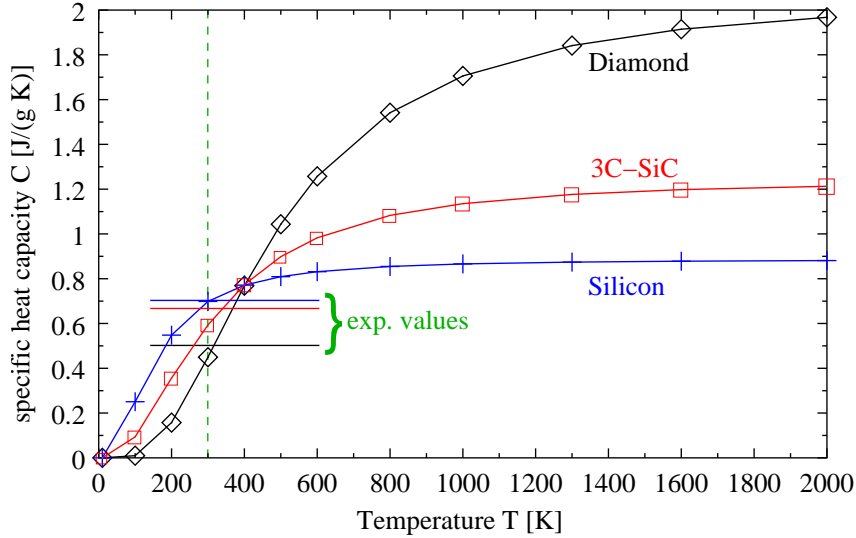
Figure 2.6: Calculated specific heat capacity for diamond, silicon, and 3C-SiC compared to experimental values at T=300 K.

In Fig. 2.5, C_v is plotted for diamond, silicon, and 3C-SiC in a temperature range between zero and 2000 K. The shape and the limit of the curves and the differences between the materials, as e. g. the Debye temperature Θ_D (Si: 741 K (exp: 650 K), C: 2021 K (exp: 2230 K), SiC: 1456 K (exp: 1600 K)), are described correctly.

Calculating now the (mass dependent) specific heat c, we obtain c=0.450 J/(g·K) for diamond, c=0.699 J/(g·K) for silicon, and 0.563 J/(g·K) for 3C-SiC, which agrees well with the experimental values of 0.502, 0.703, and 0.678 J/(g·K) as given in Ref. [72] for T=300 K. The whole curves are shown in Fig. 2.6.

Experimental results and the temperature dependence as predicted by the Einstein model is described qualitatively correct by the vibrational spectrum calculated numerically within SCC-DFTB.

2.7.3   Absolute entropy in different methods

Using the frequencies obtained by different computational methods as described above, the vibrational entropy and the internal energy of vibration can be calculated. Fig. 2.7 shows a comparison of the temperature dependence of the absolute entropy, scaled by the number of atoms in the supercell used. Since the vibrational spectrum calculated with the FHI-code reproduces the experimental properties best (compare last section), it shall be used as a reference curve. The slope of the AIMPRO curve is then slightly too large, while that of the SCC-DFTB-curve, calculated in the 64-atom supercell, is by about the same amount too flat. The SCC-DFTB-calculation in the 216-atom supercell, however, reproduces the FHI-curve nearly exactly. The internal energy U does neither show strong deviations between the different methods, except for the very low temperature range, which is not described correctly in the underlying theoretical model[23] and, furthermore, not of interest in the applications.

---

[23]The description of the low temperature behavior of the thermal energy U is described correctly by the Debye Model, which in contrast to the Einstein model yields the experimentally observed $C_v \sim T^3$ behavior at low temperatures [71].
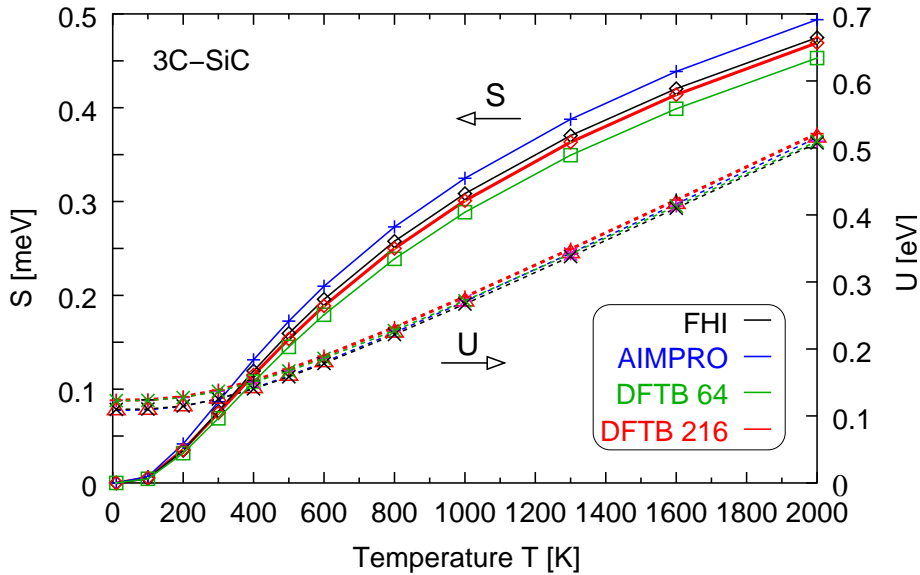
Figure 2.7: Temperature dependence of the absolute entropy S (*left ordinate*) and the internal energy U (*rigt ordinate*), scaled by the number of atoms in the used supercell.

Since the errors in the description of frequencies concern any structure calculated with one method in a similar way, the variations of the quantity of interest between the different methods, i. e. the difference in entropy ΔS between two structures, can be expected to be even smaller.

2.7.4   Formation entropy

The calculation of formation entropies of defects is by far more complicated and not as straightforward as the calculation of formation energies. Calculating the entropy as described before, a strong dependence on the cluster and supercell size is found. The reasons for this dependence and how to correct for it is discussed considering the example of an isolated vacancy in diamond and in silicon.

The periodic images of a defect strongly influence the formation entropy which is an un-avoidable artifact due to the supercell approach, compare Section 2.4. This is certainly also true for formation energies, but the effect is by far not as large as for the long-range character of formation entropies[24]. It has been found that, in order to simulate the behavior of a defect in a nearly infinite crystal, modeling is done best by using an *embedded cluster scheme*, i. e. dividing the fully relaxed supercell with the defect into a region around the defect, the *"cluster"*, in which all atoms are treated dynamically, and an outer region in which the atoms are treated as static [73, 74, 75], compare Fig. 2.8.

Calculations with several different methods for the modeling of the vibrational behavior have shown that the cluster size must be essentially smaller than the size of the supercell. On the other hand the cluster size must be large enough to provide a correct description of the defect. In Ref. [73], the authors used cells of about 5000 atoms to model an isolated vacancy in copper, whereof only about 100 to 500 atoms were then included in the calculation of the vibrational spectra. In Ref. [75], cells of up to 16384 atoms were used,

---

[24]Because of the change in the *collective* vibrational properties the defect causes the entropy is to a large deal stored in the material outside the defect region.

treating up to 1289 atoms dynamically[25]. Such large supercells are, of course, far beyond the supercell sizes that can be treated within atomistic calculations, especially since the diagonalization of the dynamical matrix does not only take a very long time but is also associated with numerical problems.

Nevertheless, with the corrections proposed by these authors, entropy calculations can also be performed in our smaller supercells containing 216 atoms. The comparison with the calculation in a supercell with 512 atoms for the vacancy in silicon shows that a consistent picture can be obtained.

To calculate the formation entropy of a vacancy, the same calculations have to be performed for the supercell with the vacancy and for the perfect supercell using the same cluster size. To correct for the different number of atoms, the results for the perfect lattice have to be multiplied by $(N - 1)/N$, where N is the number of atoms in the perfect lattice cluster.

Figure 2.8: The supercell used for modeling the defect is divided into a spherical *cluster* which contains the defect core and is treated dynamically within the atomistic calculation (dark violet), and an outer sphere (light blue) which is treated by an continuum theoretical approach.

The observed $1/N$ dependence [74] in the convergence behavior of the so calculated entropy S_{form} can be understood from elasticity theory by writing the total entropy as $S = S_{\text{core}} + S_{\text{elastic}}$. So far, only the first part, S_{core}, has been considered by the calculation described afore. Due to its long-range character, however, a large part of the entropy, S_{elastic}, is stored in the region outside the cluster. This elastic part has, therefore, to be added to the values obtained by the atomistic calculation. It can be divided into two "correction terms" that can be calculated in elasticity theory. We consider a spherical isotropic continuum of radius R. For a point defect with spherical symmetry, as can be assumed for the vacancy, only radial strain occurs, and so we can get with Eq. C.11 (see Appendix C) in spherical coordinates

$$\nabla^2 \delta = 0 \qquad \text{with} \qquad \delta = \delta(r) \tag{2.33}$$

for the dilatation δ. Since $\delta = \nabla \cdot \mathbf{u}$, the displacement field has to be of the form

$$\mathbf{u}(\mathbf{r}) = \left(\frac{A}{r^3} + B \right) \cdot \mathbf{r} \tag{2.34}$$

with constants A and B to be determined by the boundary conditions.
The first (smaller) correction to the entropy can then be understood immediately: The components of the strain tensor ε_{ij} are defined as

$$\varepsilon_{ij} = \frac{1}{2} \left(\frac{\partial u_i}{\partial x_j} + \frac{\partial u_j}{\partial x_i} \right) \ , \tag{2.35}$$

thus showing a $1/R^3$ dependence for the $\mathbf{u}(\mathbf{r})$ of Eq. 2.34. As derived in detail in Ref. [76], the R-dependence of the elastic constants transmits to the entropy, such that the entropy

---

[25]In these calculations Born-Mayer- and Morse-potentials were used for the entropy calculations.
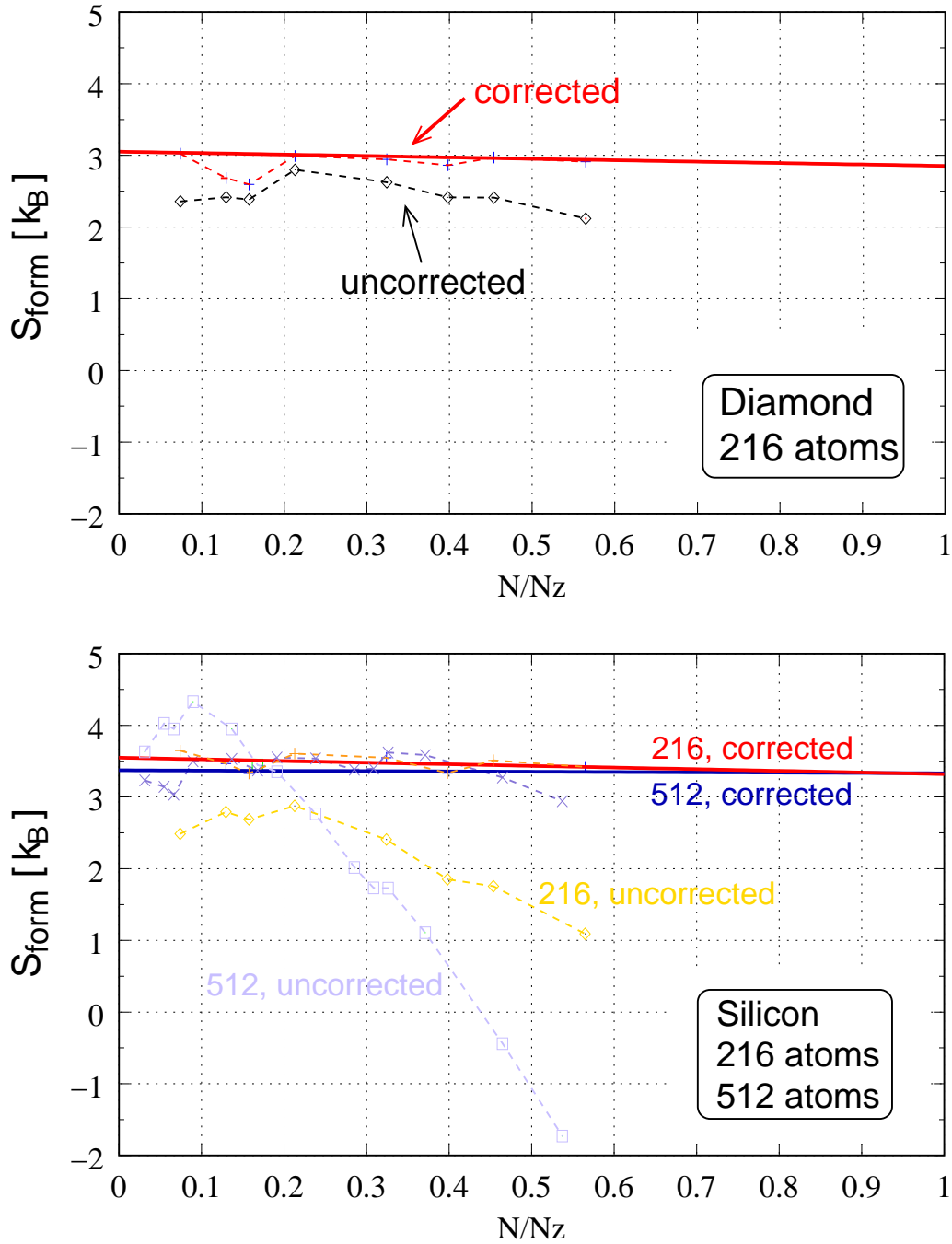
Figure 2.9: Formation entropy of the vacancy in diamond (upper diagram) calculated in a supercell with N_Z=216 atoms and in silicon (lower diagram) calculated in a supercell with N_Z=216 atoms (yellow: uncorrected, orange: corrected, red: linear fit) and with N_Z=512 atoms (light blue: uncorrected, blue: corrected, dark blue: linear fit), restricting the vibrations to N atoms in the shells surrounding the vacancy.

stored outside a sphere with radius R is proportional to $1/R^3$. Since the number N of atoms is proportional to R^3, the correction

$$\Delta S_1 = \frac{const.}{N} \tag{2.36}$$

is obtained for the formation entropy [73] with a constant depending on the material. Following the procedure proposed by Hatcher et al. [73], the entropy values obtained like

this, require a further correction ΔS_2 that accounts for the image forces introduced by the periodic images of the defect and the entropy stored in the up to now neglected region of the crystal outside the defect cluster. The size of this correction can, again, be calculated from the free energy [76], resulting in

$$\Delta S_2 = K \cdot \alpha \cdot \Delta V^{\text{image}} \tag{2.37}$$

with the bulk modulus K, the thermal expansion coefficient α and the volume change ΔV^{image} due to image forces. This term that can be split into two parts shall be motivated in the following. The idea for this finite size correction comes again from continuum theory: at the boundary of the supercell – for simplicity we regard the boundary of an outer sphere of radius R_a and assume isotropic dilatation – , the inevitably vanishing displacements of the atoms (due to the boundary conditions) introduce a volume change

$$\Delta V = -\Delta V^{\text{tot}} \left(\frac{R_i}{R_a} \right)^3 \approx -\Delta V^{\text{tot}} \left(\frac{N}{N_Z} \right) \tag{2.38}$$

at the inner sphere of radius R_i (which contains the dynamically treated cluster in our calculations)[73, 76]. ΔV^{tot} is the relaxation volume of the defect in an infinitely extended crystal. In reality however, we always have a finite crystal, terminated by the crystal surfaces. In supercell calculations, the simulated region is limited by the supercell boundaries. The volume change is influenced by these constraints, and we will calculate what part of the volume change ΔV^{tot} is caused by image forces. At the surface of the sphere ($r = R$) representing the crystal no stress is left:

$$\sigma_{\text{rr}}(r = R) = 0 \ . \tag{2.39}$$

Expressions for the strain ε_{rr} and dilatation δ follow from Eq. 2.34:

$$\varepsilon_{\text{rr}} = -\frac{2A}{r^3} + B, \qquad \delta = \nabla \cdot \mathbf{u} = 3B \ . \tag{2.40}$$

With Eq. C.9 from Appendix C the constant B can be expressed in terms of A:

$$\sigma_{\text{rr}}(r = R) = 0 \tag{2.41}$$
$$\Leftrightarrow \quad 2\mu\varepsilon_{\text{rr}} + \lambda\delta = 0$$
$$\Leftrightarrow \quad B = \frac{4\mu}{2\mu + 3\lambda} \cdot \frac{A}{R^3} \ .$$

The displacement field $\mathbf{u}$ becomes then

$$\mathbf{u}(\mathbf{r}) = A \left(\frac{1}{r^3} + \frac{4\mu}{2\mu + 3\lambda} \cdot \frac{1}{R^3} \right) \cdot \mathbf{r} \tag{2.42}$$
$$= \mathbf{u}_s(\mathbf{r}) + \mathbf{u}_d(\mathbf{r})$$

with a shear term $\mathbf{u}_s$ and a dilatation term $\mathbf{u}_d$ [77].
Let the displacement at the radius r_{core} of the defect core be $u(r_{\text{core}}) = \eta r_{\text{core}}$, then the remaining constant A can be written as

$$A = \frac{1}{1 + \frac{4\mu \, r_{\text{core}}^3}{(2\mu + 3\lambda)R^3}} \cdot \eta \, r_{\text{core}}^3 \underset{\frac{r_{\text{core}}}{R} \ll 1}{\approx} \eta r_{\text{core}}^3 \ . \tag{2.43}$$

Now it can be seen that the dilatation

$$\delta = 3B = \frac{12\mu\eta \, r_{\text{core}}^3}{(2\mu + 3\lambda)R^3} \tag{2.44}$$

tends to zero for an infinite crystal, but this is not true for a finite crystal[26]. At the surface of the outer sphere ($r = R$), the shear part of Eq. 2.42 causes the volume change

$$\delta V_s = 4\pi R^2 \cdot u_s(R) = 4\pi\eta r_{\text{core}}^3 \ , \tag{2.45}$$

i. e. the volume change the defect would cause in an infinitely extended crystal. The dilatation term yields

$$\delta V_d = 4\pi R^2 \cdot u_d(R) = 4\pi\frac{4\mu}{2\mu + 3\lambda}\eta r_{\text{core}}^3 \ . \tag{2.46}$$

Using instead of the Lamé constants μ and λ the poisson ratio

$$\nu = \frac{\lambda}{2(\lambda + \mu)} \ , \tag{2.47}$$

we get

$$\delta V_d = 4\pi\frac{2(1 - 2\nu)}{1 + \nu}\eta r_{\text{core}}^3 \ , \tag{2.48}$$

for the dilatation part and thus the total volume change becomes

$$\delta V_{\text{tot}} = 4\pi\frac{3(1 - \nu)}{1 + \nu}\eta r_{\text{core}}^3 \ . \tag{2.49}$$

The dilatation part arises only due to image forces at the surface of the sphere. From Eqns. 2.48 and 2.49 it follows that

$$\frac{\delta V_d}{\delta V_{\text{tot}}} = \frac{2}{3}\left(\frac{1 - 2\nu}{1 - \nu}\right) \ , \tag{2.50}$$

setting the volume change due to image forces which is needed for the entropy correction in relation to the total volume change [77].
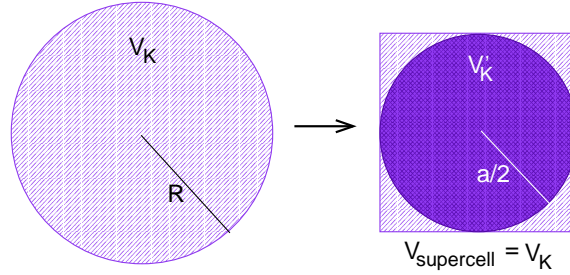
Figure 2.10: Sphere inscribed in a supercell

Up to now we used a sphere of radius R in our considerations, but the atomistic calculations are performed in cubic supercells with the same volume and edge length a. The postulation of isotropy may not apply to the marginal regions of the supercell due to the influence of neighboring cells. We, therefore, have to go over to a sphere with radius $a/2$ that is inscribed in the supercell, see Fig. 2.10. Since the relation of these volumina is

$$\frac{V_K'}{V_K} = \frac{V_K'}{V_{\text{supercell}}} = \frac{\frac{4\pi}{3}\left(\frac{a}{2}\right)^3}{a^3} = \frac{\pi}{6} \ , \tag{2.51}$$

---

[26]and especially not for the from the macroscopic view small supercells

Table 2.2: Data used for the calculation of the entropy of formation of an isolated vacancy in diamond and silicon. Experimental values from Ref. [78]

	Diamond	Silicon
B	536 GPa	100 GPa
ν	0.1	0.29
α	$7.1 \cdot 10^{-6}$ K^{-1}	$2.6 \cdot 10^{-6}$ K^{-1}
N_Z	216	216; 512
n_{core}	17	17
ΔV_{core}	$-1.330 \cdot 10^{-30}$ m^3	$-2.137 \cdot 10^{-29}$ m^3
V_{tot}	$1.226 \cdot 10^{-27}$ m^3	0.431 resp. $1.024 \cdot 10^{-26}$ m^3

the smaller volume $\delta V_d \cdot \frac{\pi}{6}$ has to be used in Eq. 2.37. Expressing the total volume change by the volume change of the defect core

$$\frac{\Delta V_{\text{tot}}}{\Delta V_{\text{core}}} \approx \frac{R_a^3}{r_{\text{core}}^3} \approx \frac{N_Z}{n_{\text{core}}} \ , \tag{2.52}$$

the final expression for the correction of the formation entropy becomes

$$\Delta S = \frac{const.}{N} + K\alpha \cdot \left(\frac{2}{3} \frac{(1-2\nu)}{(1-\nu)} \frac{\pi}{6} - \frac{N}{N_Z} \right) \cdot \frac{N_Z}{n_{\text{core}}} \cdot \Delta V^{\text{core}} \ . \tag{2.53}$$

Due to the numerous assumptions and approximations, i. e. spherical symmetry of the defect core, the cluster and the complete supercell in order to use the macroscopic continuum theory for a furthermore rather small number of atoms as can be treated in our supercell calculations, results can only be expected to be of qualitative accuracy. Nevertheless, the results presented in the next section for isolated vacancies in diamond and silicon are quite encouraging.

2.7.5 The vacancy in diamond and silicon

The procedure described above has been applied to the calculation of the formation entropy of isolated vacancies in diamond and silicon, using the data given in Table 2.2. A temperature of T=2000 K has been chosen, where the high temperature approximation is valid and the formation entropy becomes temperature independent.

The results of these calculations are shown in Fig. 2.9. In the upper diagram, the values of S_{form} of the vacancy in diamond obtained from the calculation without any corrections are plotted over the relative cluster size N/N_Z (black diamonds), the corrected values are plotted in red. The straight red line has been fitted to these values, so that the desired value for $N = N_Z$ can be extrapolated, resulting in $S_{\text{form}} = 2.85$k$_B$. Variations of the corrected values are less than ± 0.3k$_B$. For the isolated vacancy in diamond, the corrections are, thus, very small.

The description of the vacancy in silicon turns out to be much more complicated. The diverging behavior of the uncorrected values for the entropy in the supercell with 216 atoms
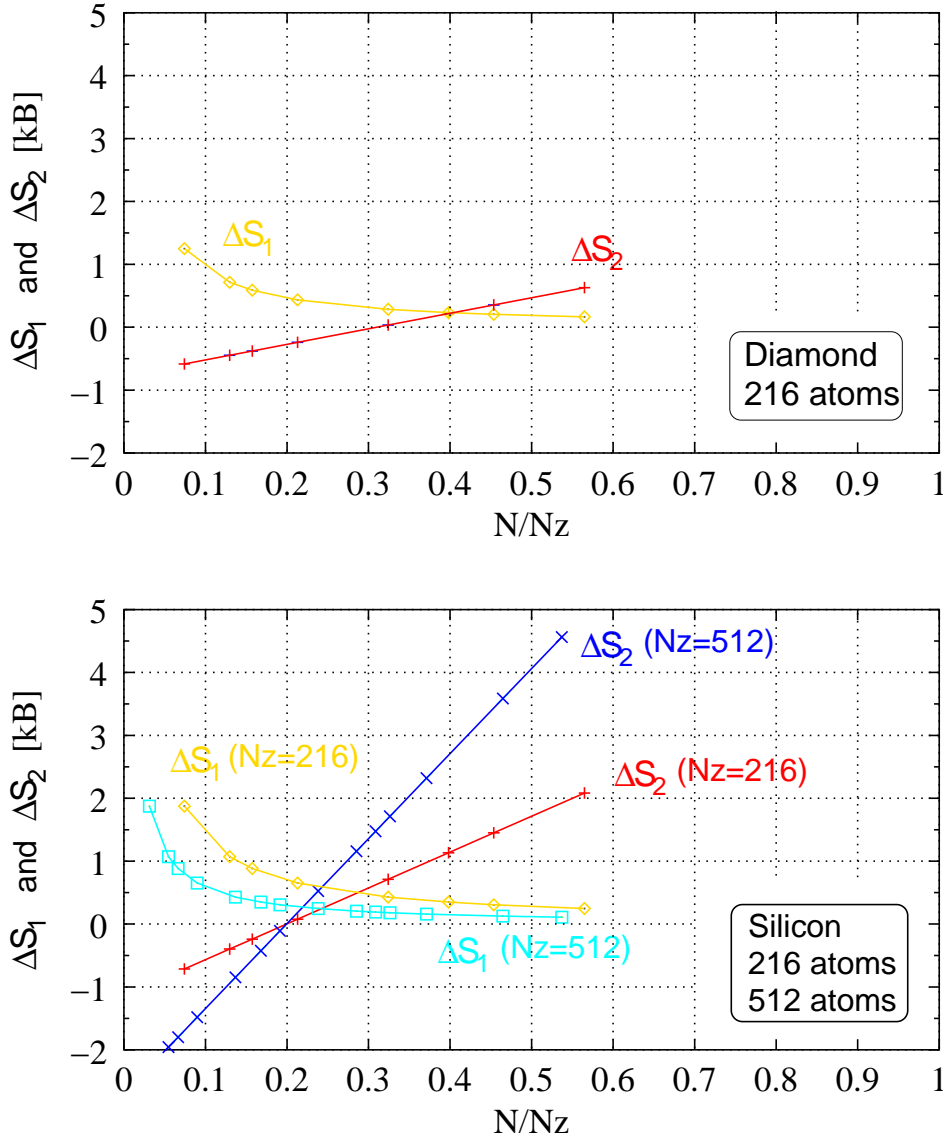
Figure 2.11: Corrections to the formation entropy for the vacancy in diamond (upper diagram) and silicon (bottom).

is found to be even worse in the larger supercell with 512 atoms, – an observation made by e. g. Fernández et al., as well [74]. Taking a closer look at the corrections derived in the previous section, this observation can be understood, because the second term of the correction is proportional to ΔV_{core}, which is by about one order of magnitude larger for the vacancy in silicon than for the vacancy in diamond (see Table 2.2).

In Fig. 2.11, the two corrections to the formation entropy are plotted separately for the vacancy in diamond (upper diagram) and in silicon (lower diagram). While in case of diamond only a very small correction is obtained, the strong relaxation yields large image forces and, accordingly, large corrections for the vacancy in silicon. The first correction ΔS_1 is only important for small cluster sizes N, where the largest part of the entropy is stored in the region outside the cluster. Additionally, it is compensated in part by the second correction ΔS_2. This part of the correction is rather small for diamond, as well, but it is of the same order of magnitude as the core entropy for the vacancy in silicon.

The total formation entropy of the vacancy in silicon, again obtained by extrapolation of

the corrected values to $N = N_Z$, results in 3.32 k$_B$ (216 atoms) and 3.33 k$_B$ (512 atoms), compare Fig. 2.9. Variations are slightly larger as in case of diamond, but still in the range of ± 0.5k$_B$.

The values obtained with the described corrections are of a proper order of magnitude, as a comparison with the literature shows. In Refs. [43, 79], the entropy of formation (in the high temperature approximation) is calculated for the unrelaxed vacancy in silicon, based on a force constant model and including the nearest or next nearest neighbors of the vacancy, only. In Ref. [79] a Green's function technique is used to investigate the influence of the force constant model on the formation entropy. Although in most simple force constant models a value of ≈ 1.7 k$_B$ can be derived for an unrelaxed vacancy in any tetrahedrally bonded material, the results obtained with different methods vary between 1.5 k$_B$ and up to 8 k$_B$ and are highly sensitive to the force constants used. For the relaxed vacancy a value of ≈ 3k$_B$ as is also obtained by first principle calculations [80], is commonly accepted. Small local changes in the force constants can result in large changes in the formation entropy, making a good description of the forces desirable.

The reason for the discrepancies between the formation entropies calculated within different methods is to find in the fact that the vacancy in silicon is one of the most complicated defects with respect to a converged energetical and electronic structure, compare also the discussion in Chapter 3. Even for the formation energies convergence starts at supercell sizes larger than 216 atoms, as has been extensively investigated in Ref. [61, 64]. Convergence problems have to be ascribed to the extremely flat potential energy surface of silicon, which in a high degree influences the quality of the dynamical matrix and thus the vibrational frequencies.

Concluding this section, we have found a possibility to calculate the vibrational entropy of defects. The absolute values calculated within SCC-DFTB are in rather good agreement with ab initio results. Including certain corrections, we can obtain reasonable values for the formation entropies of point defects, as shown at the example of isolated vacancies in silicon and diamond[27]. The migration entropies discussed in Chapters 4 and 5 do not suffer from the problems discussed in this section and can, therefore, be expected to be less sensitive in their description. Firstly, forces in SiC can be calculated much more accurate than in silicon, and, second, errors due to artificial constraints by the supercell boundaries or by periodic images can be expected to be of similar magnitude in the compared structures, whereas the comparison of a defective and a perfect supercell as required for the calculation of formation entropies is something completely different. The most important quantity to influence the calculated entropies is the accuracy of relaxation of the atoms surrounding the defect, compare Ref. [81].

---

[27]The equations given can also be applied to other defect structures, as e. g. interstitials, with minor changes. The treatment of dopant atoms requires further consideration. This is, however, not subject of this work.

Chapter 3

Vacancies and Interstitials

The first section of this chapter gives a brief overview of our results for the formation energies of silicon- and carbon–vacancies as well as next neighbor pairs of them. The SCC-DFTB results are compared to literature data, in order to get an impression of the expected accuracy of the energies calculated in various methods. Afterwards, the sublattice migration of both vacancies is discussed, since it is not only of interest as a "pure" process but also plays a key role in the formation of aggregates of other defects, as is described in Chapters 4 and 5. As a competing process to the sublattice migration, the formation of vacancy–antisite pairs is discussed, reviewing the most important findings about the $V_C\,C_{Si}$ pair, which in turn appears in the discussion of the creation of antisite pairs (Chapter 4) and the recovery of free charge carriers in nitrogen doped material (Chapter 5).

The second section of the chapter is dedicated to carbon split interstitials, and in the third section, finally, the role silicon- and carbon vacancies play in the migration processes of these interstitials is briefly described, clarifying the long-range effects defects can have on activation energies in SiC.

The results of this chapter do not claim to be exhaustive, but only those matters that are of interest for the following two chapters are pointed out, here.

3.1 Vacancies

As unavoidably in a large number created defects, vacancies are most important in the situation directly after ion implantation: Vacancy assisted processes have been discussed in Section 2.1.3, and in Chapter 4 they will turn out to be essential for the mobility of antisites. The ion bombardement causes monovacancies on both sublattices as well as pairs of a silicon- and a carbon vacancy, i. e. divacancies, and possibly also larger vacancy aggregates.

3.1.1 Formation energies

A comparison of the formation energies of vacancies and divacancies in 3C- and 4H-SiC is given in the following tables. Supercells of different sizes and the dependence of the calculated formation energies on the number of atoms around the defect that were allowed to relax during structure optimization have been compared in order to get an impression of how our method (SCC-DFTB) behaves under varying outer conditions and under which conditions results come closest to the available ab initio results. These literature values

have been obtained with the Finnish plane wave based LDA-code "FINGER" using a cubic supercell with 128 atoms, which all were allowed to relax freely[11]. The results for 3C-SiC are shown in Table 3.1.

The same calculations have been performed for the 4H-polytype of SiC, but here it has to be distinguished between the two different sites – (quasi-)cubic or hexagonal – for each of the vacancies, compare Fig. 1.4. All possible orientations have been calculated, and the formation energies are shown in Table 3.2. The last four lines of Table 3.2 show the binding energies of the divacancies on the different sites.

In a binary semiconductor, the formation energy of vacancies naturally depends on the

Table 3.1: Formation energies of vacancies in 3C-SiC, calculated within SCC-DFTB. The last column shows literature values from Ref. [11]. Especially for the carbon vacancy and for the divacancy, the formation energies vary rather strongly with the size of the supercell and the constraints in the calculation. In the last line of the table the binding energy of the divacancy $V_C V_{Si}$, obtained by subtracting the third row from the sum of the first two rows, is shown. In the columns denoted with "2NN", relaxation was limited to nearest and next nearest neighbors of the defect. All values in [eV].

Defect	128 cell, 2NN	128 cell, all	216 cell, 2NN	216 cell, all	128 cell, all [11]
V_{Si}	8.32	8.31	8.67	8.66	7.79
V_C	4.70	4.70	4.39	4.12	2.77
$V_C V_{Si}$	10.44	10.38	8.95	8.85	7.22
$V_C V_{Si}$	2.58	2.62	4.12	3.93	3.34

Table 3.2: Formation energies of vacancies in 4H-SiC. The differences between the hexagonal and cubic sites are smaller than the variations due to different constraints in the calculation. These are smaller than for 3C-SiC. The last four lines show, again, the binding energies of the divacancy in all possible orientations.

Sites	128 cell, 2NN	128 cell, all	240 cell, 2NN	240 cell, all	Ref. [11]
$V_{Si}{}^{cub}$	8.81	8.78	8.57	8.54	8.37
$V_{Si}{}^{hex}$	8.82	8.79	8.58	8.55	8.26
$V_C{}^{cub}$	4.62	4.39	4.32	4.05	4.07
$V_C{}^{hex}$	4.73	4.49	4.51	4.16	4.21
$V_C{}^{cub}V_{Si}{}^{cub}$	9.01	8.93	8.85	8.77	7.74
$V_C{}^{cub}V_{Si}{}^{hex}$	9.13	9.07	8.88	8.80	8.36
$V_C{}^{hex}V_{Si}{}^{cub}$	9.12	9.03	9.01	8.90	8.34
$V_C{}^{hex}V_{Si}{}^{hex}$	9.04	8.97	8.89	8.81	8.00
$V_C{}^{cub}V_{Si}{}^{cub}$	4.42	4.23	4.03	3.83	4.36
$V_C{}^{cub}V_{Si}{}^{hex}$	4.30	4.11	4.02	3.80	3.77
$V_C{}^{hex}V_{Si}{}^{cub}$	4.42	4.24	4.07	3.80	3.90
$V_C{}^{hex}V_{Si}{}^{hex}$	4.51	4.31	4.20	3.90	4.27

chemical potential of the constituents of the material, since the stoichiometry is changed by the creation of a vacancy. To be able to compare our results with the available literature data and not to destroy the clarity of the description needlessly, formation energies are only given for one selected set of chemical potentials μ_{Si} and μ_C. Throughout this work, expression A.11 with $\Delta\mu = 0$ has been used to calculate formation energies (see Appendix A). Since $\Delta\mu = 0$ means per definition (Eq. A.10) $\mu_{Si} = \mu_C$, this choice of $\Delta\mu = 0$ describes stoichiometric conditions, which are also experimentally most common.

A comparison of the SCC-DFTB-results in Tables 3.1 and 3.2 for the second next neighbor relaxed and fully relaxed structures shows for both supercell sizes only small variations, in most cases ≈ 0.1 eV.

For defects that induce a stronger and/or more long-range lattice distortion in their neighborhood, partly substantially larger differences can occur due to constrained relaxation, compare the analogous discussion in Chapter 4 for antisites and antisite pairs. This must be considered for the choice of the supercell so that the number of atoms that are allowed to relax can be chosen large enough but artifacts due to periodic images of the defect are kept small at the same time.

The energy differences between the calculations in the 128-atom supercell on the one hand and the 240-atom supercell on the other are slightly larger, in most cases ≈ 0.2 eV. The largest difference was found for the divacancy in 3C-SiC, where the 128-atom supercell is obviously to small to describe the relaxation around the defect correctly. The fact that this is not the case in 4H-SiC can be explained by the form of the 128-atom supercell, which has a fcc-basis in the 3C- but a sc-basis in the 4H-polytype, leading to different defect-defect distances across supercell boundaries.
The energy differences between the SCC-DFTB-results and the ab initio results are a little larger than those between the different supercells within SCC-DFTB. This can have several reasons. In principle, more accurate values should, of course, be expected from ab initio calculations due to the less approximative description of the electronic structure in these methods.

On the other hand, most ab initio calculations suffer from being limited to small supercells which can both lower or increase formation energies and migration barriers due to artificial interactions between the periodic images of the defect. An example where large variations in the formation energies occur if using different supercells and k-point sampling schemes is the isolated vacancy in silicon[1]. In Ref. [64], Puska et al. present systematic investigations on this matter, reporting a very slow and oscillating convergence behavior of the formation energies and the geometrical relaxation of V_{Si} in all charge states with the supercell size. The principle behavior of the formation energy obtained by these plane wave LDA-calculations could be confirmed by our DFTB-calculations for supercells of up to 512 atoms [61, 82]. Convergence is, however, reached for much smaller supercells in our calculations. This observation might be ascribed to a larger influence of periodic images on the widely extended plane wave basis, while the tight-binding description obviously suppresses such artificial effects better. This is also suggested by the induced relaxation around the vacancy, which, in contrast to the plane wave calculations, does not change

---

[1]As already pointed out during the discussion of the calculation of formation entropies in the previous chapter, silicon is due to its very flat potential energy surface an extremely critical case. The effects studied at its example can, therefore, be expected to be considerably smaller in a material that is less critical in this respect.

substantially for supercells larger than 128 atoms in the DFTB-calculations [61, 82]. Furthermore, even different ab initio methods show variations of the same order of magnitude. The low formation energy calculated for the carbon vacancy in Ref. [11] (with the plane wave code FINGER) is e. g. not obtained with a similar plane wave code (FHI) [12], the results of which ($\approx$4 eV) are clearly closer to the SCC-DFTB results. A reason for these deviations lies certainly in the free choice of certain parameters in the construction of the pseudopotentials as well as other partly more technical quantities.

Having this in mind, one should rather set great store by a good consistent picture of the results within the method concerning the absolute values. The qualitative results, however, can be compared with those of other methods. These compare quite well within SCC-DFTB and the available ab initio data as the results for the vacancies in this chapter as well as the results for antisites in Chapter 4 show. The 216-atom cell (3C) and the 240-atom cell (4H) with a large number of free relaxing atoms turn out to yield converged results and come in most cases closest to the literature value (where also all atoms were relaxed). These supercells are used in the following if nothing else is explicitly said.

Up to now, we have only challenged the accuracy of the absolute values for the formation energies of vacancies and divacancies calculated with SCC-DFTB compared to results of ab initio methods. The accuracy of SCC-DFTB has been discussed, while that of the literature values has been accepted unquestioningly. However, further test calculations with the Green's functions based LMTO method have shown that also these first principle values have to be handled with care, as explained in the following.

As discussed in the previous chapter, the local density approximation (LDA) in density functional theory (DFT) has the disadvantage of an incorrect description of the energy gap of semiconductors. Furthermore, it has been mentioned in Section 2.2 that there are several techniques to account for this failure and correct for the size of the energy gap and thereby also the position of localized levels in the gap. The energy gap obtained for a material within LDA depends on the basis set used. The ab initio methods used for the reference calculations, i. e. the FHI code and the FINGER code, use a plane wave basis with s-, p-, and d-basis functions for the creation of the pseudopotentials. In SCC-DFTB, a minimal basis of s- and p-orbitals is used, instead.

Since it is not possible without very large expenses in the plane wave codes or in SCC-DFTB to change the basis set, the LMTO results shall illustrate the dependence of the gap as obtained in pure LDA, i. e. without any corrections, on the basis set. For cubic SiC, a minimal basis (sp) yields an energy gap of 2.91 eV, including the d-orbitals leads to a considerably smaller gap of 1.29 eV, and further including the f-orbitals results in a gap of 1.63 eV. These values have to be compared to the experimental gap of 2.4 eV for 3C-SiC. In SCC-DFTB, the minimal basis (sp) leads to a large band gap of 5.9 eV, thus clearly further from the experimental value[2]. In spite of the obviously incorrect description of the conduction band in SCC-DFTB with the sp-basis, it has also advantages for the description of formation energies if the gap is too large, as will become clear in the following.

The effects of a Baraff-Schlüter correction [55], which is applied to the finished supercell calculation, and a fully selfconsistent correction calculated in the Green's function based LMTO with the scissor operator technique [54] has been investigated at the example of the silicon vacancy and the carbon vacancy in 3C-SiC.

In the Baraff-Schlüter correction, the calculated gap is scaled to the experimental gap, and the localized defect levels in the gap are also shifted by this scaling factor, weighted

---

[2]This strong overestimation has not only to be ascribed to the minimal basis, but is typical for tight-binding methods.

Table 3.3: The effect of two different corrections for the LDA-gap on the formation energies of V_C, V_{Si}, and $V_C V_{Si}$. "B-S" shows the formation energy with the Baraff-Schlüter correction, "Scissor" includes the fully selfconsistent correction with the scissor operator, instead. For comparison, the last column shows the SCC-DFTB results for the 216 atom supercell, allowing all atoms to relax, freely. Below the line the binding energy is shown. All values in [eV].

Defect	E_{form} [11]	B-S (FHI)	Scissor (LMTO)	SCC-DFTB
V_{Si}	7.79	8.26	8.40	8.66
V_C	2.77	3.57	3.78	4.12
$V_C V_{Si}$	7.22	–	8.47	8.85
$V_C V_{Si}$	3.34	–	3.71	3.93

with their overlap with the conduction band. In contrast to this correction, the scissor operator allows to correct not only the localized gap levels, but the whole valence band selfconsistently. In contrast to the Baraff-Schlüter correction of the gap levels only, resonant levels in the valence band are accounted for by this method. Due to the empirical character of this kind of corrections, most often no corrections are made in ab initio calculations. Only rarely, the Baraff-Schlüter correction is used in ab initio methods, while the selfconsistency and the neglected correction of the valence band is hoped not to have a significant influence, which is, in fact, true in many cases[3].

All literature values in Tables 3.1 and 3.2 are LDA-results without any corrections. Table 3.3 shows the influence of the two different corrections on the formation energies of V_C, V_{Si} and $V_C V_{Si}$. The third column shows the literature values from Ref. [11] plus the Baraff-Schlüter correction calculated within the FHI code. Due to the overlap of the occupied gap-levels with the conduction band, a correction of 0.47 eV has to be added to the formation energy of the silicon vacancy. For the carbon vacancy, a larger value of 0.80 eV has been calculated. A similar calculation within the LMTO method, but correcting the gap levels selfconsistently, yields very similar values. Adding the fully selfconsistent correction of the gap levels and the whole valence band to the results of Ref. [11] results in values even closer to the SCC-DFTB results, compare the fourth column. Especially for the silicon vacancy, formation energies have become very similar. A larger difference remains for the formation energy of the carbon vacancy, and consequently for the diva-cancy. An FHI calculation yielded 7.75 eV for the formation energy of the silicon vacancy, and 4.35 eV for the carbon vacancy (uncorrected values) [68]. Adding the Baraff-Schlüter corrections to these results leads to 8.2 eV and 5.1 eV for V_{Si} and V_C, the full correction results in 8.36 eV and 5.36 eV.

3.1.2 Migration of vacancies

In this section, the description of non-equilibrium structures is investigated at the example of activation energies for the sublattice migration of isolated vacancies. In the binary lattice of a compound semiconductor like SiC, a vacancy can migrate through the sublattice by a second neighbor atom moving onto the vacant site. This sublattice migration process (compare Section 2.2.3) is also the basis of many other migration processes: In Chapter

---

[3]In case of the saddle point structures for sublattice migration of V_C and V_{Si} the importance of the correction of the whole valence band will become clear, see the next section.

Table 3.4: Comparison of calculated activation energies (i. e. the energy difference between minimum and saddle point geometry) for vacancies in 3C-SiC and 4H-SiC (only last column). For comparison, values obtained by SCC-DFTB for the cubic (c) sites in 4H-SiC are also given. Besides the polytype, the number of atoms in the supercell and the number of relaxed atoms is shown. All values in [eV].

E_{active}	Ref. [12, 13] 216, 2NN	Ref. [68] 128, 2NN	DFTB 128, 2NN	DFTB 128, full	DFTB 216, full	DFTB 512, full	DFTB, 4H 240, full (c)
$V_C{}^{2+}$	5.2		6.4		5.8		5.8
V_C	3.5	4.0	5.1	4.6	4.8	4.8	4.7
$V_C{}^{2-}$			4.4		3.9		4.1
$V_{Si}{}^{2+}$			5.3		4.3		4.4
V_{Si}	3.4	3.6	4.9	3.9	3.9	4.1	4.1
$V_{Si}{}^{2-}$	2.4		4.3		3.5		3.6

4, it is shown that the mobility of vacancies is prerequisite for the mobility of isolated antisites, and also for the formation of nitrogen complexes the mobility of vacancies is of importance, see Chapter 5.

Unfortunately, the number of available ab initio calculations for comparison is very restricted, which on the other hand suggests to use a more approximative method like SCC-DFTB for a systematic series of investigations[4].

The description of migration processes shows the same behavior as that of the formation energies: in most cases, allowing more atoms to relax lowers the activation energies as well as using larger supercells[5]. Though the SCC-DFTB-energies are throughout higher than the available plane wave results, the same trend can be observed in both methods for the different charge states: activation energies increase the more positively the defect is charged.

A comparison of the SCC-DFTB-results of Tables 3.1- 3.4 draws a consistent picture of both formation- and activation energies. The results obtained in the supercell containing 512 atoms confirms that the results in the smaller cell (216 atoms) are already converged. The deviation of the activation energies of the sublattice migration of vacancies compared to the plane wave results sets limits to the expectable accuracy of SCC-DFTB in the first line, but as well of other, also ab initio methods. The attempt to correlate the calculated activation energies with experimentally more direct accessible annealing temperatures (see Chapter 5) assumes, however, first of all the consistency of the calculated data rather than an absolute accuracy of less than 0.5 eV. Furthermore, the same considerations as in the previous section suggest that the LDA results of Ref. [12, 13] and [68] require a correction due to the underestimated band gap.

Including the Baraff-Schlüter corrections for the silicon vacancy and the saddle point struc-

---

[4]For more accurate values of the most important processes found with SCC-DFTB, an ab initio calculation can then follow. As pointed out in the previous chapter, the calculation of migration paths is rather time consuming, for which reason many ab initio calculations are limited to those migrations processes, where the saddle point geometry can be derived from e. g. symmetry arguments, so that only this structure can then be relaxed under certain constraints to obtain the activation energy.

[5]Larger supercells can also result in higher formation energies, as for instance in the example of the isolated vacancy in silicon [64]. A general statement about the variation of formation energies or migration energies with the boundary conditions cannot be made.

Table 3.5: The effect of two different corrections for the LDA-gap on the activation energies of sublattice migration of V_C and V_{Si}. "B-S" shows the activation energy with the Baraff-Schlüter correction, "Scissor" includes the fully selfconsistent correction with the scissor operator, instead. For comparison, the last column shows the SCC-DFTB activation energy (216 atom supercell, full relaxation). All values in [eV].

Defect	E_{activ} [68]	B-S (FHI)	Scissor (LMTO)	SCC-DFTB
V_{Si}	3.6	3.6	4.5	3.9
V_C	4.0	4.7	6.2	4.8
ΔE_{activ}	0.4	1.1	1.7	0.9

Defect	E_{activ} [12, 13]	B-S (FHI)	Scissor (LMTO)	SCC-DFTB
V_{Si}	3.4	3.4	4.3	3.9
V_C	3.5	4.2	5.7	4.8
ΔE_{activ}	0.1	0.8	1.4	0.9

ture does not change the results, since in both cases the correction amounts to 0.4 eV [68]. For the carbon vacancy, however, a large difference occurs, since several defect levels are in the energy gap of the saddle point structure, but only one in case of the vacancy. The Baraff-Schlüter corrections are 0.79 eV for the carbon vacancy and 1.44 eV for the saddle point, leading to a correction of 0.65 eV for the energy barrier [68]. Adding these corrections to the LDA results listed in the second and the third column yields 4.2 and 3.4 eV for V_C and V_{Si} for the values of Ref. [12, 13] and 4.7 and 3.6 eV for the values of Ref. [68]. Tables 3.5 summarize the corrections applied to both the literature values of Ref. [12, 13] and Ref. [68]. Including the full correction of the valence band and gap levels leads to substantial changes, since large contributions to the saddle point energies arise from the correction of the valence band, which are not covered by the simple Baraff-Schlüter correction, compare the third and fourth columns in Tables 3.5. Comparing now the SCC-DFTB results in the last column with the corrected LDA values shows that at least part of the required corrections is implicitly included in the SCC-DFTB energies, which lie between the partly and the fully corrected LDA values. In contrast to the ab initio LDA calculations with a considerably too small band gap, also localized levels that are close to the conduction band are clearly separated, and no correction due to the overlap with the conduction band is required. Especially for the description of high negative charge states of defects, less technical problems occur than in LDA calculations.

Regarding the energy differences also between different ab initio calculations with and without the two corrections, the discussion of energy differences of less than 0.5 eV becomes obviously meaningless. Considerably more important is the qualitative description, which expresses itself e. g. in the difference of the activation energies for the sublattice migration of carbon vacancies and silicon vacancies. The last lines in Tables 3.5 show this energy difference. While especially the literature values of Ref. [12, 13] suggest an activation of the sublattice migration of both vacancies at approximately the same temperature (since the activation energy difference is negligibly small), the corrected LDA activation energies and the SCC-DFTB activation energies suggest that sublattice migration of the carbon vacancy should first be activated at several hundred degrees Kelvin higher temperatures[6].

---

[6]A correlation between activation energies and temperatures will be made in Chapter 5
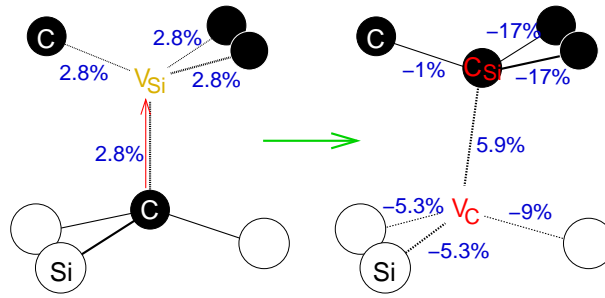
Figure 3.1: By the migration of one of its carbon ligands towards the vacant site, the silicon vacancy can transform into the $C_{Si} V_C$ pair. Relaxation induced changes of the bond lengths are given with respect to the ideal Si-C bond length 1.88 Å.

This finding could only recently be affirmed experimentally by EPR measurements on annealing studies [21], in which the signal of the carbon vacancy in as-grown samples could still be detected after that of the silicon vacancy had vanished. An exact value for the annealing temperature of V_C, i. e. the temperature that suffices to activate sublattice migration, is not yet available.

3.1.3 Vacancy – antisite pair formation

A process that can be activated at much lower cost than the sublattice migration of a silicon vacancy as described above is the movement of one of its carbon ligands into a silicon vacancy. For the vacancy and the antisite on cubic lattice sites, the atomistic model of this process is drawn schematically in Fig. 3.1. The relaxed geometry of the neutral $V_C C_{Si}$ pair has C_{1h} symmetry and is sketched at the right hand side of the figure, showing a rather strong contraction of two of the C-C bonds around the carbon antisite, which itself moves away from the vacancy, while the silicon ligands of the carbon vacancy relax inwards.

The initial and final structures as well as the saddle point geometry in 4H-SiC are also shown in Fig. 3.2 together with the energy diagram that shows the change in energy during the process. The resulting $C_{Si} V_C$ pair is by 1.8 eV more stable than the silicon vacancy.
  The carbon atom does not migrate along the direct connecting line between the vacant silicon site and its initial site, but is slightly displaced from this line, leading to a slightly asymmetric saddle point geometry. A comparatively low energy barrier of 1.7 eV has to be overcome during this process, thus, according to Eq. 2.6, it should be expected to happen much more frequently than sublattice migration ($E_{activ} \approx 4$ eV). At temperatures sufficient to activate sublattice migration, the recombination barrier of 3.5 eV can be overcome, such that the $V_C C_{Si}$ pairs can transform back to silicon vacancies which then can move to neighboring sites. With an activation energy of ≈ 4.6 eV, i. e. nearly the value obtained for sublattice migration of V_C, the dissociation of the carbon vacancy from the $V_C C_{Si}$ pair is clearly less likely than this back-transformation to the silicon vacancy.

Already in 1990, Itoh et al. observed V_{Si} to anneal out at 750° C [84]. An atomistic model for the underlying diffusion mechanism was, however, missing. Since sublattice migration of V_{Si} requires much higher activation energies than the formation of $V_C C_{Si}$ pairs which would also cause a decrease in the signal intensity of V_{Si}, we proposed the process $V_{Si} \longrightarrow V_C C_{Si}$ as an explanation for the first annealing step of V_{Si} [9], while sublattice migration should be expected to happen first at higher temperatures (compare the correlation made
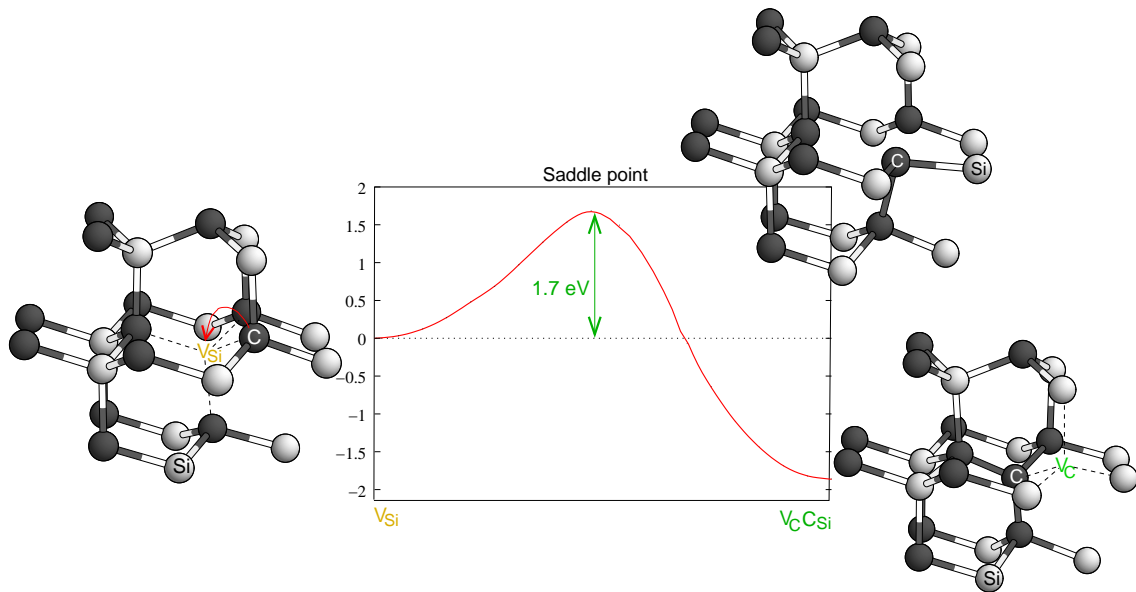
Figure 3.2: By the migration of one of its carbon ligands towards the vacant site, the silicon vacancy can transform into the $C_{Si} V_C$ pair. An activation energy of 1.7 eV is required for this migration process, and the resulting pair defect is by 1.8 eV lower in energy. The saddle point structure shown above the energy diagram is asymmetric, with the migrating carbon atom slightly displaced from the direct connecting line.
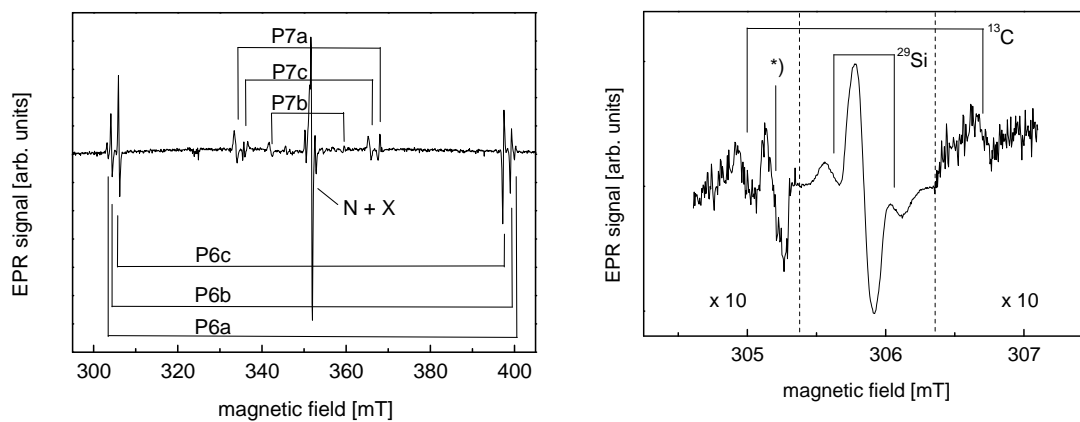

Figure 3.3: Two of the spectra that served for the identification of the P6/P7 spectrum with the $V_C C_{Si}$ pair (taken from Ref. [10]). *Left:* X-band EPR spectrum of neutron irradiated and annealed 6H-SiC, measured under illumination. *Right:* Hyperfine structure of the P6c low field EPR line. The intensity ration of the hyperfine satellites to the central line corresponds to the interaction with 4-8 silicon nuclei and one carbon nucleus.

in Chapter 5).

Based on these results, an identification of $V_C C_{Si}$ with the so-called P6/P7 EPR spectrum, see the left part of Fig. 3.3, could later on be realized by using a combination of two theoretical methods (SCC-DFTB and LMTO-ASA) with the experimental investigations of neutron irradiated 6H-SiC by Lingner et al. [10, 83]. In earlier works, these P6/P7 spectra were attributed to nearest neighbor vacancy pairs [85], and in fact, the divacancy

$V_C V_{Si}$ can, according to our LMTO-ASA calculations, explain most of the experimental findings concerning the excitation scheme and the hyperfine splittings. The hyperfine structure measured by Lingner indicates, however, the presence of *one prominent carbon nucleus*, see the right diagram in Fig. 3.3. This observation and the rather high activation energy for sublattice migration of V_C and V_{Si} rule out the divacancy as an atomistic model for the P6/P7 spectra and limits the possible candidates to the antisite pair $C_{Si} Si_C$ and the $V_C C_{Si}$ pair.

The mechanism for the creation of antisite pairs is expected to require higher temperatures than 750°C, see Chapter 4. Furthermore, the excitation energies of <0.2 eV calculated for the antisite pair, deviate clearly from the ≈1 eV measured by MCDA (magnectic circular dichroism of the absorption). These optical transitions, the symmetry, the annealing behavior and the observed hyperfine splittings can only be explained by the remaining candidate, the $V_C C_{Si}$ pair.

Using the optimized geometry of $V_C C_{Si}$ obtained from SCC-DFTB calculations, the hyperfine splittings could be calculated within LMTO-ASA. The localization of the electronic levels which give rise to the hyperfine splittings allowed us to determine the charge state of the observed pair to be doubly positive[7].

A detailed description of the properties of $V_C C_{Si}$ can be found in Refs. [10, 83, 86]. The identification of the proposed pair defect with an experimentally observed spectrum shows first successful applications of SCC-DFTB to the description of point defects and mechanisms of their migration. In addition, the procedure underlines the importance of using various methods, both experimental and theoretical, to obtain a complete picture of the properties of defects and their annealing behavior.

The $V_C C_{Si}$ pair itself turns out to play an important role in the creation of antisite– and nitrogen–related complexes, which are subject to Chapters 4 and 5.

The simplicity of the above described mechanism for the silicon vacancy suggests that an analogous mechanism should exist for the carbon vacancy, which is observed to anneal out at even lower temperatures (≈200° C) in irradiated material [14]. Calculations could, however, show that the $Si_C V_{Si}$ pair, which would result from the migration process, is instable, with the silicon antisite recombining immediately with the silicon vacancy [9]. The process $V_C \longrightarrow Si_C V_{Si}$ does, accordingly not exist, as could also be confirmed by plane wave calculations[8] [12].

3.2 Interstitials

During the implantation process, the implanted ions kick out atoms from their lattice sites and move on as long as their energy suffices to do so, before they are finally built in. Accordingly, interstitials are created in the same amount as vacancies, so that they are supposed to play an important role in the annealing processes that are the central subject of this work.

As carbon interstitials play the most important role in the mechanisms investigated in this

---

[7]The geometry of the doubly positive pair deviates less from C_{3v}–symmetry than that of the neutral pair shown in Fig. 3.1. Details can be found in Ref. [10, 83].

[8]The activation energies obtained with these calculations for the creation of the $V_C C_{Si}$ pair (≈2 eV) agrees quite well with our 1.7 eV.

work, we limit the description of interstitials to them. Silicon interstitials do not contribute essentially to the process of especially nitrogen migration (see Chapter 5) which can be attributed to their stability mainly in higher positive charge states [12], the strong lattice deformation due to the size of the silicon atoms and thereby higher migration barriers. A further reason is the attitude of nitrogen atoms to prefer the carbon site (see Chapter 5), intimating a carbon related interstitial process.

The most stable carbon interstitials in SiC are carbon split-interstitials, where two C–atoms share one C-site, such that one of them and its two Si-ligands are in a plane perpendicular to the plane spun up by the other C and its two ligands, see Fig. 3.4. The defect has D_{2d}-symmetry[9] with a highly contracted C-C-bond (26.6 % compared to the ideal SiC bond length) between the interstitial atoms that is with 1.38 Å even about 10 % shorter than the ideal bond length in diamond. The silicon ligands are strongly pushed outwards, so that for the four Si-C bonds around the defect a contraction of only 4.8 % is left.
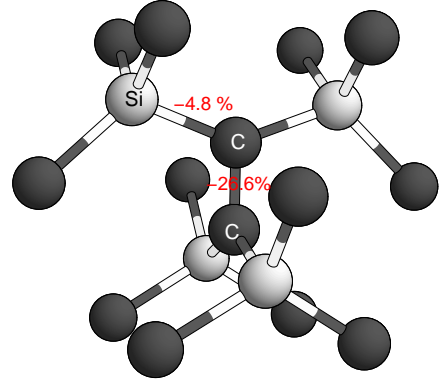

Figure 3.4: Geometry of the $(CC)_C$ split-interstitial

This $(CC)_C$ split-interstitial can move through the lattice by the migration of one of its C-atoms to the next C-site. In 3C-SiC, this migration requires $\approx$2.9 eV, while in 4H, the activation energy depends on the direction, see Fig. 3.5. Here, the lowest activation energy, $\approx$2.9 eV, is needed for a migration along the [0001]-direction, while a migration along [10$\bar{1}$0] is least favorable.
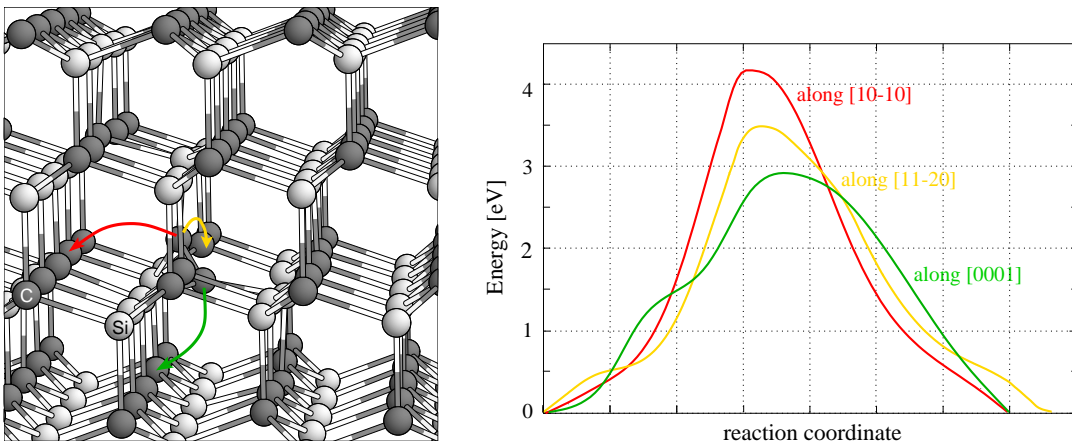

Figure 3.5: *Left:* The migration of a $(CC)_C$ split-interstitial in 4H-SiC to a neighboring C-site along the crystal directions [11$\bar{2}$0], [10$\bar{1}$0] and [0001]. *Right:* Energies along the migration path. The lowest activation energy is needed for a migration along the [0001]-direction.

For the $(CC)_C$ split-interstitial in 3C-SiC, molecular dynamic (MD) simulations were per-

---

[9]This remains valid for all charge states less negative than 2-. In this case, the symmetry axis of the defect is slightly inclined, resulting in a C_{1h} symmetry. The energy difference, though, between this and the D_{2d} configuration is only very small.

formed. The temperature simulation profile was chosen as a linear increase (200 K/fs) up to a certain maximum temperature that was then kept constant for fifty femtoseconds, followed by a linear decrease to zero temperature again.
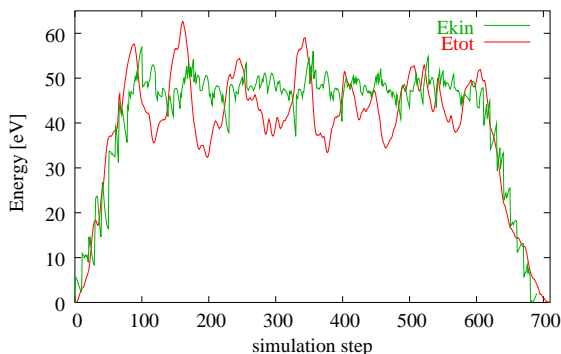

Figure 3.6: The diagram shows the total energy and the kinetic energy of the structure during the MD simulation at T=1700 K. After 80 steps of linear increase, the maximum temperature has been reached. The kinetic energy is determined by the specified temperatures, the abrupt changes in the total energy indicate structural changes.

Already during this short simulation time, some effects were observed: at a maximum simulation temperature of T=1000 K, only a rotation of the interstitial on its site could be observed. At T=1500 K, the two carbon atoms started to part with each other, but the energy seemed to be not sufficient to disrupt them definitely. A further increase to a maximum temperature of T=1700 K was enough to activate the sublattice migration process described above. An additional rotation of the defect at the new site was also observed. Fig. 3.7 shows some snapshots of this simulation. Below the structures in Fig. 3.7, the total energy of the whole structure is shown over the simulation step. The complete total energy curve as well as the kinetic energy are shown in Fig. 3.6.

Starting from the $(CC)_C$ split-interstitial (upper left part of Fig. 3.7, defect atoms marked with a red C), one of the C-atoms parts from the other (upper right, maximum of simulation temperature reached). In the third step a bond to another C (labeled with a blue C) is formed, with which in the fourth step a $(CC)_C$ split-interstitial forms. This $(CC)_C$ turns (several times) on its site (fifth picture), until the final structure (bottom right corner) is reached (structure cooled down to T=0 K). Although the temperatures in MD simulations have to be treated with care, the temperature found here agrees well with the temperature range assigned to this process in Chapter 5.

3.3 Interstitial Recombination with Vacancies

Since especially low energy implantation creates a large number of close vacancy–interstitial (Frenkel) pairs, recombination processes of such defects are as important for a complete picture of what happens during annealing as long-range diffusion. For silicon- and carbon-vacancies and carbon split-interstitials, the recombination mechanism depending on the initial distance of the defects has been investigated. This leads to a definition of a capture radius of the vacancies for this split-interstitial, which determines from which distance on sublattice migration becomes the more important mechanism compared to direct recombination.

A carbon split-interstitial can be first neighbor of a silicon vacancy. The consequence is a direct recombination without an energy barrier separating the structures.
If a carbon vacancy happens to be a second neighbor of a $(CC)_C$, there are already non-vanishing energy barriers to be overcome for the recombination. Depending on the orientation of the $(CC)_C$ to V_C, energy barriers of 0.0, 0.15 or 0.34 eV were calculated with
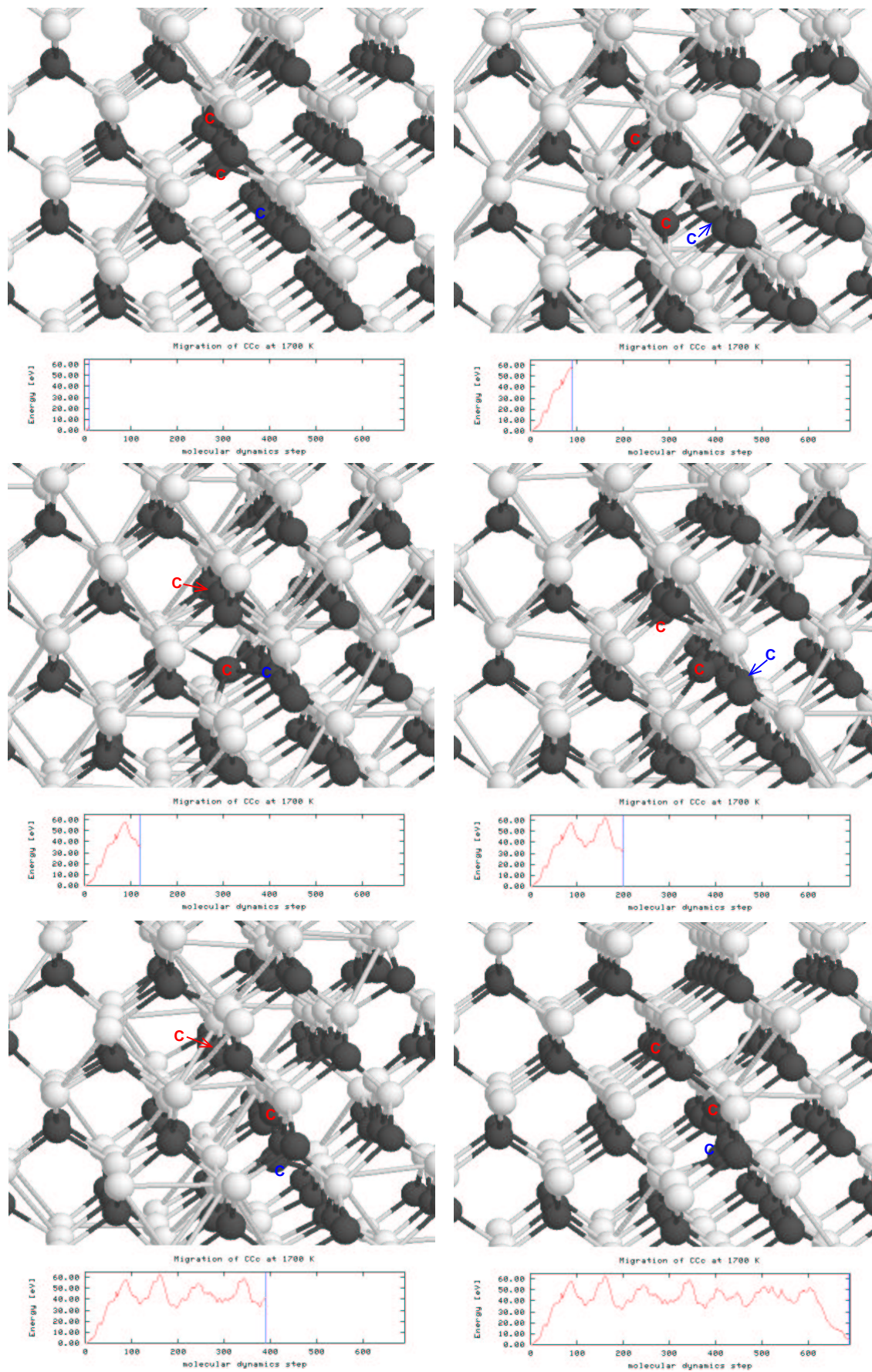
Figure 3.7: Snapshots of a molecular dynamics simulation of the migration of a $(CC)_C$ with a maximum temperature of T=1700 K. See text for details.

energy gains of 11.1, 10.0 or 11.1 eV due to recombination.

For a V_{Si} in a third neighbor distance, the highest barrier was found to be 0.91 eV (variations between different orientations are smaller than for the second neighbor V_C), while the energy gain is 12.2 eV.

Finally, a carbon vacancy in fourth neighbor distance results in a barrier of 0.98 eV, gaining 11.9 eV by recombination.

These results show the quite long-range influence of V_C and V_{Si} on $(CC)_C$ which can be understood from the large distortion the split-interstitial causes in its neighborhood. The very small energies needed to activate the recombination together with the high energy gains create a strong thermodynamical driving force for vacancy-interstitial recombination which might explain the annealing stage at 200°C for the carbon vacancy in as-irradiated material. The energy barriers and gains obtained for the silicon vacancies show furthermore that not only recombination to the perfect lattice, but even to carbon antisites is likely.

The sublattice migration mechanism for long-range diffusion will, according to these results, become dominating for interstitial–vacancy distances larger than five neighbors at the earliest. Depending on the defect densities and the uniformity of the defect distribution after implantation, this mechanism may start after the recombination of close vacancy–interstitial pairs has terminated, when vacancies and interstitials are left at larger distances, only.

Chapter 4

Aggregation of Antisites

Antisites belong to the intrinsic defects with the lowest formation energies in SiC. Nevertheless, their existence has not yet been proved experimentally. The reported observation of the silicon antisite with EPR and ENDOR measurements [87] could not be proved uniquely. For the isolated carbon antisite, there is no hint from the experimental side, caused by its electrical inactivity and therefore invisibility to common characterization methods.

Nevertheless, the results of Chapter 3 strongly suggest the existence of antisites after implantation processes. During the post-implantation annealing phase, they may play an important role in the formation of complexes of either intrinsic or extrinsic defects (compare also Chapter 5). Therefore, their migration and aggregation behavior is worth to be investigated.

Furthermore, recent photoluminescence measurements indicate a strong correlation between the local vibrational modes measured for the D_I luminescence and those calculated for the pair of a carbon and a silicon antisite. The conditions under which the D_I luminescence is measured also suggest the presence of silicon vacancies in the sample [88], which agrees well with the mechanism we propose for the creation of antisites in the following section.

Before we turn to the investigation of creation mechanisms for the antisite pair, its formation energy in 3C-SiC and 4H-SiC as well as its vibrational spectrum are discussed.

4.1 The Antisite Pair $C_{Si} Si_C$

4.1.1 Formation Energy of $C_{Si} Si_C$

In 4H-SiC, formation energies of the two types of single antisites C_{Si} and Si_C on the cubic and hexagonal sites of the crystal lattice have been calculated. The formation energies obtained with SCC-DFTB and ab initio results from Ref. [89] for the antisite pair in the different possible orientations are listed in Table 4.1. Below the line, the binding energies of the pairs are given. Various supercell sizes and numbers of relaxed atoms have been tested. The analogous results for 3C-SiC are shown in Table 4.2.

The energy differences between the hexagonal and cubic sites of the 4H-lattice and the different orientations of the pairs are of the same order of magnitude as the energy differences between the different supercells and restrictions. The same is true for a comparison of 3C-SiC and 4H-SiC. In 3C-SiC, the comparison with the ab initio results from Ref. [7] shows that especially the carbon antisite has a much lower formation energy within the SCC-DFTB calculations than in the ab initio calculation. Consequently, also the $C_{Si} Si_C$ pair

Table 4.1: Formation- and binding energies of antisites and antisite pairs in 4H-SiC. All values in [eV].

Sites	128 cell, 2NN	128 cell, all	4H-240, 2NN	4H-240, all
C_{Si}^{cub}	3.12	2.96	2.70	2.51
C_{Si}^{hex}	3.22	3.05	2.80	2.60
Si_C^{cub}	4.78	4.48	4.36	4.01
Si_C^{hex}	4.68	4.36	4.65	4.01
Si_C^{cub}-C_{Si}^{cub}	5.19	4.95	4.76	4.49
Si_C^{cub}-C_{Si}^{hex}	5.13	4.86	4.71	4.42
Si_C^{hex}-C_{Si}^{cub}	5.34	5.09	4.92	4.65
Si_C^{hex}-C_{Si}^{hex}	5.23	5.01	4.80	4.54
Si_C^{cub}-C_{Si}^{cub}	2.71	2.48	2.30	2.03
Si_C^{cub}-C_{Si}^{hex}	2.87	2.67	2.45	2.19
Si_C^{hex}-C_{Si}^{cub}	2.46	2.23	2.43	1.87
Si_C^{hex}-C_{Si}^{hex}	2.67	2.40	2.65	2.07

Table 4.2: Formation- and binding energies of antisites and antisite pairs in 3C-SiC. All values in [eV].

Sites	128 cell, 2NN	128 cell, all	3C-216, 2NN	3C-216, all	Ref. [7]
C_{Si}	2.70	2.58	2.69	2.49	3.7
Si_C	4.47	4.25	4.42	4.06	4.6
Si_C -C_{Si}	4.93	4.72	4.85	4.59	5.8
Si_C -C_{Si}	2.24	2.11	2.26	1.96	2.5

is more than 1 eV lower in energy. In the binding energies, these deviations are lower. A reason for these deviations may also lie in the relaxation constraints in the ab initio calculation, since especially around the Si_C the lattice is strongly deformed, and the relaxation constraints in the SCC-DFTB calculations increases the formation energies by about 0.3 eV.

The similarity in the results lets us choose one polytype for further investigations: we chose 4H-SiC. The supercell was mainly the 240-atom cell, in particular for all calculations of diffusion mechanisms. Total energy calculations, especially for the larger aggregates were also performed in two larger supercells containing 384 or 480 atoms. Variations were found to be in the same range as for the values in Table 4.1. In the last sections of this chapter, for the discussion of larger onion-like aggregates, a cubic 3C-SiC supercell with 512 atoms was used, additionally.

4.1.2 Properties of the Antisite Pair

The antisite pair C$_{Si}$ Si$_{C}$ has C$_{3v}$ symmetry in
the cubic polytype and has only slight devia-
tions from this symmetry in the 4H- and 6H-
polytypes, resulting in C$_{1h}$ symmetry. The lat-
tice around the antisite pair is distorted similarly
as for the isolated antisites: The Si-Si-bonds at
the Si$_{C}$ are ≈15% (isolated Si$_{C}$: 12 %) elongated
compared to the ideal Si-C-bond length, the C-
C-bonds at the C$_{Si}$ are contracted by ≈12% (iso-
lated C$_{Si}$: 11 %). The Si-C-bond between
the two antisites is with ≈1% only slightly con-
tracted, thus relaxation results mainly in a shift
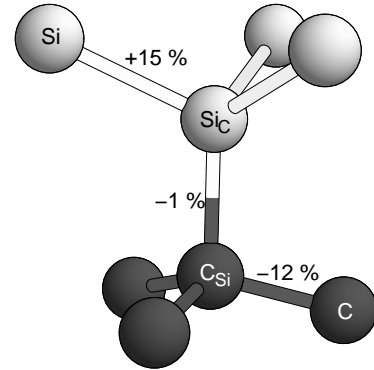of the complete pair along its axis, compare
Fig. 4.1.

Figure 4.1: Geometry of the antisite
pair C$_{Si}$ Si$_{C}$.

In order to calculate the internal energy and the entropy of formation of the antisite pair,
the vibrational spectra of the antisite pair and the ideal bulk have been calculated within
SCC-DFTB and AIMPRO, in a 64 atom supercell of 3C-SiC[1]. The antisites, its first and
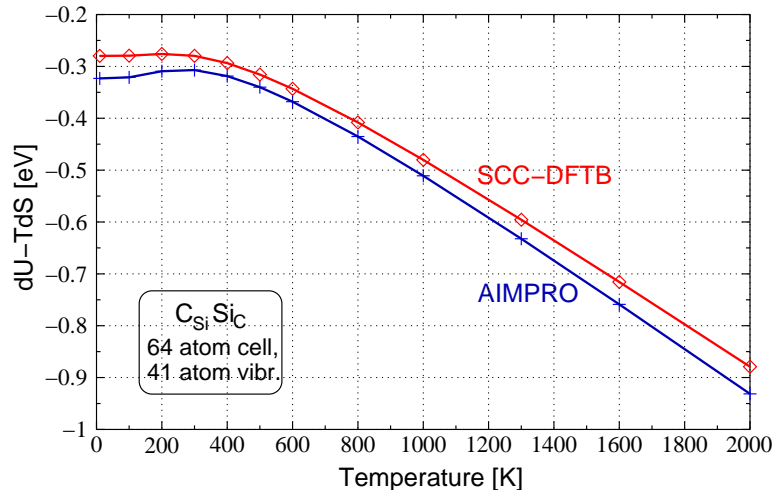

Figure 4.2: Using the vibrational spectrum calculated within SCC-DFTB and AIMPRO, the internal
energy and the entropy of formation have been calculated for the antisite pair in a 64 atom supercell of
3C-SiC. 41 atoms were allowed to vibrate.

second neighbors as well as the third neighbors of the silicon antisite were included in the
calculation of the vibrational spectrum. Including additionally the third neighbors of the
carbon antisite did not change the SCC-DFTB-result significantly[2]. The correction to the
total energy due to vibrations, $\Delta U - T \cdot \Delta S$, shows neither large deviations between the
two methods, see Fig. 4.2: for temperatures as high as T=2000 K, energy differences are
still less than 0.1 eV for an energy correction of ≈0.9 eV.
Taking a closer look at the vibrational spectra in Fig. 4.3, no significant dependence on
the supercell size (64 or 216 atoms) can be seen within the SCC-DFTB-calculations, but

---

[1]In SCC-DFTB, the same calculations were performed for a supercell containing 216 atoms, yielding
nearly exactly the same result.

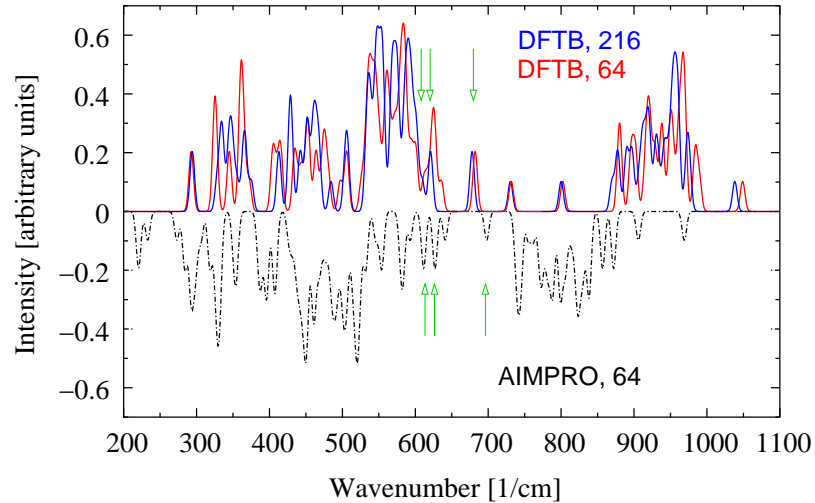[2]For AIMPRO this calculation was not available

Figure 4.3: *Positive y-axis:* Vibrational spectrum calculated within SCC-DFTB in a 64-atom (red line) and a 216-atom supercell (blue line). *Negative y-axis:* AIMPRO calculation in a 64-atom supercell. 41 atoms, that is two neighbor shells of the carbon antisite and three neighbor shells of the silicon antisite, were allowed to vibrate. The green arrows indicate the localized modes.

substantial differences between the SCC-DFTB- and the AIMPRO results.

Although the phonon band gap is as usual overestimated in the SCC-DFTB calculations[3] and the complete spectra look rather different in AIMPRO and SCC-DFTB (compare Fig. 4.3), a comparison of the localized modes in the phonon band gap shows a very good agreement between the two methods. Three localized modes are found in the phonon band gap: a degenerate e mode and an $a1$ mode are found at 626 cm^{-1} and 635 cm^{-1} induced by stretching vibrations of the three Si-Si-bonds next to the Si$_C$. The AIMPRO calculation yields 627 cm^{-1} and 641 cm^{-1} for these modes. At 682 cm^{-1} (AIMPRO 698 cm^{-1}) a C-C twisting mode is found, which is supposed to be forbidden for any PL transition[30].

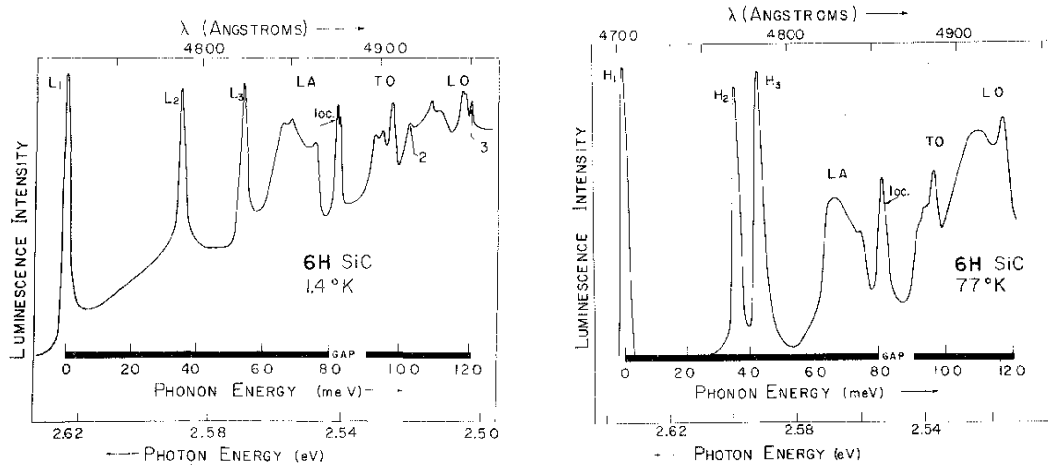Since the SCC-DFTB frequencies are much closer than the AIMPRO frequencies and,

Figure 4.4: Part of the D$_I$ photoluminescence spectrum as measured in 1972 at two different temperatures after annealing of an ion-bombarded sample at 1300°C [28]. The localized mode is marked with an arrow.

with the same broadening, consequently overlap much stronger than these, the localization

---
[3]Compare the discussion in Chapter 2

can not be read out of the plotted spectrum as easily as in the AIMPRO spectrum. The arrows in the diagram in Fig. 4.3 indicate the unbroadened frequency values, for which the localization has been calculated by investigating the eigenvectors belonging to the respective modes.

The calculated localized modes suggest an identification of the antisite pair with the very common D_I-center, for which recent photo-luminescence measurements report two lines at 661.3 cm^{-1} and 668.7 cm^{-1} for 3C-SiC, which can be correlated with the calculated e- and $a1$-modes. Probably the first photoluminescence spectra of the D_I-center were already measured by Choyke et al. in 1972 [28]. The localized vibrational mode can also be seen in Fig. 4.4 which shows the spectra for two temperatures. Experimental and theoretical details about this possible assignment can be found in Ref. [30].

Besides the possible technological relevance of the antisite pair, the comparison of the vibrational spectra of the antisite pair has shown that localized modes and integrated quantities like the vibrational entropy do not show significant deviations from the results obtained with ab initio methods, although the total spectra look rather different. Variations between these calculated values are in any case smaller than the variations that have to be considered for a comparison with experimental data and should therefore not be rated too high.

But how and under which conditions can such an antisite pair be created? In the following three sections all conceivable mechanisms are systematically investigated, starting with exchange processes in the perfect lattice, and eventually considering vacancy assisted mechanisms. An extension of the mechanisms to larger aggregates and an examination of the influence of the vibrational entropy close the chapter.

4.1.3 Creation of the $C_{Si} Si_C$ Pair in the perfect SiC-lattice

In the perfect lattice an antisite pair can only be created by the exchange of a Si and a C atom in a rotational movement of a Si-C pair. A simple rotation of a Si-C pair in a $(11\bar{2}0)$ plane of the crystal is energetically very costly ($\approx$12 eV). The energetically most favorable mechanism we found is a concerted exchange mechanism as proposed by Pandey for selfinterstitials in silicon [90].

The Pandey process consists of a simultaneous movement of the pair with a gradual change of the rotational plane by 60°. Rotation starts in a $(11\bar{2}0)$ plane, then the rotation plane gradually changes. After its rotation by 30°, the saddle point geometry is passed (here the axis of the pair is in a $(10\bar{1}0)$ plane). Finally, after another 30° rotation of the rotation plane the rotation of the pair is finished in the next $(11\bar{2}0)$ plane (60° to the first plane). The movement of the atoms is marked with arrows in Fig. 4.5, the respective minimal energy path is shown in Fig. 4.6. The reaction coordinate r has been constructed by calculating the projection of the actual
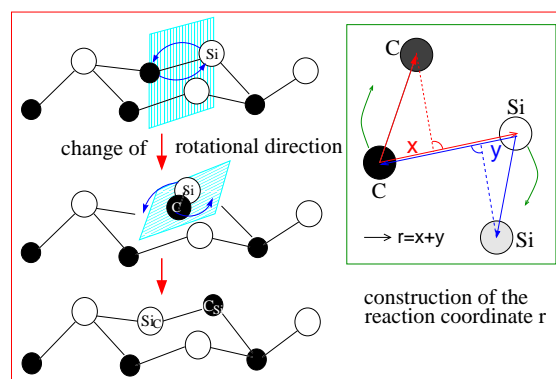

Figure 4.5: Geometry and movement of the atoms that create the antisite pair. In the inlet, the construction of the reaction coordinate r is shown (see text for details).

positions of the diffusing C– and Si–atoms separately onto the connecting vectors from

their initial to final positions. In the inset in Fig. 4.5 these two projections are marked with x for the C-atom and y for the Si-atom. The reaction coordinate is then obtained by summing up these two contributions $r = x + y$ for each geometry during the diffusion process.

At the saddle point geometry the distance between the moving C and Si atoms reaches its minimum length with a contraction of 11% compared to the ideal bulk bond length, see Fig. 4.6. The energy barrier between the ideal bulk and the Si_C-C_{Si} defect for this concerted exchange mechanism has been calculated to be 10.5 eV, i.e. ≈ 1 eV lower than the barrier for the two atoms rotating in a $(11\bar{2}0)$ plane. However, this value of 10.5 eV is still very high, indicating that direct antisite pair formation is unlikely to happen in a perfect lattice.
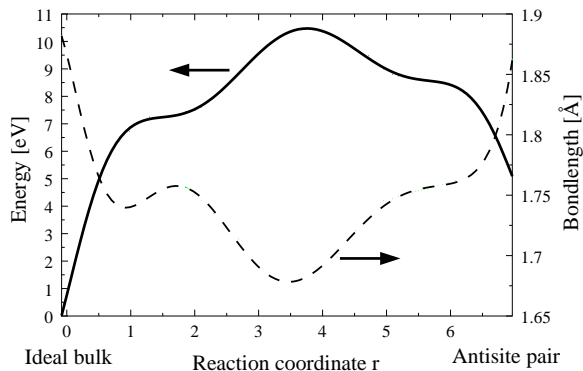

Figure 4.6: Energy difference between the actual geometry and the ideal crystal is shown during the process (*left ordinate*); on the *right ordinate* the bondlength of the rotating Si-C pair is shown.

4.1.4   Migration of Antisites in the ideal lattice

If isolated carbon- and silicon-antisites are present in the lattice, as can be expected due to the recombination processes discussed in the previous chapter, pair formation might happen by aggregation.

One of the antisites or both of them have to migrate through the lattice until they meet. Assuming no other defects around, such a process is, again based on exchange processes, but not with the direct neighbor as in the direct mechanism described before, but instead with a second neighbor. These sublattice migration processes of Si_C and C_{Si} have been investigated, but turn out to be energetically very costly: C_{Si} migration can be activated with 11.7 eV, for Si_C migration 11.6 eV are needed. The energies are even higher than for the Pandey process, so that these mechanisms have to be ruled out, as well.

Consequently, the formation of antisites requires some support from other defects — the most promising candidates are vacancies: The presence of silicon- and carbon–vacancies in the material can facilitate the migration of other defects, since they can help to keep the lattice distortion small in a migration process. This holds also for the creation of antisite pairs [40]. Furthermore, their existence in a sufficient concentration is certain under the assumed conditions.

4.1.5   Pair creation by vacancy migration

An exchange of a Si-C pair close to a vacancy requires considerably less energy than in the perfect lattice. However, a vacancy can also help the formation of an antisite pair by avoiding any costly exchange of atoms. For both vacancies, the activation energies of such mechanisms have been found to be by $1-2$ eV lower than for the respective exchange
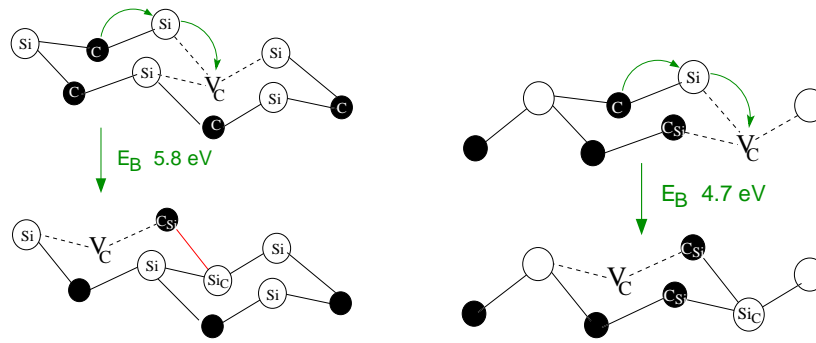
Figure 4.7: Antisite pair formation next to V_C (*left*) and V_C -C_{Si} (*right*).

process.

The mechanism is as follows: Suppose we have a single carbon vacancy. Instead of exchanging its site with a neighboring carbon atom, one of the silicon ligands can as well move into the vacancy, forming a silicon antisite. One of its carbon neighbors can take the silicon site by following immediately. This mechanism is illustrated in the left part of Fig. 4.7.

With the carbon vacancy having moved one site further on the carbon sublattice, an antisite pair has thus been created. This process can be activated with an energy of 5.8 eV, which is a large reduction compared to the direct exchange process in the perfect lattice. In the "2+" charge state, activation needs 6.4 eV, in "2-" the activation energy is reduced to 4.6 eV, confirming the trend to lower activation energies for higher negatively charged structures as already discussed in Chapter 3.
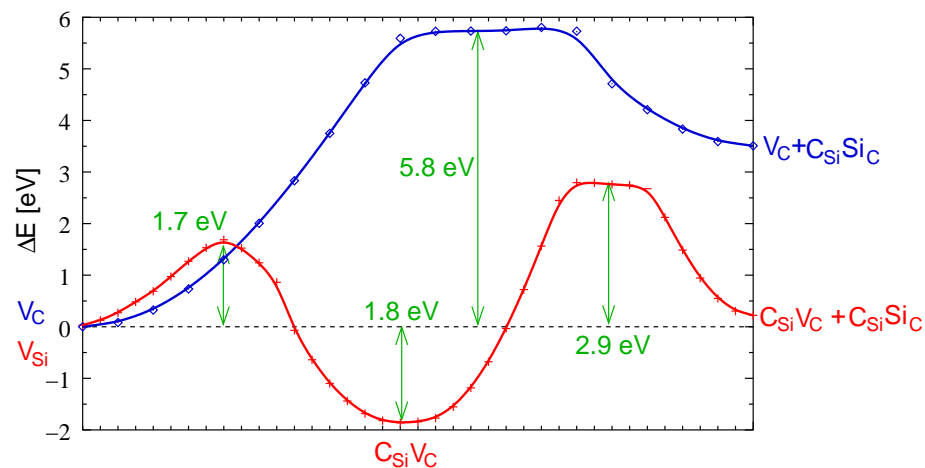

Figure 4.8: Energy change during the vacancy migration process starting from either V_C (blue curve) or V_{Si} (red curve). For better comparison, the energy of the initial structures has been chosen as reference energy for each of the energy curves. In case of V_{Si}, the mechanism consists of two steps: the formation of $V_C C_{Si}$, followed by the $C_{Si} Si_C$ creation by the migration of V_C.

Starting with a silicon vacancy V_{Si}, instead, the first thing to happen is the formation of a V_C -C_{Si} pair as described in Chapter 3. This process requires only about 1.7 eV activation energy and leads to an energy gain of 1.8 eV compared to the silicon vacancy. In a next step, an antisite pair can be created by migration of V_C as described above, see the right part of Fig. 4.7. The activation energy for this process is only 4.7 eV and the formation energy of the antisite–pair from V_C -C_{Si} is only $\approx$2.0 eV [40]. The analogous process to

the V_C migration, i. e. a carbon atom moving into the silicon vacancy and the next silicon atom following, is not possible, since the resulting structure of this process, an antisite pair next to a silicon vacancy $C_{Si} Si_C$ -V_{Si} is not stable, compare Section 3.1.3. The silicon antisite immediately recombines with the silicon vacancy.

The change in energy during the migration process is plotted in the diagram in Fig. 4.8 for both vacancies. For better comparison, both energy curves have been plotted with the energy of their respective initial structures as reference. The red curve denoting the mechanism which starts from a silicon vacancy shows two barriers and a minimum in between. For a fast process, no energy might dissipate in between, so that the overall barrier that has to be overcome in order to create the $C_{Si} V_C$ +$C_{Si} Si_C$ complex is determined by the highest of the two barriers, namely 2.9 eV. If the $C_{Si} V_C$ pair already exists or the energy can for other reasons dissipate at this step, the barrier of 4.7 eV determines the process.

In any case, assuming only the presence of vacancies in the crystal, this mechanism, which includes a movement of a carbon vacancy, is the most favorable for the creation of antisite pairs[4].

4.2   Larger Aggregates of Antisites

With an activation energy not much higher than that calculated for the sublattice migration of vacancies, the creation of an antisite pair becomes imaginable as a high temperature process. There is – at first sight – no reason, why aggregation of antisites should stop with the formation of pairs, making the investigation of larger aggregates interesting.
The first question is, which geometrical arrangements are stable, which of them are most favorable, then the question for their mechanism of creation has to be answered.

4.2.1   Stability of various arrangements

We start with an investigation of stoichiometrically built up structures which can be imagined to be aggregates of pairs of antisites. For such aggregates consisting of n antisite pairs, we have investigated the most stable geometry. We distinguish three principally different arrangements according to their dimensions. First, antisite pairs can be stacked upon each other, forming a one-dimensional chain of antisites. Second, the antisite pairs can be arranged in a plane, e. g. parallel to the polar direction of the crystal, resulting in a two-dimensional planar defect. Finally, three-dimensional aggregates can be formed.
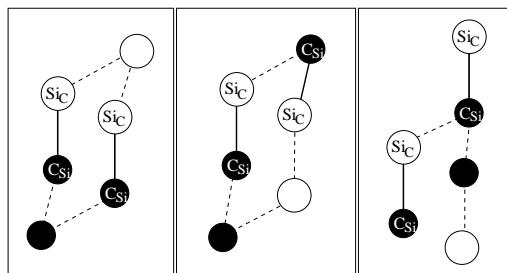

Figure 4.9: Several orientations of two antisite pairs: they can be oriented parallel to each other (*Left:*), ring-like, as shown in the middle, or stacked upon each other (*right*).

---

[4]In Section 4.4, another vacancy assisted mechanism for the mobility of isolated antisites will be discussed. Here, a discussion of larger aggregates of antisites seems, though, to make more sense, since an extension of the mechanism described in this section to the formation of larger aggregates suggests itself.
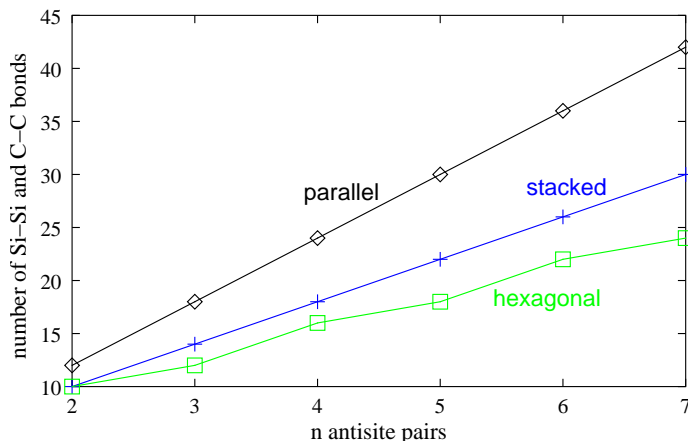
Figure 4.10: Number of "wrong" bonds in the aggregate of n antisite pairs.

The various possible orientations of two antisite pairs towards each other are shown in Fig. 4.9. They can be arranged parallel as shown in the left part of Fig. 4.9, ring-like (center part of Fig. 4.9) or stacked upon each other along a crystal direction (right part). This distinction can be maintained for larger aggregates of more than two pairs, as well, leading to the classification of one-, two- or three-dimensional aggregates[5].

The number of "non-SiC-bonds", i. e. the number of (compared to the Si-C-bonds) short C-C-bonds and long Si-Si-bonds induced by the antisites is a good quantity to compare the different geometries. The resulting distortion is a measure for the formation energy and, thus, for the stability of the structure. For two pairs, as shown in Fig. 4.9, six Si-Si- and six C-C-bonds can be counted in the parallel arrangement, while only five of each non-SiC bond are found in the two other structures. A comparison for aggregates of n antisite pairs was done in Fig. 4.10, showing the number of non-SiC-bonds that a structure in each of the three cases must have at least.

In the parallel arrangement this number grows fastest with the number n of antisite pairs. While there is no difference for two antisite pairs, the ring-like ("hexagonal") arrangement has the smallest number of non-SiC-bonds for three and more pairs. With three, five,...antisite pairs, a whole ring can be completed, leading to an especially small number of non-SiC-bonds in this arrangement.

The energetical behavior turns, in fact, out to be analogous, showing that the parallel arrangement is highest in energy, and even becomes instable for large n. This can be understood, since the strong expansion on the side of the silicon antisites and the strong contrac-

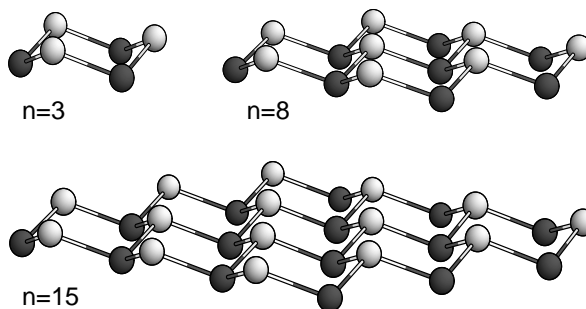**Figure 4.11:** Geometries of the most stable two-dimensional aggregates of antisites. Structures were calculated in two different supercells, one of which was more extended in the lateral direction (384 atom supercell), the other more in the polar direction (480 atoms). The differences are found to be negligible.

---

[5]Non-stoichiometrical three-dimensional aggregates will be discussed later on

tion on the side of the carbon antisites can be balanced in no way. For the other two arrangements, the energy

$$\Delta E(n) = \frac{E(n\,pairs) - nE(1\,pair)}{n} \qquad (4.1)$$

is gained by bringing n pairs together, see Fig. 4.12. The limiting cases are an infinite chain, as shown here along the [0001] axis, in the one-dimensional case, and a completely inverted bilayer in the two-dimensional case, see Fig. 4.13. In the latter, the bonds inside the bilayer have the ideal Si-C bond length, and the longer Si-Si-bonds on one side are compensated by the shorter C-C-bonds on the other side, causing only a small shift of the complete bilayer along the [0001] direction.
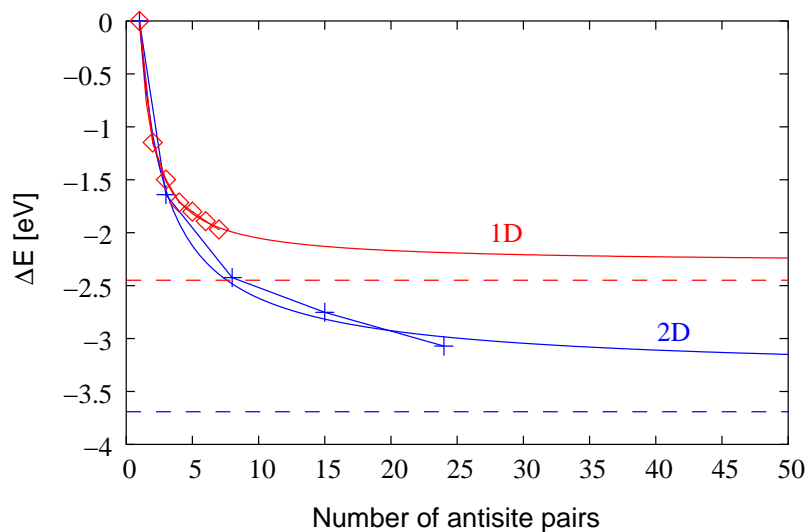

Figure 4.12: One-dimensional (1D) and two-dimensional (2D) aggregates of antisites. The 1D structures up to the infinite chain were calculated in a 480-atom supercell, while for the 2D structures the more laterally extended 384-atom supercell was used, in order to be able to calculate some larger complexes. The dashed lines indicate the limits of the infinite chain (1D) and the completely inverted bilayer (2D).

The energy gain $\Delta E(n)$ upon adding pairs of antisites to the aggregate, converges like $1/n$ to the limit of $\Delta E_{1D}(\infty)$ =-2.5 eV/pair (infinite chain) and $\Delta E_{2D}(\infty)$ =-3.6 eV/pair (complete antisite layer), respectively.

Thus, especially the two-dimensional aggregation, where the main stabilizing factor is the formation of "inverted rings", is energetically favorable, and mechanisms for the creation of such aggregates should, therefore, be investigated.

For three-dimensional aggregates of antisites, we find the symmetrically, but non-stoichiometrically, built up "onion-like" structures to be the most stable arrangements. Created upon the alternating addition of single antisites of both types, these structures are centered on one antisite and surrounded by one or more shells of antisites of alternating type. The smallest ones, $Si_C\,(C_{Si})_4$ and $C_{Si}\,(Si_C)_4$ have been found to be extremely stable: the energy gains due to clustering are as high as 7.1 eV and 7.8 eV compared to the isolated constituents. Substituting the next shell of atoms by antisites leads to complexes of the form $Si_C\,(C_{Si})_4(Si_C)_{12}$ and $C_{Si}\,(Si_C)_4(C_{Si})_{12}$. Here, the energy gain compared to isolated C_{Si} and Si_C antisites has been calculated in a 512 atom containing 3C-supercell to be 28.1 eV and 25.8 eV. In 4H-SiC, the formation energies of these structures might be slightly
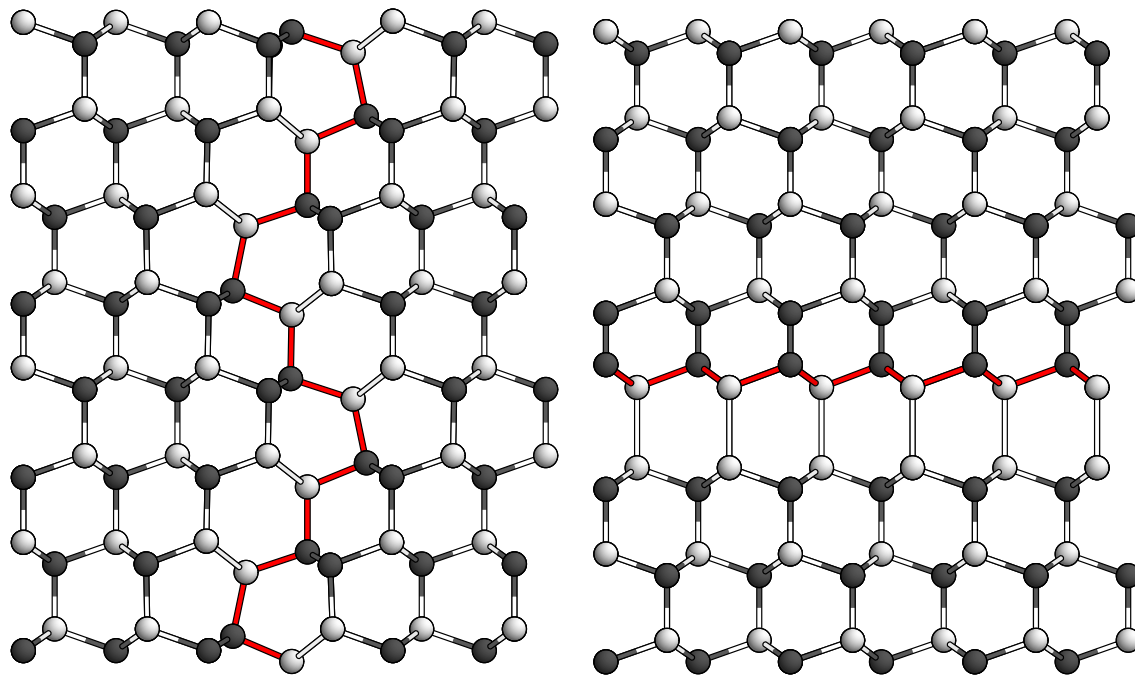
Figure 4.13: Geometries of the infinitely extended chain of antisites (*left*) and the completely inverted bilayer (*right*).

higher due to reduced symmetry.

A similar $1/r$ behavior of the energy gain, following the surface-to-volume ratio, can be expected upon this kind of 3D–aggregation of individual antisites into concentric "antiphase shells".

Now we turn to the question of how such large antisite aggregates can be created, starting with the two-dimensional aggregates.

4.2.2   A Vacancy's Spiral Walk for the Creation of Antisite Aggregates

In principle, it is conceivable to extend the vacancy migration mechanism that was described for the pair in Section 4.1.4 to the creation of further pairs of antisites [91]. As is indicated in Fig. 4.14, vacancy migration could go on along the dashed line by this mechanism. The result of a seven-steps "V_C-walk" is shown for example on the right hand side in Fig. 4.14. In principle, the whole bilayer could be inverted by this mechanism before it stops.

The whole process and the actual energy value of the structure is shown in Fig. 4.15, starting from an isolated carbon vacancy in the upper left picture and following the migration process until the lower left corner is reached. Below the geometries of the minimum energy structures, the part of the energy curve that has been passed by so far is shown. In each figure, the atoms that will become antisites in the following step are marked with light cyan circles, while already created antisites are marked with red circles. From the third pair on, the migration barriers are noticeably lower, which seems to be caused by the ring formation: In the fourth picture in Fig. 4.15, the first ring of antisites is complete, and every second step one more ring of antisites is added. These ring structures are energetically very favorable, since they allow a very good balancing of different bondlengths — in
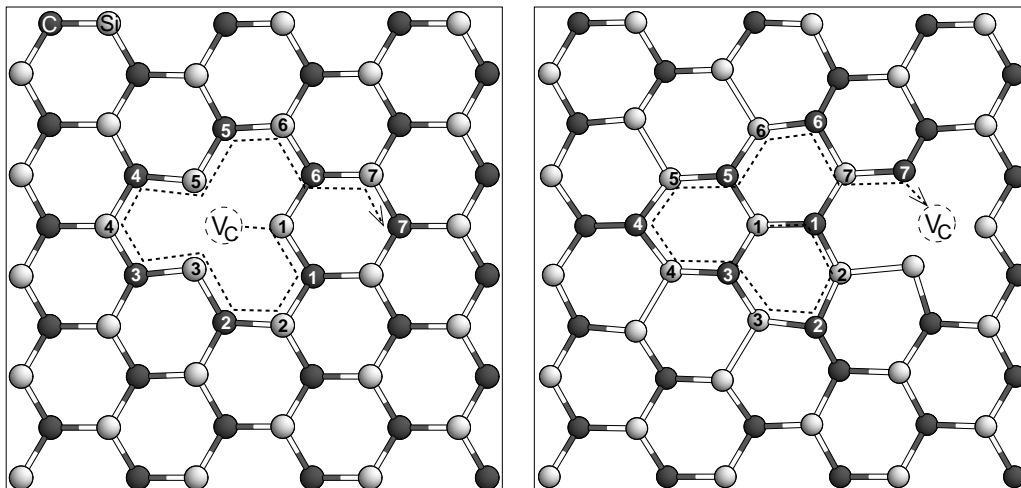
Figure 4.14: Top view of a (0001) plane, creation of antisite pairs by migration of vacancies. *Left:* In the first step, the atoms labelled with 1 are supposed to move along the dashed line towards V_C. After this step, the vacancy will be at the site of carbon atom 1. In principle, the mechanism can go on, as is denoted with the dashed line, while perpetually pairs of antisites are created. *Right:* After seven steps, the result looks like this: V_C has moved along the dashed line up to the former site of carbon atom 7. In contrast to the antisites on the edges of the resulting platelet, those antisites created first are now coordinated as in the ideal lattice, except for the bond perpendicular to the plane shown here.

the rings, there are only Si–C bonds, while the distortion due to longer Si–Si- or shorter C–C–bonds is restricted to the direction of the c-axis.

In the last two steps of this mechanism, the effect of the barrier lowering might be superposed by the supercell constraints in the plane, caused by the periodic images of the defect, which are in case of the large antisite aggregates already very close to each other.

Of course, there are not only carbon vacancies present, but also silicon vacancies and divacancies. If starting from a silicon vacancy, instead, the mechanism is nearly the same. The only difference is the first step, where the transformation to the $V_C\,C_{Si}$ pair happens before the carbon vacancy can follow the afore described procedure. The creation of the $V_C\,C_{Si}$ pair in the plane, where the spiral walk will take place one step later, is found to be slightly more opportune for the activation energies of the following steps than the creation of a pair perpendicular to this plane.

Slightly different looks the process if starting with a divacancy $V_C\,V_{Si}$. Although the mechanism shown in Fig. 4.16, of a moving carbon vacancy is the same in this case as in case of an isolated V_C, ring formation does not occur during the first six steps. The mechanism starts with the transformation of $V_C\,V_{Si}$ to a $V_C\,C_{Si}\,V_C$ complex (which requires ≈ 2 eV to be activated), then one of the V_C performs the spiral walk centered around the other V_C (which in a larger aggregate has three C-ligands and is thus rather a V_{Si}). Not before the seventh step, a ring-like structure has been created. However, the surrounded vacancy seems to facilitate the migration process, resulting in distinctively lower migration barriers compared to the mechanisms starting from isolated vacancies.

All the three processes described so far have one thing in common. Regarding again the energy curve in Fig. 4.15, the problem of the recombination barriers becomes obvious. If

Figure 4.15: Top view of a (0001) plane: stepwise creation of up to seven antisite pairs by migration of a carbon vacancy. Below the geometries of the minimum energy structures, the part of the energy curve that has been passed by so far is shown. In each figure, the atoms that will become antisites in the following step are marked with light cyan circles, while already created antisites are marked with red circles. The energy barriers are denoted above the arrows.

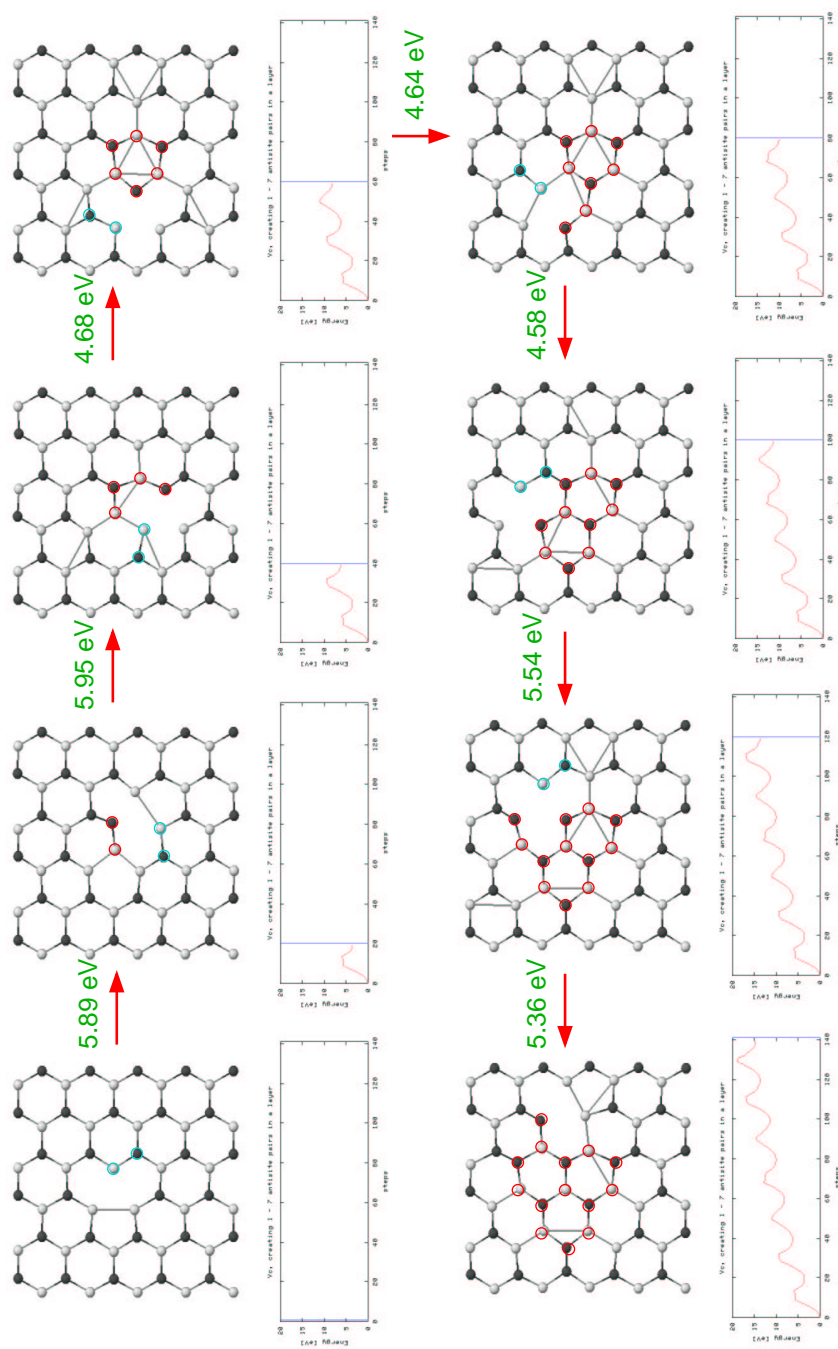**Figure 4.16:** Top view of a (0001) plane: stepwise creation of antisite pairs by migration of a carbon vacancy, but the origin is a divacancy V_C V_{Si} in this case. Again, the atoms that will become antisites in the following step are marked with light cyan circles, while already created antisites are marked with red circles. The energy barriers are denoted above the arrows.
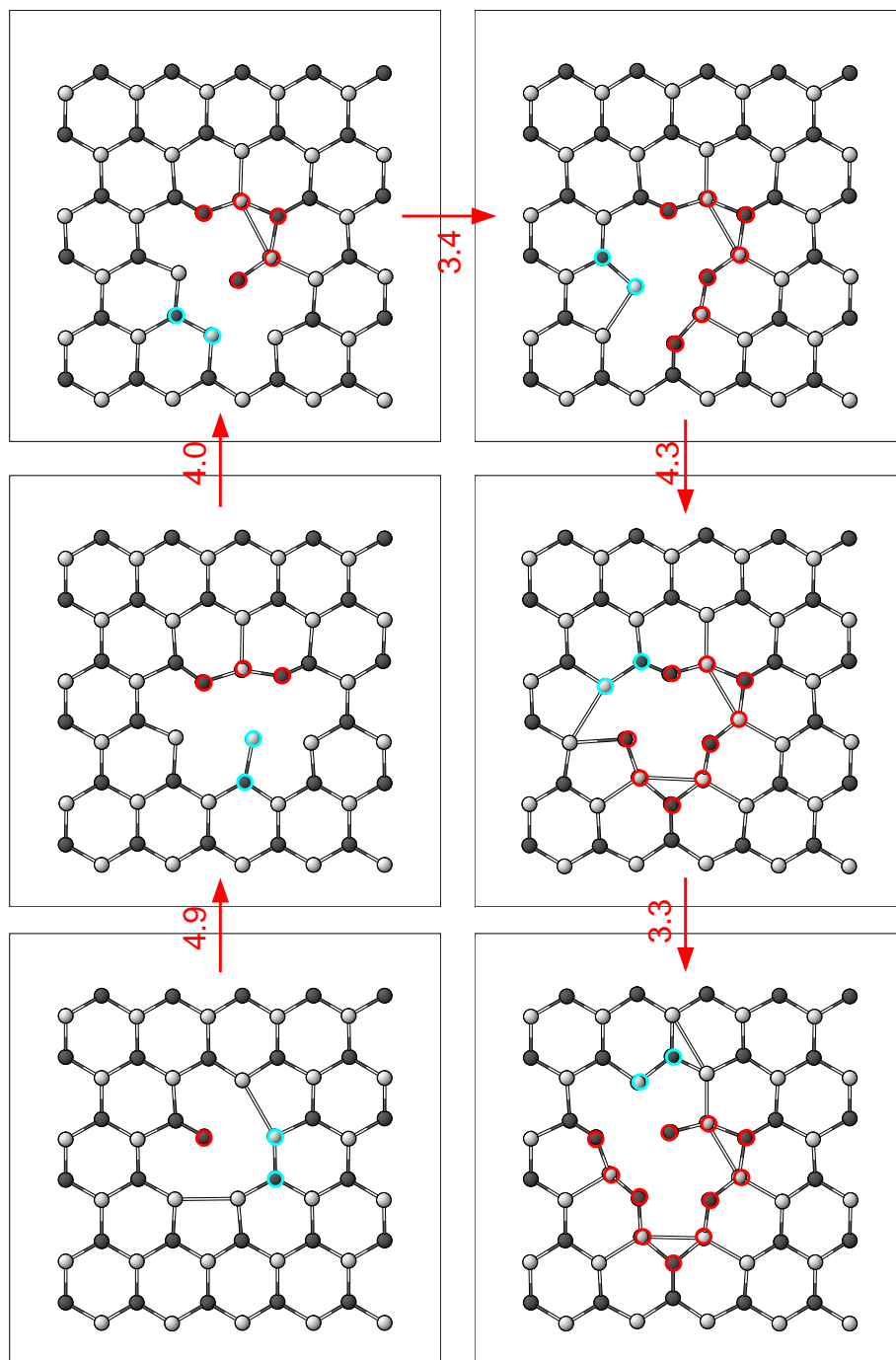
the energy suffices to overcome the barrier in the direction of creation of antisite pairs, it is certainly enough to overcome the barrier in the reverse direction which, in addition, leads to a lower energy structure.

If starting with a silicon vacancy, the V_C C_{Si} pair is energetically favorable to be created, and so is the first antisite pair. However, already for the second pair, the formation energy is by ≈ 3 eV higher than that of V_{Si}. Consequently, as shown in Fig. 4.20 (solid black line), the energy barrier for recombination is distinctively lower than the barrier that has to be overcome for the creation of the second pair, which requires about 6 eV, i. e. is much too high. Furthermore, the recombination barriers are lower than the energy barriers calculated for sublattice migration of V_{Si} or V_C. Thus, the dissociation of the vacancies after some steps, which would leave a stable antisite platelet behind, does not seem likely.

4.3   Contributions of the Vibrational Entropy

During the migration process, the lattice has to be rearranged quite strongly, with four Si-C–bonds being broken and two Si-Si- and two C-C–bonds coming up. Hence, the description of the energies by the total energies of the structures might be too inaccurate. Thus, it might be necessary to consider the contributions from vibrational entropy. As discussed in Section 2.7, their influence may in some cases not be negligible, especially for processes involving substantial rearrangements of the lattice, which can give rise to considerable changes in the vibrational frequencies.

Although such a correction cannot be expected to further stabilize the larger aggregates essentially, it might have a considerable influence on the barriers for the above described processes on the one hand and for vacancy migration on the sublattice on the other hand, making the dissociation of the vacancy more probable.

Furthermore, it can certainly not be expected that the entropical contributions lower the activation energy needed for the pair creation by an exchange process in the ideal lattice (≈ 10 eV) sufficiently, so that the process could be expected to happen at usual temperatures[6].

Figure 4.17: Lowering of the sublattice migration barrier of V_C: the change in $dU - T \cdot dS$ at the saddle point geometry of the process compared to the minimum energy structure.

The migration of vacancies on their sublattices and the vacancy assisted processes for antisite creation, however, have to be re-investigated in this context.

---

[6]For a better readability, the difference between the energy barriers (calculated without consideration of the entropical contribution) and the free energy barriers (including this term) is referred to as "lowering of the barrier", although this is, of course, not a "lowering" in the physical sense.

Example 1: Sublattice migration of vacancies

Considering the vibrational contributions $dU - T \cdot dS$, the activation energies for the sublattice migration of V_C and V_{Si} are lowered very similarly like shown in Fig. 4.17 for the carbon vacancy. Including all atoms of the supercell yields the black line, restricting the vibrations of nearest and next nearest neighbors results in the blue curve. At a typical annealing temperature of T=1800 K, the activation energy for the sublattice migration of V_C is lowered by $\Delta E \approx 0.3$ eV. The same holds for V_{Si}. No qualitative changes result from including the entropy in this case. The diagram in Fig. 4.18 shows how the energy curve changes at this temperature (all atoms relaxed). Even at temperatures as high as 2000 K, the difference between the results with and without this constraint is only 0.05 eV (compare Fig. 4.17), i. e. clearly less than the accuracy of the method.
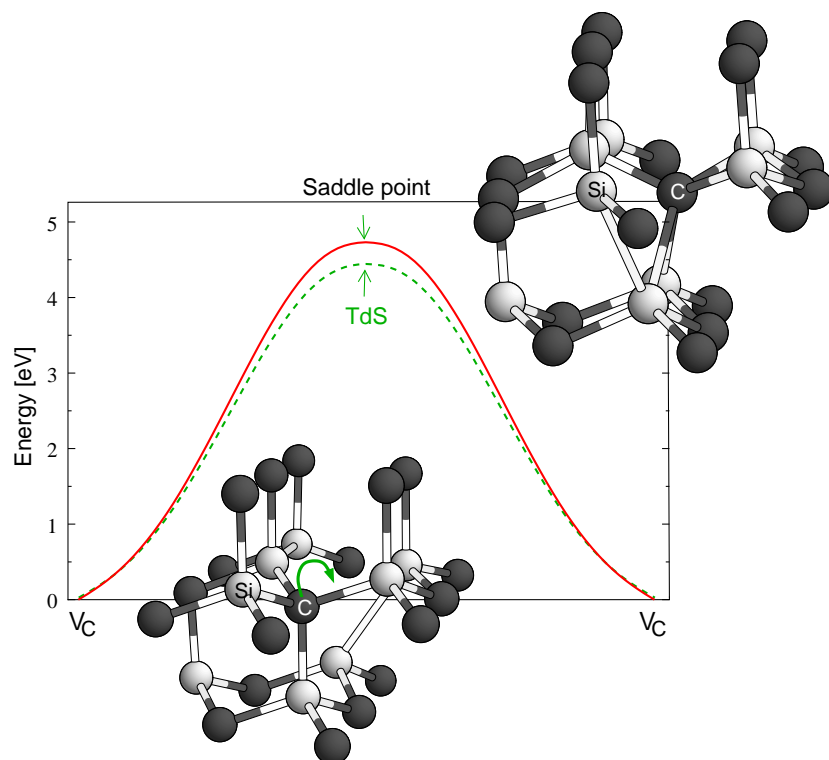
Figure 4.18: Influence of the vibrational entropy on the activation energy for the sublattice migration of the carbon vacancy.

Example 2: Transformation of V_{Si} to the $V_C\,C_{Si}$ pair

The transformation of the silicon vacancy into the $V_C\,C_{Si}$ pair defect (compare Section 3.1.3) is affected similarly by the entropy contributions: At a temperature of T=1800 K, the activation energy (compared to the silicon vacancy as reference) is lowered by $\Delta U - T \cdot \Delta S \approx 0.3$ eV. The resulting pair defect, $V_C\,C_{Si}$, is lowered by approximately the same amount compared to the silicon vacancy. Consequently, the recombination barrier remains unchanged, and the $V_C\,C_{Si}$ pair is further stabilized against recombination to V_{Si}. The free energy barrier for the process $V_{Si} \longrightarrow V_C\text{-}C_{Si}$ is, then, 1.4 eV, the pair $V_C\text{-}C_{Si}$ is by 2.1 eV lower in energy than the silicon vacancy.
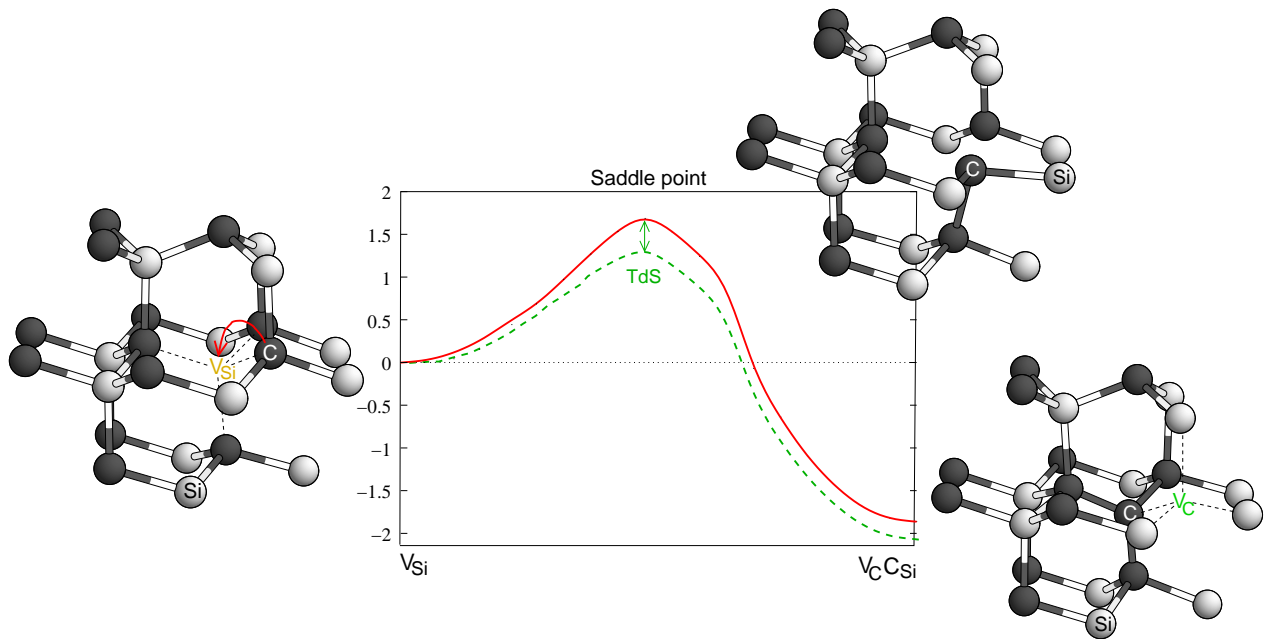
Figure 4.19: Influence of the vibrational entropy on the transformation of the silicon vacancy into the $V_C C_{Si}$ pair.

Now, reconsidering the "spiral walk" of the vacancy, i. e. the creation of pairs of antisites along the way around the original vacancy site (see Section 4.2), we can calculate the entropical contributions to all the equilibrium and saddle point structures. Because of the stronger rearrangement of the lattice, these contributions can be expected to be larger than those of the first two examples.

Example 3: The spiral walk

The first step, the transformation of V_{Si}, has just been discussed in example 2. The activation energy for the next step of the process, that means the creation of the first antisite pair V_C -C_{Si} $\longrightarrow$ (V_C -C_{Si}) + (C_{Si} -Si_C), is lowered to 3.7 eV. The final structure of this step is then found to be $\approx$ 0.3 eV more stable than the silicon vacancy. The result is shown in Fig. 4.20. For two different temperatures, T=1000 K (blue lines) and T=2000 K (red lines), the Gibbs free energies of minima and saddle point structures are shown in the diagram together with the energies obtained without considering these terms (black lines)[7]. Saddle point geometries are throughout slightly stronger affected than equilibrium structures, and the energy differences are as expected larger than those found for the sublattice migration of vacancies. Nevertheless, no qualitative changes concerning the energetical order of activation- and recombination barriers show up here, so that the inclusion of entropy cannot change the conclusion that this mechanism will not lead to larger aggregates of antisites but probably stop after the creation of (V_C -C_{Si})+(C_{Si} -Si_C), which, besides, has a slightly lower free energy than the isolated silicon vacancy at temperatures above 1000 K.

At this point, it should be noted that a really substantial change in the results of this section, i. e. a strong stabilization of the larger antisite aggregates, would mean that a
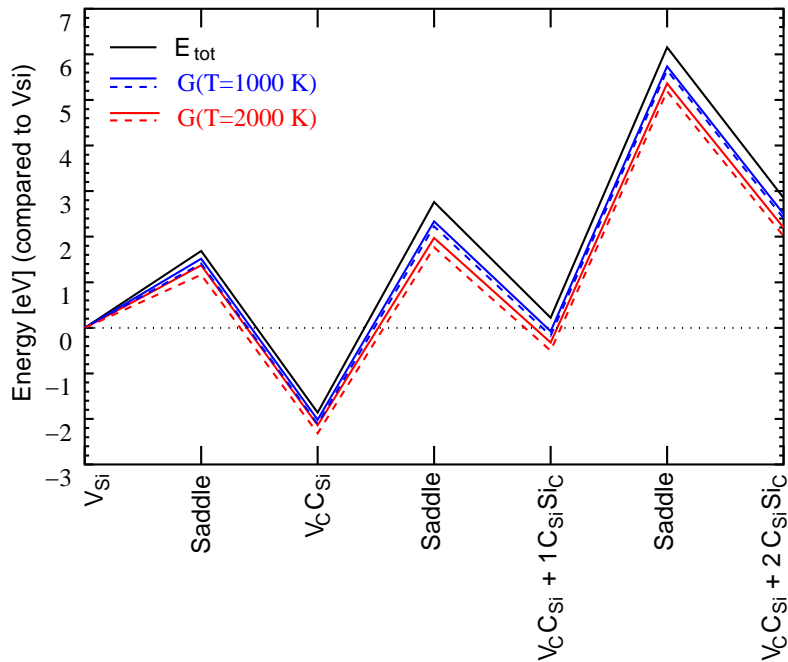
---

[7]The connecting lines are just guides for the eye

Figure 4.20: Influence of the entropy on the pair creation mechanism. For two temperatures, T=1000 K and T=2000 K, the Gibbs free energy has been calculated for the equilibrium structures and the saddle point geometries. *Solid line:* One (0001)-face of the supercell was kept fixed. *Dashed line:* all atoms included in the vibrational spectrum

spontaneous inversion of the crystal lattice already during growth (which happens at sufficiently high temperatures to activate the processes) became possible. A mechanism to create larger aggregates of antisites has, therefore, to be more demanding, that means it has to be dependent on preconditions that are not fulfilled during usual growth processes. In order to find such a possibility, an alternative mechanism based on single antisite movements is discussed in the next section.

4.4   Mobility of Isolated Antisites

We have seen in Chapter 3 that the recombination of interstitials with nearby vacancies is among the first processes to happen during the annealing phase. Since this recombination also leads to antisites, this suggests an aggregation mechanism of isolated antisites to antisite pairs (or larger aggregates). However, we have seen in Section 4.1.3 that activation energies for sublattice migration of antisites are much too high to be imaginable at realistic temperatures. The "spiral walk" of vacancies, compare Section 4.2.2, may be able to explain pair formation, but not the formation of larger aggregates, thus vacancies alone could neither help in this case.

The high vacancy concentrations may, however, assist the migration processes of isolated antisites. The following sections deal with the role of vacancies in migration processes of antisites.

4.4.1 The vacancy assisted mechanism

To activate a vacancy assisted mechanism for antisite migration, the vacancies must first approach the antisites. Thus, sublattice migration of vacancies is essential in any case. When a vacancy has reached a neighboring site to an antisite on either of the two sublattices, an antisite migration mechanism can start. A silicon antisite Si_C can jump directly into a neighboring carbon vacancy V_C. With an energy of 4.1 eV the jump can be activated. ΔS is nearly zero for this jump, thus there is no lowering of the barrier due to vibrations.
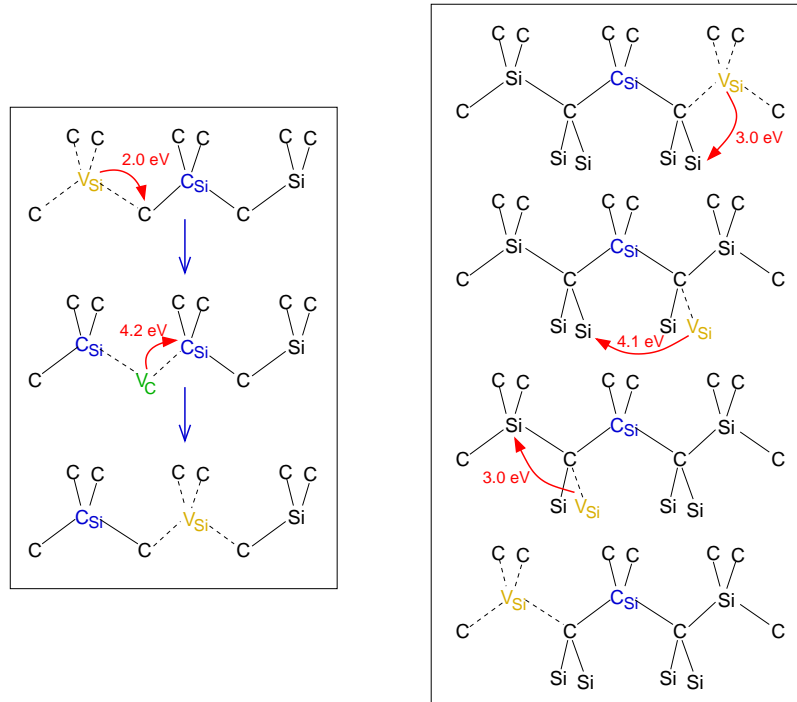

Figure 4.21: *Left:* Two-step mechanism of a Si-vacancy assisted jump of the carbon antisite. The first step requires 2.0 eV, the second 4.2 eV to be activated, but the intermediate structure V_C-C_{Si}-V_C is 2.2 eV lower in energy than the initial structure V_{Si}-C_{Si}. *Right:* Instead of dissociating, V_{Si} can as well migrate around C_{Si}. The determining step is shown in the second picture, where V_{Si} has to move from one C-ligand of C_{Si} to the other. The migration barrier of this step has nearly the value as for usual sublattice migration of V_{Si}, whereas the other two steps are less costly.

The carbon antisite C_{Si} can perform a similar jump into a silicon vacancy V_{Si}, requiring 4.9 eV activation energy. In this case, however, a two-step mechanism, as shown in Fig. 4.21, is found to be much more favorable. The first step is a transformation of the silicon vacancy to the $V_C C_{Si}$–complex, lowering the energy of the structure by about 2.2 eV (compare the top and the middle structure in Fig. 4.21 and the energy curve in Fig. 4.22). The activation energy for this transformation is only 2.0 eV. From this symmetric structure, the first C_{Si} can recombine with the V_C to complete the jump (middle and bottom structure in Fig. 4.21). Assuming no energy dissipation at the intermediate stage, the overall energy barrier which is important for the mechanism is 2.0 eV. Considering the entropical contributions does even in this case not lead to a significant lowering of the barrier (for T<2000K $\Delta U - T \cdot \Delta S$ is less than 0.1 eV).
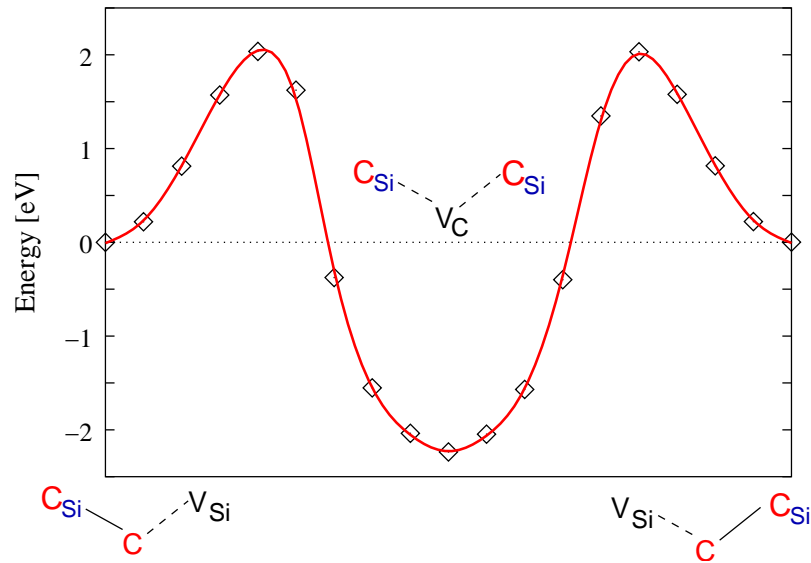
Figure 4.22: In the two-step mechanism of the vacancy assisted C_{Si} -migration an intermediate structure with a lower energy than the initial and the final structure is crossed.

Up to now, only an *exchange* of a vacancy and an antisite has happened. To obtain a *directed diffusion* process, we need the vacancy to either dissociate from the antisite — then the antisite has to wait for the arrival of another vacancy — or to move around the antisite, such that a further antisite jump can take place.

This latter mechanism is shown in the right part of Fig. 4.21 for the silicon vacancy moving around the carbon antisite. It consists of three steps, whereof two are energetically equivalent. First, the vacancy has to move to one of the other Si-sites surrounding the C-ligand of the C_{Si} ($E_{activ} = 3.0$ eV). In the second step, migration has to continue to a Si-site next to the other ligand of the C_{Si}, which is a principally different process ($E_{activ} = 4.1$ eV). The third step is equivalent to the first one ($E_{activ} = 3.0$ eV), but in the resulting structure V_{Si} and C_{Si} have changed places – compare the top and bottom parts of Fig. 4.21.

The determining step is shown in the second picture, where V_{Si} has to move from one C-ligand of the carbon antisite to the other. The migration barrier of this step ($E_{activ} = 4.1$ eV) has approximately the same value as that of usual sublattice migration of V_{Si} (if no antisite is present), whereas the other two steps are less costly in energy. This can be understood considering the strong inward relaxation of the C-ligands around a C_{Si}, which destabilizes the bonds between the first and the second neighbors and thereby lowers the energy that is necessary for moving the Si-atom to the vacant site. The entropical contribution lowers the activation energy of the determining step again by about 0.2 eV at T=1800 K.

The dissociation of the carbon vacancy from the silicon antisite can be activated with 4.8 eV. Considering the entropy, a free activation energy of only 4.4 eV is needed at T=1800 K. Note that these values are slightly above those found for the sublattice migration of V_C, thus determining the activation energy needed for the whole process.

Thus, vacancy assisted migration of both antisites is energetically comparable to plain sublattice migration of vacancies. This result makes it conceivable that pairs of antisites as well as possibly larger aggregates of antisites can be formed at conditions under which
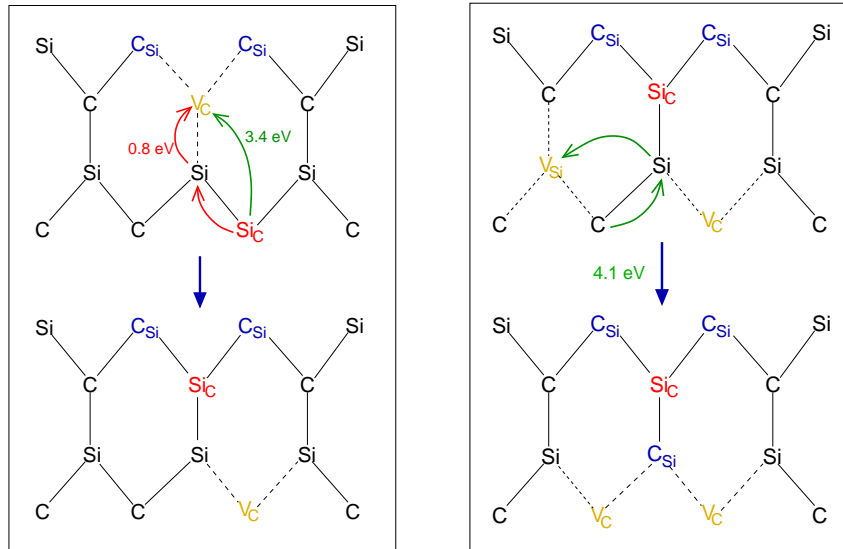
Figure 4.23: *Left:* The $Si_C (C_{Si})_2$ complex can be easily created from the $V_{Si} (C_{Si})_2$ complex that is an intermediate state during the vacancy assisted movement of C_{Si}. *Right:* If a silicon vacancy approaches the $Si_C (C_{Si})_2$ complex up to the position shown in the upper structure, a barrier of 4.1 eV has to be overcome to end up with a $Si_C (C_{Si})_3$ complex. The energy is thereby lowered by 3.18 eV.

vacancy migration is observed.

4.4.2 The $Si_C (C_{Si})_2$ complex

The two-step mechanism that has been discussed for the silicon vacancy assisted migration of a carbon antisite leads in the first step to a very stable structure, the $V_C (C_{Si})_2$ complex (see the center structure of the left part of Fig. 4.21).

We consider the case that a carbon antisite via the vacancy assisted mechanism proposed afore approaches a silicon antisite. If aggregation is supposed to happen this way, then the situation shown on the left hand side of Fig. 4.23 has to occur in the last step[8]. As indicated by the arrows in Fig. 4.23 (left), there are two possible movements of the silicon antisite. A direct recombination of the Si_C with V_C (green arrow) would require 3.4 eV, but the mechanism indicated with the red arrows, in which the Si_C pushes its silicon neighbor into the vacancy and follows simultaneously, requires only 0.8 eV. The result is (in both cases) the structure shown below, a $Si_C (C_{Si})_2$ complex and in a second neighbor distance a carbon vacancy that can dissociate in a next step.

Comparing the energy barriers for the second step of the vacancy assisted C_{Si} migration mechanism on the one hand and the formation of the $Si_C(C_{Si})_2$ on the other hand, the latter is clearly favored. That means, instead of the second step of the C_{Si} migration mechanism rather the addition of the silicon antisite to the $C_{Si} V_C C_{Si}$ complex will take place in this situation. Furthermore, the structure resulting from the recombination process is by 2.7 eV lower in energy, while the second step of the vacancy assisted C_{Si} migration ends up in an energetically higher structure, instead.

Thus, the vacancy mediated mobility of a carbon antisite can lead to the formation of larger complexes. It results, however, not in a simple pair formation, if a Si_C is approached

---

[8] An intermediate structure with the assisting silicon vacancy next to the Si_C will probably not lead to an antisite pair by the mechanism discussed here, but the silicon antisite will recombine with the vacancy, leaving just a C_{Si} and a V_C in second neighbor distance behind
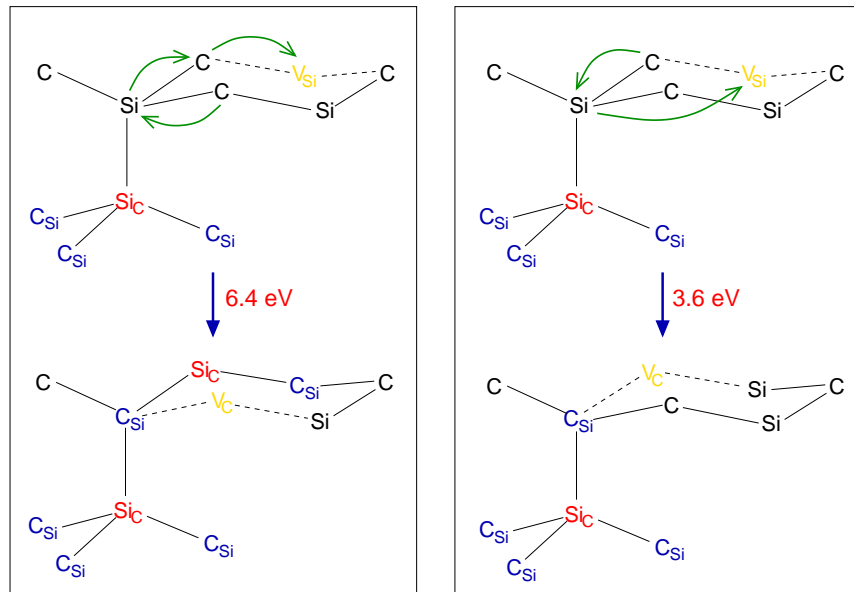
Figure 4.24: *Left:* A ring mechanism for adding one more C_{Si} to a Si_C (C_{Si})$_3$ complex. *Right:* Another mechanism which adds a fourth C_{Si} to the complex. See text for details.

as described here, but the V_{Si} transforms and two C_{Si} are "attached" to the Si_C, while a carbon vacancy remains in second neighbor distance and can dissociate later on.

The mechanism can proceed if sublattice migration of silicon vacancies is activated. If a silicon vacancy approaches the complex obtained so far, consisting of two carbon antisites and one silicon antisite (and possibly the carbon vacancy on the former site of the Si_C, if it is not yet dissociated), the process sketched on the right hand side of Fig. 4.23 can take place. The silicon vacancy can move on as denoted by the arrow in the upper part of Fig. 4.23 (right) with approximately the same activation energy (4.1 eV) as calculated for undisturbed sublattice migration. The carbon ligand follows immediately without a further barrier to the vacant site, such that a complex of a Si_C, three C_{Si} and one or possibly two carbon vacancies is obtained. The total energy is lowered by 3.2 eV, showing that the movement of the V_{Si} in this direction is more likely than a movement onto another Si-site, instead. The carbon vacancies can dissociate from the complex, and the growth of onion-like antisite aggregates is settled.

When a silicon vacancy approaches the structure Si_C (C_{Si})$_3$ just created, the structure Si_C (C_{Si})$_3V_{Si}$ is obtained, which, in contrast to $Si_C V_{Si}$, is stable against spontaneous recombination. However, only the very small energy barrier of 0.1 eV separates it from the 1.4 eV more favorable V_C (C_{Si})$_3$, after the silicon antisite has recombined with the silicon vacancy.

A silicon vacancy that has approached the Si_C (C_{Si})$_3$ complex up to a third neighbor site of the Si_C offers two possibilities of adding a fourth C_{Si} to the complex. The left part of Fig. 4.24 describes a ring mechanism which involves the simultaneous movement of three atoms, as denoted by the green arrows. In this mechanism, not only one C_{Si} is created, but one more pair of antisites[9], which could be the starting point for a next shell of antisites (for the creation of larger onions). The total energy of the two structures is nearly equal, but they are separated by an energy barrier of 6.4 eV.

As an alternative mechanism, the process on the right hand side of Fig. 4.24 has been investigated. Here, the silicon atom next to the Si_C recombines with the silicon vacancy,

---

[9]compare also the discussion of the spiral walk of vacancies in Section 4.2.2.

and its carbon neighbor moves to the C_{Si} position. The carbon vacancy created in this process can, again, dissociate in a next step. The total energy of the structure is reduced by 3.3 eV by the process, and an energy barrier of 3.6 eV makes the addition of a fourth carbon antisite and therewith the completion of the Si_C (C_{Si})$_4$ quite probable, when the temperatures are sufficient to activate migration of silicon vacancies ($\approx$4 eV).

4.5 Influence of other Defects on Migration Processes

High defect concentrations due to high doping rates and/or severe lattice damage result in short distances between the induced defects. So far, we only took into account "isolated" processes in an otherwise perfect crystal lattice. However, reality looks different, and another defect that is present due to the created defect density or a mobile atom – maybe involved in some different diffusion process – may appear in the vicinity of the regarded process.

In this section, only a brief sketch of such influences shall be given, in order to rate possible effects of the close environment of defects on the activation energies of the investigated process. Considering a process with three defects, i. e. antisites or vacancies or even nitrogen-atoms, involved, leads to a defect concentration of $1.2 \cdot 10^{21}$ cm^{-3} if using the standard 4H-supercell with 240 atoms, as described in Chapter 2.
Especially during the first stage of annealing after the ion implantation process, the vacancy concentration can be very high. For both V_{Si} and V_C, concentrations as high as 10^{21} cm^{-3} are reported [97]. Thus, the described arrangement with three defects in a supercell is in the range of the defect concentration, and the assumptions agree with the experimental conditions.

How the presence of a defect affects the height of the energy barriers and the direction of a microscopic jump has been examined for the example of the movement of the silicon vacancy next to a carbon antisite. As shown above, the mobility of the silicon vacancy determines the efficiency of the vacancy assisted mechanism for C_{Si} migration. Whether migration is promoted or hindered depends on the defect, its distance from the place where the migration process is supposed to happen, and the orientation towards the direction of migration.
We have investigated two different directions for the migration of V_{Si}: (a) to an equivalent position with respect to the C_{Si} ("*direction (a)*", as would play a role in the process of moving around C_{Si} in order to obtain directed diffusion), or (b) one site further apart from the C_{Si} ("*direction (b)*", as a first step of dissociation). For these two processes, we compare the "plain" process with those processes we obtain under the influence of another C_{Si}, a Si_C, a V_C, a V_{Si} or a N_C.
The geometrical arrangement of these defects and the direction of migration are indicated in the six small pictures of Fig. 4.25 together with the energy curves along the diffusion paths. The defect considered as a perturbation of the examined process is marked in magenta. In the upper left picture, the "plain" process, i. e. no other defect present, is shown. The energetically more favorable direction in this case is *direction (a)*. This is still true, if another carbon antisite or a silicon vacancy are near (see the center left and right picture in Fig. 4.25). The presence of another C_{Si} lowers both migration barriers, and in case of *direction (a)* the resulting (symmetrical) structure is also lower in energy (migration in the other direction results in a structure equivalent to the initial structure). A silicon vacancy leads to a lowering of the energy in both cases, but implies a transformation of one of the silicon vacancies into a $V_C C_{Si}$ pair, since two silicon vacancies are not stable on neighboring
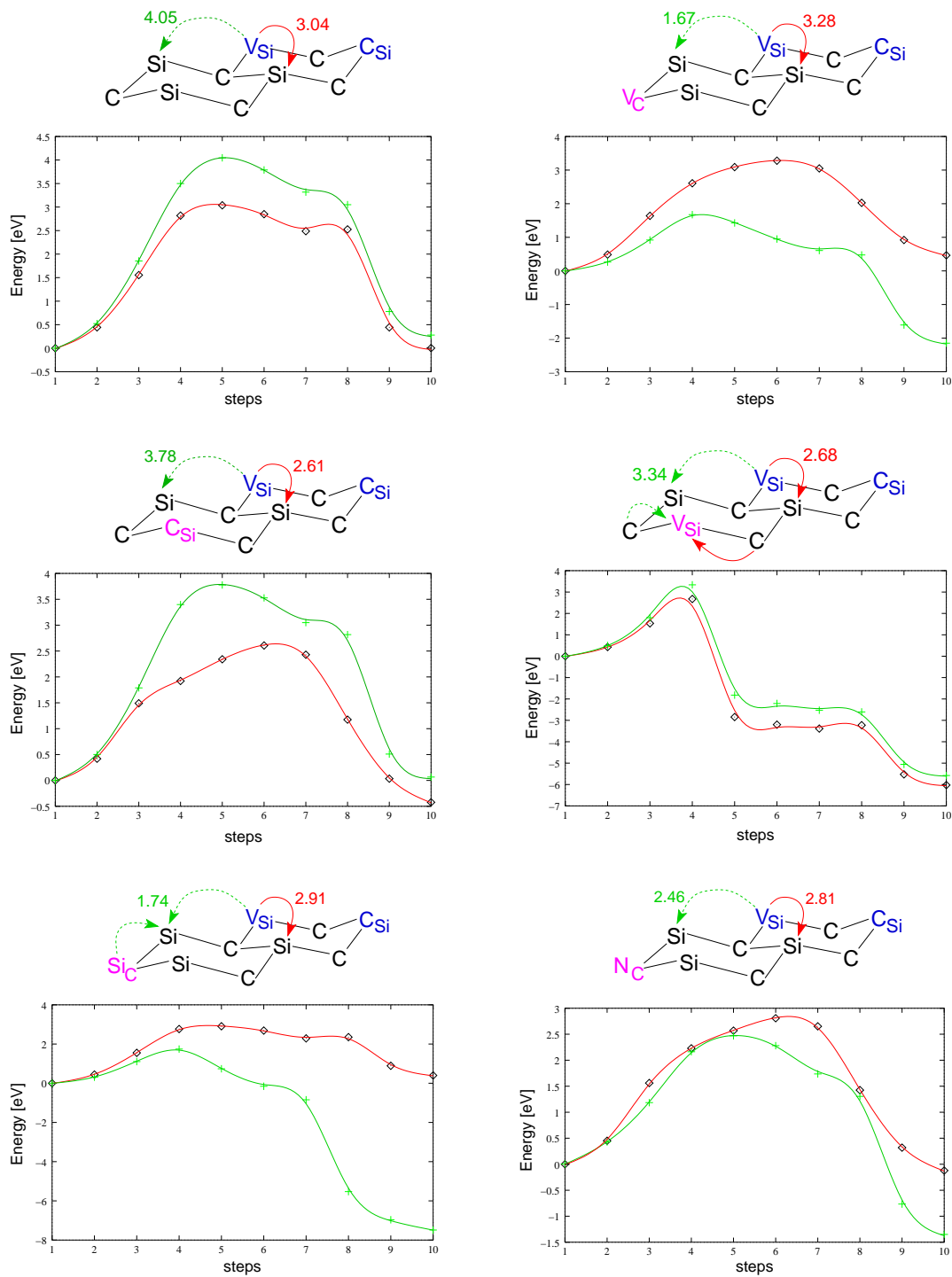
Figure 4.25: The presence of other defects may essentially influence the energy barriers of a migration process. Shown above are two migration processes of V_{Si} as might happen during a vacancy assisted C_{Si}-antisite jumps and their energy curves under the influence of C_{Si}, Si_C, V_C, V_{Si} or N_C (marked in magenta). The red (green) curve in the energy diagram belongs to the processes marked with a red (green) arrow in the structure above the diagram.

sites. A silicon antisite or a carbon vacancy, in contrast, promote migration along *direction (b)*. The formation of a divacancy leads to a stabilization of the structure shown in the upper right picture in Fig. 4.25. The silicon antisite implies a recombination with the V_{Si}, thus leaving only a V_C behind. A nitrogen atom N_C promotes V_{Si}-migration along *direction (b)*, resulting in a $V_{Si} N_C$ pair which might play an important role in the various annealing steps of the silicon vacancy and will be discussed in detail in Chapter 5.

Thus, all these defects that can be expected to be created during the implantation process or in the consecutive annealing process affect the migration barriers and in some case also the resulting structures rather strongly, if they are in third or fourth next neighbor distance to the migrating silicon vacancy.

For the process discussed in the previous section, this means that the formation of the $Si_C (C_{Si})_2$ complex from the initial structure, where a Si_C approaches a $V_C (C_{Si})_2$ complex, may be prevented by the presence of another defect close to the silicon antisite. A silicon vacancy would for example rather lead to a recombination with the Si_C than to the formation of the discussed complex.

4.6 Conclusions for the Formation of Antisite Aggregates

What have we achieved up to now? According to the energetical stability, the formation of larger aggregates of antisites is not unlikely. The mechanisms described in the previous sections can under the discussed assumptions lead to larger aggregates of antisites. The vacancy assisted pair creation is only conceivable for complexes of one or two antisite pairs, larger two-dimensional aggregates cannot be obtained like this. Onion-like structures can result from the movement of single antisites. The results discussed in Section 4.4.2 suggest that aggregation does not go stepwise, e. g. with single carbon antisites approaching a less mobile silicon antisite one by one, but the $Si_C (C_{Si})_2$ complex is formed at once. Mobility of the silicon vacancy is the basis for further addition of carbon antisites to this complex and consequently for "onion-growth".

First calculations have shown that the completely inverted bilayer, which was shown to be very stable in Section 4.2.1, has some promising electronic properties. Fig. 4.26 shows the potential of the structure calculated within SCC-DFTB and with the FHI code. At the side of the C-C bonds, a potential well forms, while at the side of the Si-Si bonds a potential wall is created. Some first one-dimensional ab initio calculations resulted in high tunneling probabilities for free charge carriers through this quantum well/wall structure [68]. Although two-dimensional antisite aggregation to complexes larger than two antisite pairs can obviously not be expected to happen in a crystal *after* growth, it can possibly be created already *during* growth.

With the help of atomic layer epitaxy (ALE) it is possible to grow monolayers of silicon and carbon in a controlled way on the substrate. ALE is a very new technique for SiC but already established in other materials. In the 1990s it was for the first time successfully applied to the growth of cubic and hexagonal SiC on silicon substrate. A detailed description of the method and its application to various materials can be found in Refs. [92, 93, 94, 95, 96]. The basic principle is the alternating supply of certain reactants in a comparably low temperature range, typically 600-950°C [92].
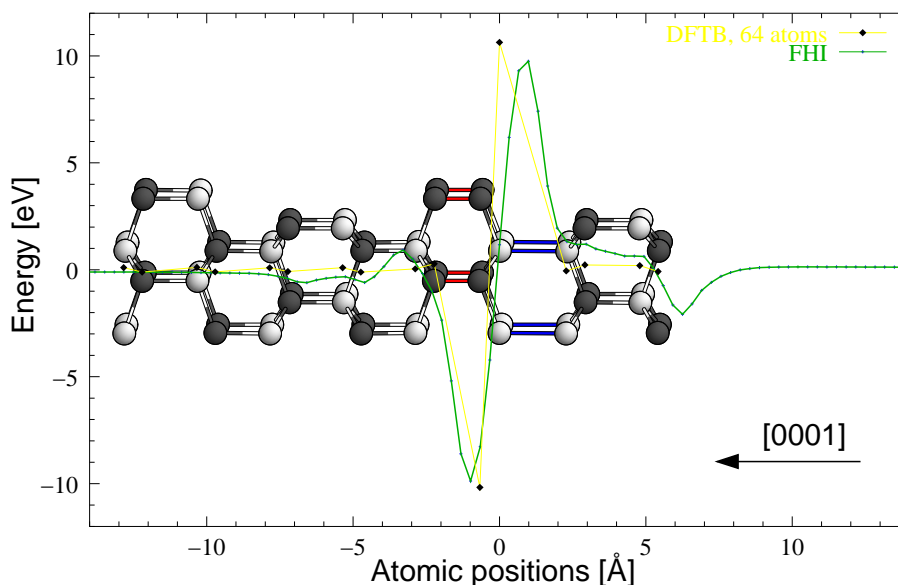
Figure 4.26: Potential wall and well of the inverted bilayer, calculated within SCC-DFTB and FHI.

These low temperatures lead naturally to a low growth rate, so that this method is not suitable for bulk growth. Nevertheless, the low temperatures might be advantageous for our aim: silicon and carbon monolayers can be grown either hetero- or homoepitactically, so that during growth along [0001] the polarity of the material can be changed. If the alternation of the reactants is stopped and the growth procedure, instead, repeated with the same reactant a second time, a Si-Si or a C-C sequence is created. Like this, stress-free sequences of silicon and carbon monolayers could be grown, including Si-Si-C-C sequences like the inverted bilayer. This would offer a variety of possibilities to design two-dimensional quantum devices.

One crucial point for the realization of such devices is the stability of the created sequences of Si- and C-monolayers during the growth process. First molecular dynamics investigations of an inverted bilayer at the surface of a crystal with and without hydrogen passivation indicate that considerably higher temperatures than used in ALE should be required to induce either a dissociation of the surface atoms or a re-ordering to a "normal" Si-C bilayer with the original polarity. Nevertheless, more detailed investigations are currently under work both on the experimental side to optimize the growth technology by e. g. varying the reactants and on the theoretical side, where we continue tunneling calculations and molecular dynamics simulations.

Another result has been achieved in the previous sections: Having once found a mechanism for the migration of a defect and having calculated the entropies for minimum energy and saddle point geometry, we can give an estimate for the diffusivity D of defects. With the activation energy E_a of the process, the diffusivity can be expressed as

$$D = D_0 \, exp \left(-\frac{E_a}{kT} \right) \ , \tag{4.2}$$

where D_0 is the diffusion coefficient

$$D_0 = \frac{d^2\,\omega}{2} p\,exp\left(\frac{\Delta S}{k}\right)\;.\tag{4.3}$$

Here, ΔS is the entropy difference between the ground state and the saddle point structure, d is the distance between the two equivalent minima (initial and final structure), and ω is the attempt frequency of the jump, commonly approximated by the Debye-frequency $(\omega_D(\text{SiC}) = 1.6 \cdot 10^{13}\,\text{s}^{-1})$.

In case of vacancy assisted diffusion, which will be discussed in the following, p is the likelihood of finding a vacancy on a neighboring site, that is the vacancy concentration divided by the number of sites in the sublattice. In case of direct diffusion, $p = 1$.

An important quantity for aggregate formation is also the diffusivity. An estimate for the diffusivities of vacancies and antisites on the basis of the mechanism presented above can be obtained using Eq. 4.2 and 4.3. For the migration of V_C and V_{Si} on their sublattices we get a diffusivity of $D(V_C) = 2.49 \cdot 10^{-15}\,\text{cm}^2/\text{s}$ and $D(V_{Si}) = 8.77 \cdot 10^{-14}\,\text{cm}^2/\text{s}$ at T=1800 K. Thus, the silicon vacancy has a slightly higher mobility than V_C, which agrees with the observation that in as-grown material, where no interstitials are available, V_C survives higher annealing temperatures than V_{Si} [98]. Annealing at 1600°C for one hour seems to remove V_C [21].

To calculate the diffusivity for the vacancy assisted migration of Si_C and C_{Si}, we need to know the concentration of vacancies in the material. At the early stage of annealing directly after implantation, concentrations as high as $10^{21}\,\text{cm}^{-3}$ are observed for both V_C and V_{Si}. Using this concentration, we obtain $D(C_{Si}) = 2.70 \cdot 10^{-10}\,\text{cm}^2/\text{s}$ and $D(Si_C)=4.09 \cdot 10^{-16}$ cm^2/s for the antisite migration. Thus, the diffusivity of the C-antisite is faster than that of the Si-antisite or the vacancies, which has to be attributed not only to the lower activation energy, but also to the larger change in entropy ΔS at the saddle point. We get the following ordering of diffusivities: $D(C_{Si}) > D(V_{Si}) > D(V_C) > D(Si_C)$. Nevertheless, since the mobility of V_{Si} is required for the C_{Si} motion, $D(V_{Si})$ is determining this process. In case of Si_C, $D(Si_C)$ is the slowest and thereby determining diffusivity.

Accordingly, the migration of C_{Si} is much easier than Si_C migration. Consequently, the Si-centered onion $Si_C(C_{Si})_4$ should be more likely to be created than the inverse onion-structure, the formation of which is hindered by the low mobility of Si_C. A mechanism for the stepwise creation of $Si_C(C_{Si})_4$ has been proposed in the previous section. Furthermore, other aggregates with e. g. equal numbers of antisites or an excess of C_{Si} may be formed by this process [91].

Naturally, the described mechanism of vacancy assisted migration of C_{Si} and also Si_C may, depending on the conditions, also apply to the formation of differently formed aggregates of antisites. That the presence of other defects in the close neighborhood can have a significant influence on the activation energy and also the result of a migration mechanism has been shown in the previous section. Accordingly, the growth of onion-like aggregates may be hindered by some other defect, leading to a differently formed, e. g. two-dimensional antisite aggregate.

Chapter 5

Nitrogen related Defects in SiC

The construction of SiC-devices requires n-type and p-type doped crystals. As illustrated in the introduction, nitrogen is the common dopant in SiC for creating n-type material, because the nitrogen atoms are built into the SiC-lattice as shallow donors. As already pointed out in Chapter 2, the low diffusivities of defects of nearly any type in SiC imply that doping has to be done by ion implantation, which, however, has the disadvantage of creating a massive lattice damage, up to the amorphization of crystal regions, if e. g. the temperature during implantation is chosen too high [17, 104].

Unfortunately, doping with nitrogen does not lead to a higher concentration of free charge carriers than $\approx 10^{19}$ cm^{-3}, but saturates according to Hall- and DLTS-measurements at this value [31]. A post implantation treatment consisting of further implantation with hydrogen, helium, boron or aluminum and further annealing can lead to a reduction of the free charge carrier compensation – with $\approx 30\%$ recovery at $\approx 700°$C up to a full recovery at annealing temperatures above $\approx 1050°$C [32], see Fig. 5.1.

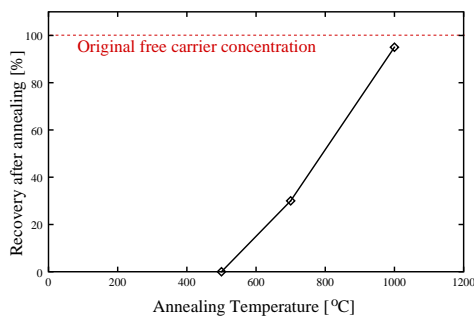**Figure 5.1:** Recovery of the free carrier concentration versus annealing temperature as measured by Åberg et al. [32, 33]. At $\approx 700°$C 30%, at $\approx 1050°$C 100% recovery are observed.

Since they observe a very efficient passivation, Åberg et al. propose the formation of complexes with elementary point defects, such as vacancies or interstitials [32]. As the silicon vacancy unlike the carbon vacancy appears commonly negatively charged in n-type material, and Coulomb attraction may enhance aggregation, they suggest the formation of $V_{Si} N_C$ pairs as reason for the passivation of the nitrogen atoms and explain the observed recovery process by the dissociation of these pairs.

As will become clear later in this chapter, the described behavior of the free charge carrier concentration is closely related to the annealing stages of the silicon vacancy. The low temperature annealing stage at $750°$C can be ascribed to either recombination with interstitials (Frenkel pairs) or the transformation into a $C_{Si} V_C$ pair, like discussed in detail in Chapter 3. Further weak and strong annealing stages of mostly uncertain origin have been observed in capacitance spectroscopy experiments [99], positron annihilation studies [17], and EPR measurements

[21]. According to these experiments, a weak annealing stage is found at $\approx 1050°$C, while the final strong annealing stage is found around $1400°$C [14, 17]. Also in these works, the formation of nitrogen–related complexes, especially nitrogen-vacancy pairs, is proposed to play an important role during the annealing processes.

The question, which nitrogen–related complexes are stable in SiC and for which of them a formation process exists that has an activation energy that can be correlated to the observed annealing temperatures is still unanswered in the literature. We will show in the following sections that a consistent picture can be drawn on the basis of an interstitial based diffusion mechanism.

5.1   Nitrogen–related Pair Defects

In principle, any defect that is present after the implantation process, could form a pair defect with a nitrogen atom: other nitrogen atoms — leading to $N_C N_{Si}$ pairs, vacancies — leading to $V_{Si} N_C$ or $V_C N_{Si}$ pairs, or antisites — resulting in $N_C C_{Si}$ or $N_{Si} Si_C$ pairs. The first two cases, nitrogen pairs and nitrogen–vacancy pairs are well known defects in diamond [100, 101], and the similarity of both materials in many of their properties suggests that similar defects can as well be expected in SiC. Experiments indicate that the isolated nitrogen is usually built in on the carbon site in SiC as N_C [102, 103], and the existence of a N_{Si} is rather uncertain and at least not very probable, as can also be affirmed by our calculations, see Section 5.1.4.

The formation of $N_C N_{Si}$ pairs becomes already doubtful by this, and additionally, the pair is slightly less stable than its constituents N_C and N_{Si} .

Since the vacancy concentration in the implanted region can be expected to be about two orders of magnitude higher than the concentration of the implanted species [104], it is very probable that vacancies are involved in the aggregates. Nitrogen–vacancy pairs are, thus, more likely than pure nitrogen aggregates. This is affirmed by the experimental results of Kawasuso et al. as well as Åberg et al.[17, 32].

Based on their positron annihilation and DLTS measurements, they suggest the presence of nitrogen-vacancy pairs – and, in fact, Vainer and Il'in ascribe their observation of the so-called P12-center in N-doped 6H-SiC to a silicon vacancy–nitrogen pair [85]. Calculations of the hyperfine interactions of the $V_{Si} N_C$ pair within the Green's function based Linear Muffin Tin Orbital (LMTO) method confirm this ascription, although presuming a different symmetry of the electronic structure (C_{1h} instead of C_{3v}), see Table 5.1. More details of these calculations and the revised correlation of the EPR-signal with the defect model can be found in Ref. [62].

But how can such pairs develop? We want to investigate the processes that could take place directly after the ion implantation process. That means, to a great deal, nitrogen is most likely built in substitutionally on carbon sites as N_C , and vacancies, both isolated or in form of divacancies, are present in the implanted and damaged region of the crystal. Furthermore, carbon split-interstitials that have not yet recombined with close vacancies can be expected to be found.

Table 5.1: Hyperfine interactions of the $V_{Si}N_C$ pair, calculated within LMTO-ASA

EPR	Defect	state		^{13}C (-1,-1,1)		^{14}N (1,1,1)	
				a	b	a	b
P12	$V_{Si}N_C$	$^2A_1'$	C_{1h}	32.6	7.3	–1.6	0.26
			Exp.	33.6	4.2	±2.4	0.18
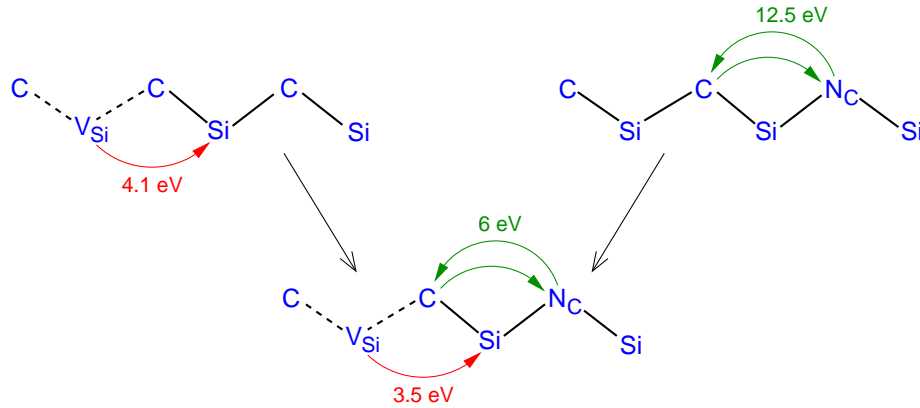
Figure 5.2: Creation of a $V_{Si}N_C$-pair by sublattice migration of either the silicon vacancy or the nitrogen atom.

5.1.1 Pair formation by aggregation of V_{Si} and N_C

The most simple mechanism to imagine for the formation of $V_{Si}N_C$ pairs is a sublattice migration process of either of the constituents. To start the discussion of this mechanism with the sublattice migration of the silicon vacancy towards the N_C, we can recall the results of Chapter 3: sublattice migration of V_{Si} can be activated with an energy of ≈4.1 eV (in the otherwise perfect lattice). This energy would be needed for bringing together distant V_{Si} and N_C. However, due to the high defect densities in the implanted region, it is rather probable that V_{Si} and N_C are already quite close together, which does not leave the energy barriers unaffected. For a third neighbor distance (as sketched in Fig. 5.2), the migration barrier is reduced to 3.5 eV.

On the other hand, the nitrogen atom could migrate on the carbon sublattice until it meets a silicon vacancy. Without the help of other defects, i. e. vacancies, this process is based on very costly exchange processes between N- and C–atoms. In the otherwise perfect lattice, such a process, similar to the Pandey-process[1] requires ≈12.5 eV to be activated and can, therefore, be ruled out immediately. Regarding, again, a V_{Si} and an N_C in a third neighbor distance, this activation energy is – due to the in this case only threefold coordinated C-atom – reduced to 6 eV. The migration of the silicon vacancy is, thus, energetically always more favorable, no matter how far the vacancy and the N-atom are separated.

Thus, if the external conditions, i. e. temperature and defect concentration, allow vacancy

---

[1]compare Chapter 4, where this mechanism is described for the formation of antisite pairs in the perfect lattice

migration, the pair might be created by this mechanism (with the nitrogen atom staying on its site). However, the energies needed to activate this mechanism are too high to explain the experimental observation of the pair already before high temperature annealing.

A more complicated mechanism of aggregation with a lower activation energy seems to be needed, therefore. Recalling our results for the migration of carbon split-interstitials, an interstitial based mechanism might be an alternative. We have, therefore, examined the interstitials that are present after implantation and their migration mechanisms.

5.1.2   Mobilizing N_C — Creation of N-interstitials

Certainly present are carbon split-interstitials. Their migration can, as discussed in detail in Chapter 3, be activated with 2.9 eV. If a $(CC)_C$ meets a carbon vacancy or a silicon vacancy, it will recombine to either the ideal lattice or to a carbon antisite. The question is now, what happens when a $(CC)_C$ split-interstitial meets an N_C ?

In principle, two things could happen: its migration mechanism could stop or change
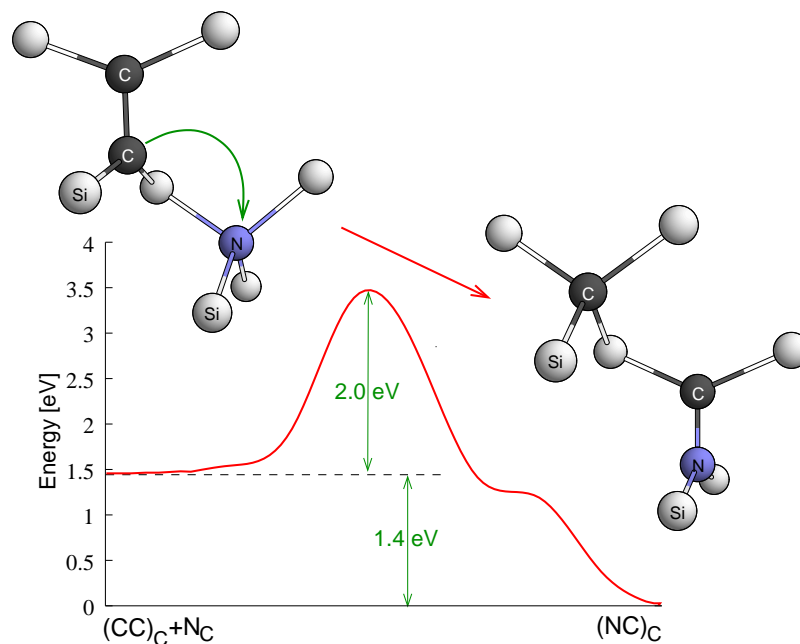
Figure 5.3: A $(CC)_C$ split interstitial moves to the substitutionally built in N_C, resulting in a $(NC)_C$ split-interstitial.

direction. On the other hand, the C-atom could move to the site of N_C, if this is energetically more favorable. Actually, the latter alternative is what happens: The C-atom of the $(CC)_C$ can with an even lower energy be activated to move to the site of N_C than to carbon site with a carbon atom, resulting in an $(NC)_C$ split-interstitial. In Fig. 5.3 the initial and final structure of this process is shown above the energy along the migration path. The newly created $(NC)_C$ split-interstitial is even lower in energy than the $(CC)_C$ split-interstitial next to an N_C, thus the formation of these split-interstitials is more likely than the alternative of a change of the migration direction of the $(CC)_C$.

The geometrical structure of $(NC)_C$ is very similar to that of $(CC)_C$, only with slightly shorter bonds at the N-atom. As denoted in the energy diagram, the energy barrier is 2.0

eV, while 1.4 eV are gained by this process.

N-atoms as "usual" (instead of split-) interstitials have been found to be instable: without an energy barrier, they move to a nearby C-site during the relaxation of the structures, resulting in $(NC)_C$ split-interstitials. This has been found for all different interstitial sites in 4H- and 3C-SiC. According to this result, it becomes conceivable to find these $(NC)_C$ split-interstitials besides substitutionally built in N-atoms directly after implantation, as well.

It is not surprising that these $(NC)_C$ split-interstitials can migrate in a similar way as the $(CC)_C$ split-interstitials. The N-atom of the $(NC)_C$ can move a C-site further, requiring ≈ 2.5 eV, thus slightly lower than calculated for the $(CC)_C$ split-interstitial. The C-atom of the $(NC)_C$ would need 3.4 eV to move to the next carbon site, so that the migration of the N-atom is preferred and will maintain.

One further kind of movement is needed to render nitrogen migration possible through the SiC-lattice: a change of the direction of migration might be required, e. g. when the N-atom meets another defect that would otherwise stop the migration process. A rotation
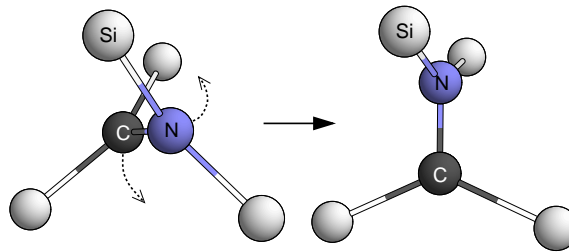

Figure 5.4: Rotation of the $(NC)_C$ split-interstitial.

of the $(NC)_C$ split-interstitial on the C-site into another of the six possible orientations of the interstitial (see Fig. 5.4) requires an activation energy of 0.8 eV – for the $(CC)_C$ split-interstitial, a similar value of 0.6 eV was obtained. After the rotation, the sublattice migration mechanism can be continued.

After all, we have found a way to mobilize N_C and can now turn to our aim, to find a mechanism for the nitrogen-vacancy pair formation.

5.1.3   Recombination of $(NC)_C$ with divacancies $V_C V_{Si}$

Provided sufficiently high annealing temperatures, nitrogen can be mobilized as described above and move through the SiC-lattice in form of $(NC)_C$ split-interstitials. Due to the high vacancy concentrations after implantation, these split-interstitials will probably very soon come across a vacancy or a divacancy. Since it seems to be the most simple way to create a nitrogen–vacancy pair, we will first discuss the case that an $(NC)_C$ meets a divacancy $V_C V_{Si}$ [2].

 Two cases have to be distinguished: $(NC)_C$ can approach the divacancy either from the side of the carbon vacancy V_C or from the side of the silicon vacancy V_{Si}. If an $(NC)_C$ has arrived at a second neighbor site of the carbon vacancy of a $V_C V_{Si}$ (see Fig. 5.5 (left)), it will fill up V_C, resulting in a $V_{Si} N_C$ pair. Only 0.2 eV are needed to activate this recombination process, and 7.4 eV are gained. On the other hand, $(NC)_C$ can approach $V_C V_{Si}$ from a C-site being third neighbor to the silicon vacancy of the $V_C V_{Si}$, as in Fig. 5.5 (right). The N-atom does, however, not move through the divacancy in order to reach the vacant

---

[2]The presence of divacancies directly after implantation has been reported from various experimentalists, and the strong binding energies (see Chapter 3) back up this observation.
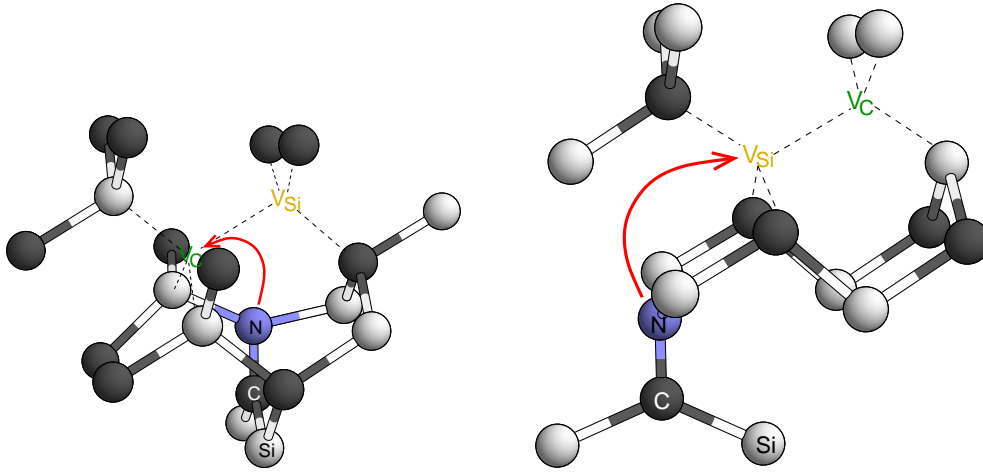
Figure 5.5: The N-atom of a $(NC)_C$ split-interstitial can fill up the carbon site (*left*) or the silicon site (*right*) of a divacancy.

C-site, but stays on the Si-site. The resulting complex is a $V_C N_{Si}$ pair. The recombination process requires 1.0 eV to be activated, and 8.0 eV are gained. In Fig. 5.6, the change in energy during both migration processes is shown. The "inverse" pair, $V_C N_{Si}$, is only by
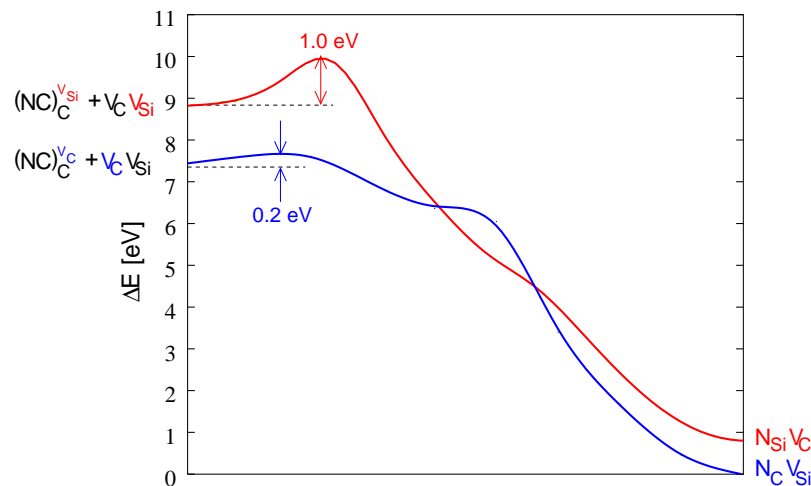
Figure 5.6: The energy curves for the two possibilities a $(NC)_C$ can recombine with a divacancy.

0.8 eV less stable than the $V_{Si} N_C$ pair. In the neutral charge state, a migration barrier for the N-atom of 2.4 eV separates it from the $V_{Si} N_C$ pair. In the negative charge state, the $V_{Si} N_C$ pair is by even 1.6 eV more stable, and the transformation of the inverse pair to this structure costs only 2.1 eV.

However, in the positive charge state, the energetical order is reversed: in this case, the $V_C N_{Si}$ pair is by ≈ 0.1 eV lower in energy than the $V_{Si} N_C$ pair, and the energy barrier between the two pairs is ≈ 3.4 eV. According to these results, the nitrogen–vacancy pair seems to be a bistable defect which, depending on its charge state, can appear in form of a $V_{Si} N_C$ pair (n-type) or a $V_C N_{Si}$ pair (p-type). Since we are here generally focusing on n-type material and the role of nitrogen in p-type material is only of secondary importance, we can suppose that the concentration of $V_{Si} N_C$ pairs prevails.

Figure 5.7: If an $(NC)_C$ approaches a silicon vacancy, it does not fill up the V_{Si} but instead kicks out one of the carbon ligands of the vacancy to an interstitial site $((CC)_C)$.

5.1.4 $(NC)_C$ meeting isolated vacancies

Naturally, during its migration through the lattice an $(NC)_C$ split-interstitial can come across not only divacancies but also isolated vacancies. Meeting a carbon vacancy, the N-atom recomb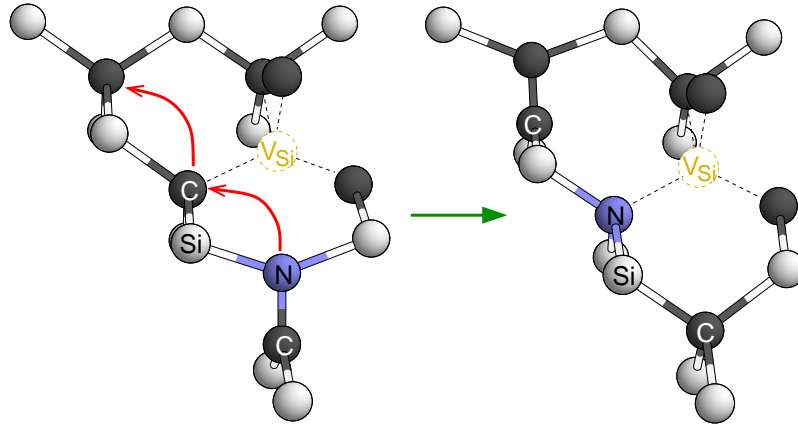ines with the vacancy as expected, resulting in the substitutional N_C: From a second neighbor distance, less than 0.1 eV are needed for this process, and the resulting N_C is 9.2 eV lower in energy. The migration mechanism is stopped, and the nitrogen atom can only be re-mobilized, if a $(CC)_C$ kicks it out into a split-interstitial geometry, as described in Section 5.1.2.

The situation is substantially different for a silicon vacancy. One might expect a simple recombination, like in case of the carbon vacancy, resulting in a substitutional N_{Si}. Our calculations show, however, that such a recombination does not take place, but one of the carbon ligands of the vacancy is kicked out, instead. As shown in Fig. 5.7, the N-atom of an $(NC)_C$ that has approached a silicon vacancy up to a third neighbor distance can kick out one C-ligand with an activation energy of 2.9 eV, lowering the energy by 1.8 eV. The N-atom is then three-fold coordinated built in on the C-site – a $V_{Si}N_C$ pair results. The C-atom has in this mechanism been moved to the next C-site where it forms a $(CC)_C$ split-interstitial with the C-atom on this site. From there, it can dissociate in a next step and migrate through the lattice as described before.

Thus, the kick-out mechanism with a ligand of a silicon vacancy is another possibility to create a $V_{Si}N_C$ pair. Though the activation energy needed for this process is higher than in case of the recombination of $(NC)_C$ with divacancies, it is of the same order of magnitude as the activation energy needed for the sublattice migration of carbon split-interstitials.

That means, at low annealing temperatures, a recombination process with divacancies will be responsible for the creation of $V_{Si}N_C$ pairs, while in cases where long-range diffusion is expected due to larger defect-defect distances, and $(CC)_C$ sublattice migration as well as $(NC)_C$ sublattice migration start to become important, the kick-out process can become accountable for $V_{Si}N_C$ pair creation, as well. Additionally, this kick-out mechanism can contribute to the annealing of silicon vacancies in the respective temperature range[3].

---

[3]A tentative correlation between the calculated activation energies and experimentally observed annealing temperatures is given in Section 5.3.

5.1.5 The $C_{Si}N_C$ pair as an alternative

The $V_{Si}N_C$ pair and the inverse $V_C N_{Si}$ pair are not the only stable nitrogen–related complexes in SiC. Obviously, the probability of pair formation with vacancies is rather high compared to the pairing with other defects, since under the assumed conditions the vacancy concentration is extremely high. However, vacancies may also promote the formation of other defect complexes without being directly involved in the resulting complex.

A very stable complex to be discussed in this context is the $C_{Si}N_C$ pair. Stoichiometrically equivalent to a N_{Si}, it is by ≈ 3 eV lower in energy, and the exchange process of the N-atom with the C-atom requires only ≈ 4 eV – much lower than the energies found for other exchange processes, compare the exchange of N_C defects with second neighbor carbon atoms, which was discussed in the beginning of this chapter. Nevertheless, 4 eV are too high to explain the existence of the $C_{Si}N_C$ pair in a temperature range below the final annealing stage of the silicon vacancy (activation energy for sublattice migration ≈ 4.1 eV), which has been observed experimentally at $\approx 1400°$C.

There are, however, alternative ways to create the $C_{Si}N_C$ pair with lower activation energies. Reconsidering the initial structure of the kick-out process between a $(NC)_C$ and a V_{Si} in the previous section, we find an alternative final structure (compare top structures in Fig. 5.8). The behavior of the N-atom remains unchanged, but instead of kicking the carbon ligand to a $(CC)_C$ on a neighboring C-site, the N-atom kicks the C-atom throughout the vacancy to the antisite position C_{Si}. This mechanism requires only 2.0 eV, i. e. 0.9 eV less than the kick-out process described before. Furthermore, a large energy gain is linked with this process: the energy of the $C_{Si}N_C$ pair is 10.6 eV lower than the $(NC)_C$ next to the silicon vacancy.
That means, for the same initial situation, a $(NC)_C$ split-interstitial and a V_{Si} in third neighbor distance, these processes have to be regarded as competing processes with the result, $C_{Si}N_C$ or $V_{Si}N_C$ and a $(CC)_C$, depending on the disposable energy.

Alternatively, the $C_{Si}N_C$ pair can be created as shown in Fig. 5.8 (center and bottom). Part of the silicon vacancies may have transformed to $V_C C_{Si}$ pairs[4]. An $(NC)_C$ split-interstitial might therefore meet such a $V_C C_{Si}$ pair rather than a V_{Si} (see the center left structure in Fig. 5.8). With 0.3 eV the recombination of the N-atom with the carbon vacancy can be activated, gaining 8.8 eV.
As a third possibility, we considered the case of carbon split-interstitials $(CC)_C$ approaching a $V_{Si}N_C$ pair, see the bottom structure in Fig. 5.8. A recombination of the C-atom of the $(CC)_C$ with the silicon vacancy results in a carbon antisite, while the N-atom remains on its site. With 1.9 eV, this process can be activated, i. e. a lower energy than needed for the $(CC)_C$ sublattice migration, and 9.7 eV are gained.
Thus, we have found several ways to create $C_{Si}N_C$ pairs at rather low energetical cost. The large energy gains linked with these processes indicate the high stability of this pair defect and make its creation yet more likely.

The role the discussed pair defects, $V_{Si}N_C$ and $C_{Si}N_C$, play in the observed annealing behavior of the silicon vacancy and the observed saturation of the free charge carrier concentration in highly N-doped material and its recovery as reported by Åberg et al. is the subject of the next section.

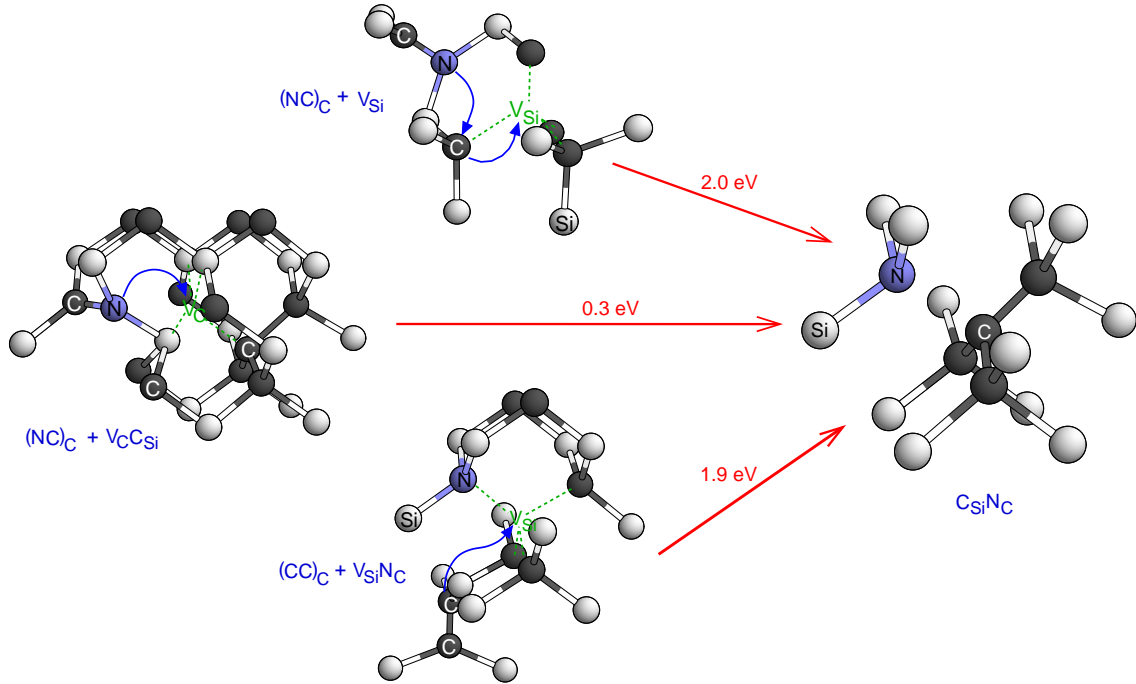[4]This process requires 1.7 eV, compare Section 3.1.3.

Figure 5.8: Three possible ways to create a $C_{Si}N_C$ pair (right hand side). *Top:* $(NC)_C$ approaches V_{Si}. *Center:* $(NC)_C$ approaches $V_C C_{Si}$. *Bottom:* $(CC)_C$ approaches $V_{Si}N_C$ pair. The activation energies linked with the mechanisms are indicated above the arrows.

5.2 Dissociation or Aggregation

5.2.1 Dissociation of $N_C V_{Si}$ pairs

Åberg et al. have found that in N-doped 4H-SiC the reduction of the free charge carrier concentration upon additional ion implantation with H, He, Al, and B is compensated in part by post-implantation annealing above 700°C [32, 33]. At a temperature around 1000°C they obtain a full recovery of the free charge carriers (compare Fig. 5.1) and suggest the dissociation of implantation-induced nitrogen-related complexes, probably $V_{Si}N_C$ pairs, as an explanation for this observation.

Complex formation with the newly implanted ions seems unlikely, because the concentrations can not explain the observed efficiency of compensation. With the Debye frequency $\omega_{Debye} = 1.6 \cdot 10^{13}$ s^{-1} as attempt frequency $\omega_{attempt}$ they derive a dissociation barrier ΔG from the concentration of nitrogen donors

$$N_d(t) = N_d^\infty \cdot \left[1 - exp\left(-\omega_{attempt} \cdot exp(-\frac{\Delta G}{k_B T}t) \right) \right] , \qquad (5.1)$$

where N_d^∞ is the concentration after full doping recovery. With the measured concentrations for 700°C they obtain $\Delta G = 3.2$ eV [33] as an estimation of the activation energy for the dissociation.

If we now consider the mechanisms discussed in the previous sections for the creation of $N_C V_{Si}$ pairs, we find the lowest energy dissociation process for the silicon vacancy moving one Si-site further, namely 5.5 eV. As discussed in this context, sublattice migration of N-atoms requires much higher energies, and due to the large energy gains in the recombination processes described for the $(NC)_C$ split-interstitials with divacancies, these

mechanisms (in the opposite direction as described before) can be ruled out, as well.
These calculated activation energies can, thus, not explain the dissociation as proposed in
Ref. [33]. As Coulomb attraction may additionally hinder a dissociation into V_{Si} $^-$ and
N_C $^+$, which further increases the discrepancy between our calculated 5.5 eV and the 3.2
eV proposed in Ref. [33].

An alternative explanation of the experimental findings may be found in further aggre-
gation of nitrogen. The formation of larger nitrogen–related complexes is, furthermore,
encouraged by the observed high ratio of compensation per vacancy.

5.2.2 Further Aggregation: the formation of V_{Si} $(N_C)_n$-complexes

Provided high concentrations of nitrogen, the aggregation process does not have to stop
with the formation of V_{Si} N_C pairs. Especially at high temperatures, which allow the
activation of migration processes that require higher activation energies, further nitro-
gen atoms can be mobilized. Aggregation is no longer limited to the low energy recom-
bination processes of close nitrogen atoms and vacancies or divacancies, but long-range
diffusion becomes important, since sublattice migration of $(NC)_C$ (E_{activ}=2.5 eV) and
$(CC)_C$ (E_{activ}=2.9 eV) and thereby further creation of $(NC)_C$ by the mechanism $(CC)_C$ +
$N_C \longrightarrow (NC)_C$ (E_{activ}=2.0 eV) can take place. We will, therefore, investigate what happens
when further $(NC)_C$ or $(CC)_C$ approach V_{Si} N_C pairs.

The migration of $(CC)_C$ to $V_{Si} N_C$ pairs leads to $C_{Si} N_C$ pairs, as already discussed in Section
5.1.5. This C_{Si} N_C pair will be discussed in more detail in a later section.

If an $(NC)_C$ meets a V_{Si} N_C pair, it does
not recombine with the silicon vacancy of the
pair, which would result in an N_{Si} N_C pair.
Instead, performing a kick-out mechanism
as in case of the isolated V_{Si} (see Sec-
tion 5.1.4), the N-atom can be built in on
the site of one of the remaining three C-
ligands of the silicon vacancy, resulting in
a V_{Si} $(N_C)_2$ complex and a $(CC)_C$ split-
interstitial that can dissociate in a next
step.

Figure 5.9: The very stable V_{Si} $(N_C)_4$ com-
plex may be a final annealing product of the
silicon vacancy in n-type SiC.

This mechanism can be imagined to happen also
for one or two more $(NC)_C$ approaching the com-
plex: V_{Si} $(N_C)_n$ complexes can be created by a
subsequent addition of $(NC)_C$ split-interstitials to
V_{Si} $(N_C)_{n-1}$ complexes. Approaching the silicon
vacancy of a V_{Si} $(N_C)_{n-1}$ complex, one of the ligands can be kicked out, resulting in a
V_{Si} $(N_C)_n$ complex and a $(CC)_C$ split-interstitial. The activation energies for these pro-
cesses and the respective energy gains do not vary significantly with n: about 2.9 eV are
needed for activation, while the resulting complex is by $\approx$2 eV lower in energy.

With $n = 4$, a completely inactive complex has been created: the four nitrogen atoms of
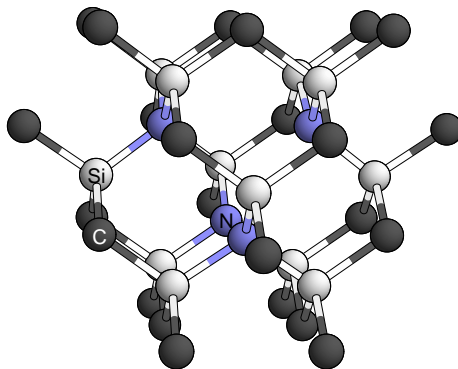
Table 5.2: Transition levels of $V_{Si}(N_C)_n$ calculated within LMTO and experimentally observed acceptor levels.

Defect	Transition	LMTO	Exp.
$V_{Si}N_C$	–2/–3	–0.34	–0.35
$V_{Si}(N_C)_2$	–1/–2	–0.59	–0.60
$V_{Si}(N_C)_3$	0/–1	–1.17	–1.10
$V_{Si}(N_C)_4$		inactive	

$V_{Si}(N_C)_4$ (see Fig. 5.9) fully passivate the silicon vacancy. The formation of this complex could explain the observed high compensation ratio at high N-concentrations.

At the first view, such a complex may seem "exotic", but it can be motivated from investigations of color centers in diamond. There, the respective VN_4 complex, known as "B-center" is a very prominent defect center [105]. In SiC as well as in diamond this complex turns out to be extremely stable: the binding energy has been calculated to be ≈ 10 eV. The complex has T_d-symmetry, and the nitrogen atoms relax only slightly outwards (4 %), see Fig. 5.9. Its electrical and optical inactivity and these geometrical facts will, however, make its observation and thereby the proof of its existence difficult [5].

The stability of the $V_{Si}(N_C)_4$ complex is also reflected in the energy needed to activate its dissociation. The process $V_{Si}(N_C)_4 \longrightarrow V_C V_{Si}(N_C)_3 + (NC)_C$ requires as much as 9.9 eV to be activated, but since the energy of the resulting structure is by 8.9 eV higher, recombination of the $(NC)_C$ with the V_C will take place immediately.
The lowest energy alternative to destroy the complex is by a $(CC)_C$ split-interstitial approaching it and kicking out one of the N-atoms: $V_{Si}(N_C)_4 + (CC)_C \longrightarrow V_{Si}(N_C)_3 + (NC)_C$. The activation energy of this mechanism is 4.9 eV, but still the resulting complex is by ≈ 2.0 eV higher in energy. Dissociation is according to these results very unlikely, and $V_{Si}(N_C)_4$ is accordingly a good candidate for a final annealing product of the silicon vacancy.

The formation mechanism of the $V_{Si}(N_C)_4$ complex is based on the subsequent aggregation of $(NC)_C$ to the smaller $V_{Si}(N_C)_n$ complexes. It is not yet clear whether these complexes have been observed experimentally, but there is strong evidence for this due to the results of Ballandovich and Violina [99]. Using capacitance spectroscopy, they found three deep acceptor levels in 6H-SiC with energies at E_C–0.35 eV, E_C–0.6 eV, and E_C–1.1 eV, thermally stable up to 1050°C [99]. Another experimental indication comes from the positron lifetime spectroscopy experiments of Kawasuso et al. [17], according to which the disappearance of these acceptor levels is correlated with a weak annealing stage for vacancy-related defects. According to our LMTO-calculations, the energies for the uppermost acceptor levels of $V_{Si}(N_C)_n$, n=1,2,3 agree with the experimental data, compare Table 5.2.

If the assignment of the experimental findings to the $V_{Si}(N_C)_n$ complexes should be tenable, the observed vanishing of the acceptor levels has to be explained in our model, as

---

[5]In diamond, the B-center could neither be seen by positron annihilation, since a distinction between an isolated vacancy and the complex could not be made.

well. The dissociation of the complexes is rather improbable, since not only the $V_{Si}N_C$ pair and the $V_{Si}(N_C)_4$ complex but also the two complexes with two or three N-atoms have very high binding energies, and the high dissociation barriers cannot be linked to the reported temperature of $\approx 1050°C$.

The alternative explanation may, again, be found in further aggregation instead of dissociation. An annealing product with a shallower donor level would explain the "vanishing" of the levels.

5.2.3   Formation of $C_{Si}(N_C)_n$ complexes

Reconsidering the results of Sections 3.2 and 5.1.2, the energy needed for the activation of $(CC)_C$ sublattice migration is only slightly higher than the activation energy of $(NC)_C$ migration. Therefore, processes involving migration of $(CC)_C$ have to be considered at the same or slightly higher temperatures as processes based on $(NC)_C$ migration. That means, it has to be investigated what happens when $(CC)_C$ split-interstitials meet $V_{Si}(N_C)_n$ complexes.

For $V_{Si}(N_C)_4$, we have already seen that it is energetically more opportune for the $(CC)_C$ to migrate to another C-site (leaving the total energy of the system unchanged) than to kick out one N-atom (increasing the total energy by ≈ 2.0 eV) of the complex.
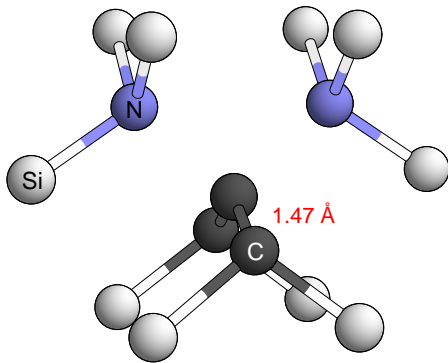
Figure 5.10: The $C_{Si}(N_C)_n$ complex.

For the $V_{Si}N_C$ pair, we have discussed the formation of a $C_{Si} N_C$ pair already in Section 5.1.5. Only 1.9 eV are needed for this recombination process that results in the 9.7 eV lower $C_{Si} N_C$ pair. The same mechanism can take place for the $V_{Si}(N_C)_2$ complex: with 2.4 eV the recombination to a $C_{Si}(N_C)_2$ complex can be activated, see Fig. 5.10. Here, 7.5 eV are gained by the recombination. A strong off-center relaxation of the antisite C_{Si} produces together with an inward relaxation of its two C-neighbors strong C-C double-bonds (sp^2-hybridization) that are with ≈ 1.47 Å shorter than in diamond (1.54 Å).

This relaxation effect that stabilizes the $C_{Si}(N_C)_2$ complex also causes the instability of the $C_{Si}(N_C)_3$ complex, where only one C-C bond would remain.

Actually, the electronic properties of the $C_{Si}N_C$ pair and the $C_{Si}(N_C)_2$ complex can explain the observed vanishing of the acceptor levels. In Table 5.3, the occupation levels of these two complexes, calculated within the LMTO method, are shown. The $C_{Si} N_C$ pair turns out to be a donor, similar to the isolated N_C, $C_{Si}(N_C)_2$ has been calculated to be a double donor. The $+/0$ level is for any polytype close to the conduction band minimum, similar as the donor level of the isolated N_C, which is even shallower. A trend to lower energies can be seen beginning with the donor level of N_C at E_{CB}-0.05 eV, $C_{Si} N_C$: E_{CB}-0.10 eV, $C_{Si}(N_C)_2$: E_{CB}-0.3...0.4 eV.

Thus, the acceptor levels of $V_{Si}(N_C)_n$ complexes can turn into donor levels by the incorporation of a C-atom due to recombination with a $(CC)_C$.

The $C_{Si}(N_C)_2$ complex can alternatively result from a $(NC)_C$ approaching a $V_{Si} N_C$ pair, as shown in Fig. 5.11. This kick-out process, in which the N-atom kicks out one of the C-ligands of the vacancy to the antisite position, requires 1.6 eV to be activated. The
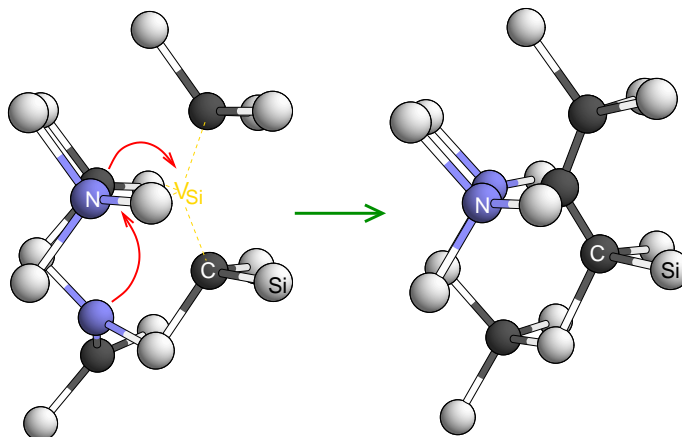
Figure 5.11: Creation of the $C_{Si}(N_C)_2$ complex when a $(NC)_C$ approaches a $V_{Si}N_C$ pair.

Table 5.3: Transition levels of $C_{Si}N_C$ and $C_{Si}(N_C)_2$ in the most common polytypes, calculated within LMTO.

Polytype	Defect	Transition	LMTO
3C	$C_{Si}N_C$	+/0	2.33 eV
4H	$C_{Si}N_C$	+/0	3.10 eV
6H	$C_{Si}N_C$	+/0	2.95 eV
3C	$C_{Si}(N_C)_2$	+/0	2.18 eV
3C	$C_{Si}(N_C)_2$	++/+	2.09 eV
4H	$C_{Si}(N_C)_2$	+/0	2.66 eV
4H	$C_{Si}(N_C)_2$	++/+	2.58 eV
6H	$C_{Si}(N_C)_2$	+/0	2.55 eV
6H	$C_{Si}(N_C)_2$	++/+	2.47 eV

energy gain of ≈ 9.3 eV affirms the stability of the complex.

5.3   Correlation of Activation Energies and Temperatures

So far, only activation energies have been discussed, but the experimentally accessible quantity is rather the temperature at which a defect anneals out[6]. To get an idea of how the calculated energies can be correlated with the observed annealing temperatures, we make an attempt to interpret our data with a simple model.

---

[6]To deduce activation energies from experimental data by an Arrhenius plot is often not very accurate and often technically difficult as it requires a large number of measurements in a wide temperature range. Especially for high temperatures, results depend on the annealing time.

5.3.1   Definition of an assignment

Assuming a Boltzmann distribution for the number of stable defects at a given temperature, the expression

$$T = \frac{\ln(\omega_D \cdot \tau)}{k_B}\Delta G_{\text{act}} \approx \frac{\ln(\omega_D \cdot \tau)}{k_B}E_{\text{act}} \qquad (5.2)$$

can be derived [43], allowing a direct comparison of the annealing temperature T with the calculated activation energy E_{act} for a migration mechanism of a defect. The Debye frequency $\omega_D \approx 1.6 \cdot 10^{13}s^{-1}$ is used as the attempt frequency for the jump, τ denotes the lifetime of the defect under these conditions. As only little is known about this quantity, we call a defect stable if it exists at least between one and one hundred seconds.

If there is a large contribution of the entropy at the saddle point compared to the minimum
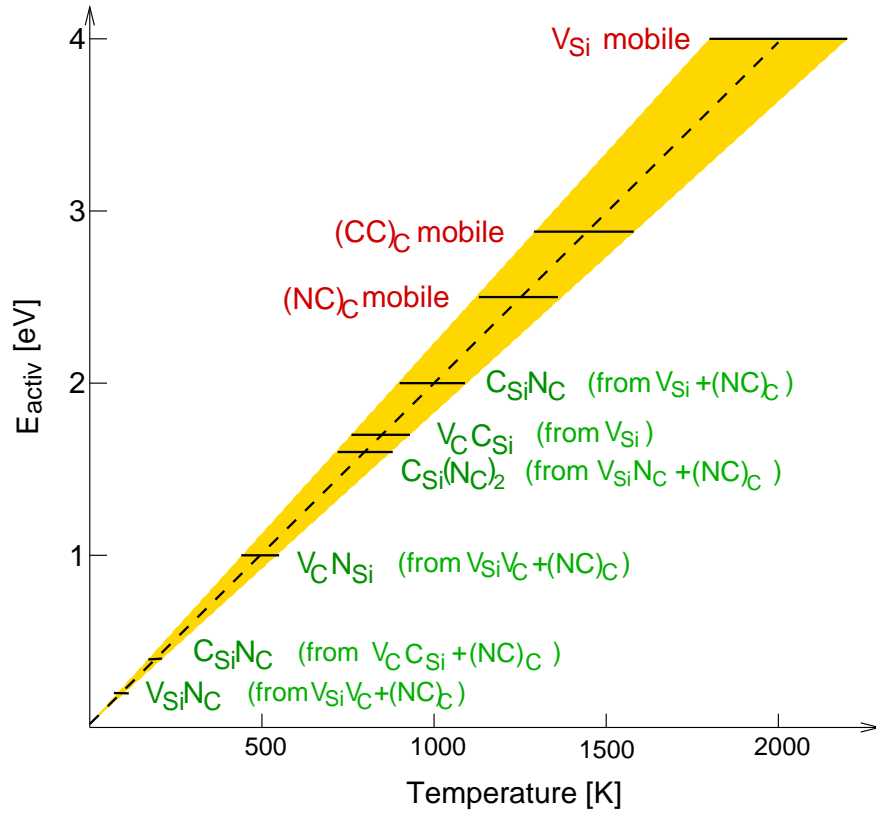
Figure 5.12: Correlation of the calculated activation energies with a temperature at which the annealing of the defect is observed. Due to uncertainties that are discussed in more detail in the text a range of temperatures is assigned to an activation energy instead of one specific value. Sublattice migration processes are denoted above the so obtained shaded region, other processes below.

energy structure, the free energy of migration $\Delta G_{\text{act}} = E_{\text{act}} - T \cdot \Delta S$ has to be used in Eq. 5.2 instead of E_{act}. Since this term is temperature dependent, the expression for T becomes

$$T = \frac{\ln(\omega_D \cdot \tau)}{k_B}\frac{1}{1 + \frac{\ln(\omega_D \cdot \tau)}{k_B}\Delta S} \cdot E_{\text{act}} \ . \qquad (5.3)$$

The change in entropy $\Delta S = S_{\text{saddlepoint}} - S_{\text{minimum}}$ is in most cases positive, so that the additional factor is <1, and the activation energy E_{act} has to be assigned to a lower temperature value.

While the entropical contributions lower the energy barriers and the correlated temperatures, other influences can increase the barriers and therewith the temperatures. As shown in Chapter 4 at the example of the migration of a silicon vacancy, the vicinity of other defects can increase or lower the migration barriers. Furthermore, different charge states can be the reason for an increase or decrease of the activation energies. Due to the inhomogeneity of a sample, the Fermi level may not be constant but locally varying to some extent. This may cause the coexistence of various charge states of one defect, implying a variation in the activation energies. Such effects cannot be known exactly and can therefore not be included in detail. Furthermore, the experimentally observed temperatures can vary about ≈ 100 K due to technological reasons. Another uncertainty lies within the calculated activation energies. A comparison of the activation energies calculated within SCC-DFTB with available ab initio data (sublattice migration of vacancies, formation of the $V_C C_{Si}$ -pair) [12] suggests deviations up to ≈ 0.5 eV. As the assignment is specialized to our results of the silicon vacancy, these deviations may, however, be much smaller. Nevertheless, within our calculations the obtained activation energies define at least upper limits, if in spite of intensive search the saddle point configuration with the lowest energy should have been missed. Since the main purpose is to give rather a qualitative overview than an exact assignment of T and E_{act}, these considerations lead us to the definition of a *range of temperatures* that is correlated with E_{act}. This has been done in Fig. 5.12, where the slope of the temperature–energy curve varies around an average value of 500 K $\sim$ 1 eV.

5.3.2 Correlation of the calculated values with experimental findings

The calculated values for the activation energies can now be compared with help of this assignment. Above the shaded area in Fig. 5.12, the sublattice migration processes are indicated. The silicon vacancy becomes mobile, i. e. long-range diffusion by sublattice migration starts, at a temperature of $1600°C$ [21], which agrees well with the calculated ≈ 4 eV for the activation energy: the above described assignment would suggest a corresponding temperature of 2000 ± 200 K.

The assignment of the activation energies for the mechanisms marked below the shaded area has been made under the assumption of non-equilibrium conditions. Directly after implantation, the defect- (especially vacancy-) concentrations are much higher than in thermal equilibrium, creating a thermodynamic driving force that tends to bring the system into equilibrium by certain annealing processes. We can, therefore, consider the presence of all the defects involved in the mechanisms, in order to compare the *activation energies*, only. Otherwise, in thermal equilibrium, the *formation energies* of e. g. vacancies for the vacancy assisted processes have to be considered, additionally (compare Sections 2.1.1 and 2.1.2).

The transformation of the silicon vacancy to the $C_{Si} V_C$ pair (activation energy ≈ 1.7 eV) has to be assigned to a temperature of ≈ 850 K, which also agrees quite well with the observed $\approx 750°C$ [10].

In agreement with experimental observations is, furthermore, the vanishing of divacancies below room temperature: the vanishing of the signal of the divacancy can be explained by a direct recombination with $(NC)_C$ split-interstitials, resulting in either $V_{Si} N_C$ - or $V_C N_{Si}$ -pairs, both processes are supposed to happen below 500 K. A direct recombination of $(NC)_C$ split-interstitials with $V_C C_{Si}$ pairs, which also may have been created directly by the implantation process, can be explained in this temperature range. Consequently, the

presence of both $C_{Si} N_C$ - and $V_{Si} N_C$ -pairs in as-implanted samples is conceivable.

The sublattice migration of $(NC)_C$ and $(CC)_C$ split-interstitials can accordingly be expected around 1250 K and 1450 K. Long-range diffusion and subsequent recombination of these split-interstitials with other defects is a possible explanation for the observed annealing stages at 1050°C and 1400°C.

The reduction of the free charge carrier compensation can be imagined like this: At lower temperatures, mainly recombination processes, the activation of N_C by close $(CC)_C$ and the migration of the created $(NC)_C$ will happen. Many nitrogen atoms will, however, get immobile again due to the recombination with carbon vacancies. A further mobilization requires new $(CC)_C$ to approach the N_C which further requires long-range diffusion of $(CC)_C$. If this is activated, further substitutionally built in nitrogen can be mobilized, and by the mechanisms described in Section 5.2.3. $C_{Si} N_C$ and $C_{Si} (N_C)_2$ complexes can be created from various defects and complexes created before. The electronic properties of these complexes can explain the recovery of the carrier concentration.

A competing process is, however, the formation of $V_{Si} (N_C)_n$ complexes which finally results in the inactive $V_{Si} (N_C)_4$ complex.

5.3.3   Entropy effects on nitrogen migration

The most important mechanisms, i. e. the creation of mobile nitrogen split-interstitials and the sublattice migration processes, have been investigated in view of the effects of vibrational entropy, as was done in case of vacancy migration and aggregation of antisite pairs in Chapter 4. The influence of the entropy on the sublattice migration of substitutional N_C might be rather strong, but the activation energy for this exchange process is much too high to be brought into a realistic order of magnitude by the entropical contribution.

Nevertheless, the entropical contribution to the activation energies of the creation process for nitrogen split-interstitials and the sublattice migration processes of the carbon- and nitrogen split-interstitials, has to be investigated. Our calculations show that the creation of $(NC)_C$ split-interstitials is facilitated by ≈ 0.3 eV at a temperature of 1800 K, while $(CC)_C$ is stabilized by ≈ 0.06 eV compared to the resulting $(NC)_C$. The change in energy along the migration path associated with this mechanism is shown in Fig. 5.13. The activation energy of the process does not change considerably, even at these elevated temperatures.

The same calculations were performed for the sublattice migration processes of the two split-interstitials. For the nitrogen split-interstitial $(NC)_C$, calculations yield a negligible contribution of $T \cdot \Delta S < 0.1$ eV for temperatures lower than 2000 K. The activation of $(CC)_C$ sublattice migration, though, is lowered by $T \cdot \Delta S \approx 0.7$ eV at a temperature of $T = 1800$ K. At a temperature of $T = 1300$ K, the barrier is lowered by ≈ 0.5 eV.

According to the stronger influence of vibrational entropy on the migration of carbon split-interstitials than on that of nitrogen split-interstitials, the activation of $(CC)_C$ and $(NC)_C$ sublattice migration has to be expected to happen at approximately the same temperature. Consequently, activation of nitrogen atoms that might e. g. have been trapped by carbon vacancies on their way through the lattice is perpetually possible by $(CC)_C$.

Furthermore, with the calculated entropies, we can now estimate the diffusivities of these split-interstitials and compare them to those of the vacancies. At $T = 1800$ K, the calculation of the diffusivities of the carbon and nitrogen split-interstitials yields $D((CC)_C)$
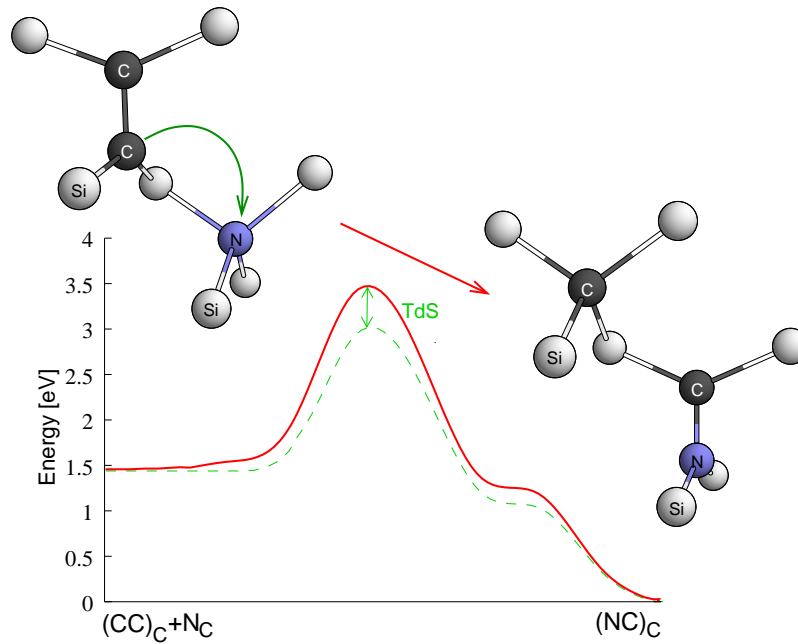
Figure 5.13: Influence of the vibrational entropy on the creation of $(NC)_C$ split-interstitials.

$= 2.67 \cdot 10^{-9}$ cm^2/s and D($(NC)_C$) $= 4.64 \cdot 10^{-10}$ cm^2/s. For the sublattice migration of carbon- and silicon-vacancies, we obtained values of D(V_C) $= 2.49 \cdot 10^{-15}$ cm^2/s and D(V_{Si}) $= 8.77 \cdot 10^{-14}$ cm^2/s, as already discussed in Chapter 4. The split-interstitial migration is in both cases by about four orders of magnitude faster than vacancy migration, so that the proposed mechanism is obviously very efficient.

5.4   Implantation with Phosphorus

An alternative to nitrogen implantation for the creation of n-type SiC-material is the implantation with phosphorus (P) ions. With the implantation of phosphorus, a higher electrical activation in the high concentration range ($> 10^{20}$ cm^{-3}) can be reached [31, 106], and a co-implantation of nitrogen and phosphorus was found to be advantageous. It is not yet clear on the atomic scale why this saturation behavior of the free carrier concentration is not (or possibly at higher concentrations) observed in P- or N-P co-implanted samples.

We have investigated migration mechanisms of the implanted phosphorus ions. For nitrogen, our calculations have shown a split-interstitial based mechanism to be very efficient. We therefore start with the investigation of a similar interstitial based mechanism for phosphorus. For this aim, we first have to investigate the stable interstitial structures of phosphorus atoms in the SiC lattice.
Among all the possible interstitial configurations, phosphorus – like nitrogen – turns out to prefer the split-interstitial position on the carbon site, $(PC)_C$. But also as split-interstitial on the silicon site, $(PSi)_{Si}$, the phosphorus atom can be built in, although $(PC)_C$ is favored about 0.83 eV over for $(PSi)_{Si}$. The geometries are similar to that of $(NC)_C$, but the phosphorus atom induces a large lattice distortion, so that relaxation moves the defect axis to a tilted position: in both structures, the P-atom is slightly moved out of the symmetry
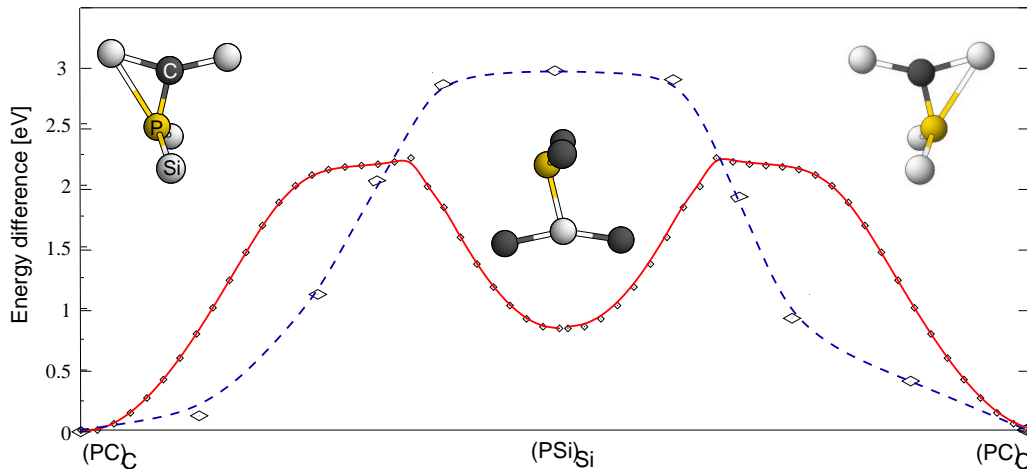
Figure 5.14: *Solid red line:* Migration of phosphorus split-interstitials using both sublattices: $(PC)_C \longrightarrow$ $(PSi)_{Si} \longrightarrow (PC)_C{}^{\text{nextsite}}$. *Dashed blue line:* Direct migration $(PC)_C \longrightarrow (PC)_C{}^{\text{nextsite}}$ requires a higher activation energy. The atomic structure in the center shows the geometry of $(PSi)_{Si}$, belonging to the two step process.

plane.

The tetrahedrally coordinated interstitial positions are – in contrast to the case of nitrogen – also stable, but about 7 eV higher than the split-interstitial configurations. Consequently, a split-interstitial based migration mechanism for phosphorus, similar to that proposed for nitrogen, can be expected to have the lowest energy of the possible interstitial based mechanisms.

A direct migration of $(PC)_C$ from one carbon site to the next leads over a symmetric interstitial structure, in which the phosphorus atom is bonded to both carbon atoms that are part of the initial and the final $(PC)_C$ structure, and the closest silicon atoms. The activation energy for this migration mechanism can be activated with 2.9 eV, compare the dashed line in Fig. 5.14.

Because of the result that $(PSi)_{Si}$ and $(PC)_C$ are both stable interstitial configurations, sublattice migration can also take place on both sublattices by first neighbor jumps with the P-atom alternating from $(PC)_C$ to $(PSi)_{Si}$, see the solid line in Fig. 5.14, and further on to the next carbon site. The jump from the carbon site to the silicon site $((PC)_C \longrightarrow (PSi)_{Si})$ can be activated with $\approx$2.2 eV, gaining 1.37 eV which are then needed to activate the jump from the silicon site to the next carbon site $((PSi)_{Si} \longrightarrow (PC)_C)$.

That means, sublattice migration of phosphorus can be activated at slightly lower cost than the analogous processes for nitrogen (2.5 eV) or carbon (2.9 eV). At elevated temperatures, both described mechanisms (with and without a change of the sublattice) have to be considered, thus we have found a very efficient diffusion mechanism for phosphorus.

Since the lattice is not at all perfect in the implanted region, the phosphorus atoms will not very long migrate through the lattice before meeting another defect. As in case of carbon split-interstitials in Chapter 3 and for nitrogen split-interstitials at the beginning of this chapter, we have investigated the recombination of phosphorus split-interstitials with vacancies on both sublattices for various dopant-vacancy distances.

In contrast to nitrogen, we have found that phosphorus fills up both silicon and carbon vacancies, and a process analogous to the kick-out mechanism described for nitrogen $(NC)_C$ interstitials close to a silicon vacancy could not be found. Instead, simple recombination processes lead to large energy gains, and an at the first view surprisingly long-range

influence of both kinds of vacancies has been found. Since the energetical difference between the two phosphorus split-interstitials is rather small, recombination processes of both $(PC)_C$ and $(PSi)_{Si}$ with V_C and V_{Si} have to be considered.

A $(PSi)_{Si}$ split-interstitial being second neighbor to a silicon vacancy has been found to be instable, as the phosphorus atom immediately and without any energy barrier moves to the vacant site, resulting in a P_{Si}. If instead a carbon vacancy is third neighbor to a $(PSi)_{Si}$, this structure has been calculated to be (meta)stable, but also in this case no energy barrier has to be overcome, before the P can recombine with the vacancy to P_C, gaining 10.3 eV.

For $(PC)_C$ split-interstitials, results are similar: a $(PC)_C$ as second neighbor to a V_C recombines with an activation energy of <0.3 eV and an energy gain of 8.7 eV to P_C. If a $(PC)_C$ has approached a silicon vacancy up to a third neighbor distance, they recombine spontaneously to P_{Si}. Even if $(PC)_C$ has approached a V_{Si} up to a fifth neighbor distance, only, the activation energy is still only $\approx$0.9 eV for recombination to P_{Si}. The energy gain due to this recombination amounts to 14.5 eV.

For a $V_C C_{Si}$ pair with the carbon vacancy in a second neighbor distance to a $(PC)_C$, an activation energy of <1.0 eV has been calculated for the recombination to the $P_C C_{Si}$ pair, even this process accompanied by a large energy gain of 12.5 eV.
From these results, we can conclude that phosphorus can, in contrast to nitrogen, be built in on both sublattices, as P_C or as P_{Si}.

The $P_C C_{Si}$ pair has also to be considered important as a donor complex. Though it is about 2.9 eV higher in energy than the stoichiometrically equivalent P_{Si}, its creation is likely by recombination of a phosphorus interstitial with a $V_C C_{Si}$ pair. Since the $V_{Si} Si_C$ pair is instable against recombination to V_C, an analogous mechanism for the creation of $P_{Si} Si_C$ does not exist. A creation starting from P_C by a costly exchange process is unlikely, in particular since the resulting $P_{Si} Si_C$ pair is by 2.2 eV higher in energy.

Recombination of phosphorus split-interstitials with divacancies can lead to phosphorus–vacancy pairs. These have already been observed by Veinger et al. [107] in 1986. For nitrogen, two stable positions in a vacancy were found, $N_C V_{Si}$ and $N_{Si} V_C$. For phosphorus, the situation is similar. Phosphorus prefers the silicon site of a divacancy by 1.1 eV over the carbon site. In the $P_C V_{Si}$ pair, the phosphorus is rather between the two vacancies than on the carbon site (the three P-Si bonds are elongated by 22 %), leading to a small barrier of 0.6 eV for the transformation into a $P_{Si} V_C$ pair. In the negative charge state, the $P_C V_{Si}$ pair gets stabilized. It is now only 0.5 eV higher in energy than the $P_{Si} V_C$ pair, and the energy barrier separating the two pairs increases to 0.9 eV. The $P_{Si} V_C$ pair is Jahn-Teller instable and slightly more stable if the defect axis is tilted a few percent and two of the silicon ligands of the vacancy relax to a larger distance between each other, resulting in C_{1h}-symmetry. The energy difference to the structure with C_{3v}-symmetry is, however, only $\approx$0.1 eV, so that at already rather low temperatures, the distortion will probably be averaged and the pair will be observed in C_{3v}-symmetry.

Its recombination behavior distinguishes phosphorus substantially from nitrogen. As it simply fills up vacancies, the formation of larger P aggregates, like e. g. a $V_{Si} (P_C)_4$ or a $V_C (P_{Si})_4$ complex, is implausible. Only the existence of larger vacancy clusters in the implanted region could explain the creation of such complexes, but a compensation of the free charge carriers as efficient as for nitrogen is not possible. If a P approaches a $P_{Si} V_C$ pair, it will fill up the vacancy, resulting in the $P_C P_{Si}$ pair. For nitrogen–vacancy pairs, the

formation of $N_{Si} N_C$ pairs was hindered by the kick-out process or the also more favorable formation of $C_{Si} (N_C)_2$ complexes. Furthermore, $N_{Si} N_C$ was calculated to have a slightly higher energy than its constituents. On the contrary, the pair of two phosphorus atoms has a binding energy of ≈ 2.4 eV over for isolated P_C and P_{Si}.

If phosphorus is used together with nitrogen in a co-doping procedure, there is, furthermore, the possibility of the formation of P-N pairs. The $P_C N_{Si}$ pair has been calculated to be by ≈ 5 eV higher in energy than the $P_{Si} N_C$ pair. Both pairs can result from a recombination with phosphorus split-interstitials with the respective nitrogen–vacancy pairs. Its lower energy and the more prevalent existence of the $V_{Si} N_C$ pair over for the inverse pair, supports the creation of $P_{Si} N_C$ pairs. The $P_{Si} N_C$ pair has C_{3v}-symmetry, and a binding energy of 2.5 eV compared to the isolated constituents P_{Si} and N_C. This binding energy and the large energy gains due to recombination of both nitrogen and phosphorus split-interstitials suggest that once created aggregates will not dissociate again.
On the other hand, according to the measurements of Laube et al. [106] the electronic behavior of the co-implanted sample is determined mainly by the phosphorus atoms, which rather suggests the formation of separate complexes of P and N with intrinsic defects in the first line.

The most important conclusions that can be drawn out of the results presented in this section are that phosphorus as a n-type dopant behaves completely different from nitrogen. A very efficient diffusion mechanism based on split-interstitial jumps has been found for long-range diffusion. The (for SiC) extremely low recombination barriers imply that at high defect concentrations, as can be expected directly after the implantation process (compare the discussion at the beginning of this chapter), the sublattice migration of phosphorus plays only a secondary role. Phosphorus split-interstitials will directly recombine with vacancies in a large radius of about five atomic distances already at low annealing temperatures. Once these processes have finished, lower defect concentrations demand higher annealing temperatures to activate sublattice migration in order to promote the phosphorus atoms to substitutional sites. These results indicate that doping with phosphorus has many advantages over for doping with nitrogen. Our finding that phosphorus does not tend to form inactive aggregates suggests, moreover, that the sequence of implantation steps with nitrogen and with phosphorus might make a difference. If already inactive nitrogen complexes have been formed, phosphorus will not change the situation, but if a large number of silicon vacancies are already filled up with phosphorus atoms, the kick-out process of nitrogen split-interstitials and thereby the formation of inactive $V_{Si} (N_C)_4$ complexes may be prohibited.

Chapter 6

Summary and Outlook

In this work, the selfconsistent charge density-functional based tight-binding method (SCC-DFTB) was used to investigate some selected problems of point defects and aggregates thereof in silicon carbide (SiC). Special importance was attached to mechanisms for the formation and annealing of defect complexes starting from such defects that are supposed to be created during ion implantation processes, both intrinsic and n-type dopants.

Antisites are not only among the intrinsic defects with the lowest formation energies but also among those which received the least attention in the literature. On the experimental side, this can be understood, since they are only hardly detectable by common methods. We could, however, show that there is a strong indication that the common D_I photoluminescence center is related to the antisite pair $C_{Si} Si_C$. Among a variety of possible mechanisms for the creation of an antisite pair, two vacancy assisted mechanisms have been calculated to be energetically most favorable.

The stability of larger aggregates of antisites, especially a completely inverted bilayer as the limit of two-dimensional antisite aggregation or the three-dimensional "onions" of antisites has been shown. For the creation of small onion-like aggregates centered around a silicon antisite, a mechanism based on the vacancy assisted mobility of isolated antisites has been described. A two-dimensional inversion of the lattice is, however, hindered by recombination barriers that are smaller than the barriers for creation or for the dissociation of the mediating vacancy from the complex, such that no complexes with more than two antisite pairs will be created.

This result stays unchanged if taking into account the entropical contributions to formation and activation energies. Although these contributions have been shown to be of non-negligible order of magnitude at the high temperatures needed for the activation of the discussed processes, recombination stays more likely for more than two pairs.
Thus, creation of a completely inverted bilayer which shows a promising quantum well behavior and offers many possibilities for the design of quantum devices, has to be done by a special epitaxial method during growth.

The annealing behavior of implanted nitrogen ions has been studied, resulting in a consistent model by which the experimentally observed saturation behavior of the free charge carrier concentration can be explained. With the help of carbon split-interstitials $(CC)_C$, nitrogen can be mobilized in form of nitrogen split-interstitials $(NC)_C$. Calculations based on the migration of these split-interstitials could confirm that nitrogen is preferably built in on the carbon site by recombination with carbon vacancies. Instead of similarly filling up

silicon vacancies, resulting in N_{Si}, the $(NC)_C$ perform rather a kick-out mechanism which leads to either $V_{Si} N_C$ or $C_{Si} N_C$ pairs. With $V_{Si} N_C$ as the first step to the formation of $V_{Si}(N_C)_4$ complexes which have been calculated to be electrically inactive, a very efficiently passivating atomistic model for the observed saturation has been found. The formation of $C_{Si} N_C$ and $C_{Si} (N_C)_2$ complexes can cause the recovery of charge carriers upon further implantation and annealing.

A similar, even more efficient, migration mechanism has been found for phosphorus as alternative n-type dopant. According to our investigations of recombination processes of phosphorus split-interstitials $(PC)_C$ and $(PSi)_{Si}$ with vacancies, phosphorus can as well be built in on silicon- as on carbon sites. Low activation energies and high energy gains go along with these recombination processes, an no aggregation to inactive complexes could be found, making P the preferred n-type dopant over for N.

In the near future, work on these matters has to be continued, especially in view of a possible identification of the EPR-signals of nitrogen- and phosphorus-related complexes with atomistic models – a field where there is today still much confusion in the literature. For this purpose, it could be shown during this work that a combination of several methods with different advantages is a successful approach to obtain experimentally relevant information about a topic.

Up to now, phosphorus and nitrogen have merely been treated separately. A more detailed investigation of how P influences the tendency of nitrogen to form inactive complexes during a real co-implantation process is required to find an efficient co-implantation and annealing procedure for the creation of n-type material with high concentrations of free charge carriers.

Furthermore, it has to be investigated both experimentally and theoretically, how the formation of large antisite aggregates can be achieved. Some first calculations have shown a promising behavior of such structures, especially the two-dimensional inverted bilayer, as quantum well/wall structures with a large tunneling probability. If one could succeed in deterministically growing silicon and carbon monolayers hetero- as well as homoepitaxially, a large variety of quantum devices could be designed for special purposes.

Appendix A

Formation Energies

To determine the relative stability of defects, the formation energy is calculated. It depends on the environmental conditions, i. e. the concentrations of all involved materials, the temperature and the pressure. The temperature dependence does not only enter the expression for the Gibbs free enthalpy with the term $-TS$ (see chapter 2) but is also implicitly included in the formation energy via the chemical potential. This dependence is, though, only significant, if e. g. equilibrium of a solid with a gaseous phase is investigated (compare the considerations of growth and oxidation of SiC surfaces in Ref. [41]). In the processes discussed in this work, the implicit temperature dependence of the chemical potentials is negligible as is the pressure dependence.

With the total energies E_{tot} obtained from the supercell calculations, the formation energy for any defect in SiC has the form

$$E_{\text{form}} = E_{\text{tot}} - n_{\text{Si}}\mu_{\text{Si}} - n_{\text{C}}\mu_{\text{C}} - \sum_i n_{\text{i}}\mu_{\text{i}} \ . \tag{A.1}$$

Here, n_{Si} and n_{C} denote the concentrations of silicon- and carbon–atoms, n_{i} the concentrations of all impurities i in the crystal. With μ_{Si}, μ_{C} and μ_{i}, the chemical potentials of silicon, carbon and the impurities are taken into account.

In thermal equilibrium with the SiC crystal, the chemical potentials of silicon μ_{Si} and carbon μ_{C} are connected by the relation

$$\mu_{\text{Si}} + \mu_{\text{C}} = \mu_{\text{SiC}}^{\text{bulk}} \ , \tag{A.2}$$

with help of which one of the chemical potentials can be eliminated from the expression for the formation energy.

With some further definitions, such as

$$\Delta\mu_{\text{Si}} = \mu_{\text{Si}} - \mu_{\text{Si}}^{bulk} \qquad \text{and} \qquad \Delta\mu_{\text{C}} = \mu_{\text{C}} - \mu_{\text{C}}^{bulk} \ , \tag{A.3}$$

denoting the deviation of the actual chemical potentials of silicon and carbon in the SiC-crystal from their values in the most stable phase of the silicon- and the carbon-crystal, and the formation enthalpy of SiC

$$\Delta H_{\text{f}}^{\text{SiC}} = \mu_{\text{SiC}}^{\text{bulk}} - \mu_{\text{Si}}^{bulk} - \mu_{\text{C}}^{bulk} \ , \tag{A.4}$$

it follows that

$$\Delta\mu_{\text{Si}} + \Delta\mu_{\text{C}} = \Delta H_{\text{f}}^{\text{SiC}} \ . \tag{A.5}$$

For intrinsic defects, Eq. A.1 can now be rewritten by substituting the chemical potential of carbon μ_C:

$$
\begin{aligned}
E_{\text{form}} &= E_{\text{tot}} - n_{\text{Si}}\mu_{\text{Si}} - n_C\mu_C \\
&= E_{\text{tot}} - n_{\text{Si}}\mu_{\text{Si}} - n_C \cdot (\mu_{\text{SiC}}^{\text{bulk}} - \mu_{\text{Si}}) \\
&= E_{\text{tot}} - (n_{\text{Si}} - n_C) \cdot \mu_{\text{Si}} - n_C\mu_{\text{SiC}}^{\text{bulk}} \\
&= E_{\text{tot}} - (n_{\text{Si}} - n_C) \cdot (\Delta\mu_{\text{Si}} + \mu_{\text{Si}}^{\text{bulk}}) - n_C\mu_{\text{SiC}}^{\text{bulk}} \ .
\end{aligned}
\tag{A.6}
$$

Substituting instead the silicon chemical potential μ_{Si} leads to the equation:

$$
E_{\text{form}} = E_{\text{tot}} - (n_C - n_{\text{Si}}) \cdot (\Delta\mu_C + \mu_C^{\text{bulk}}) - n_{\text{Si}}\mu_{\text{SiC}}^{\text{bulk}} \ .
\tag{A.7}
$$

The addition of these two equations leads to a symmetric form of the expression:

$$
\begin{aligned}
E_{\text{form}} &= E_{\text{tot}} - \frac{1}{2}(n_{\text{Si}} - n_C)\left[\cdot\Delta\mu_{\text{Si}} + \mu_{\text{Si}}^{\text{bulk}} - \Delta\mu_C - \mu_C^{\text{bulk}}\right] \\
&\quad - \frac{1}{2}(n_{\text{Si}} + n_C) \cdot \mu_{\text{SiC}}^{\text{bulk}} \ .
\end{aligned}
\tag{A.8}
$$

Using Eq. A.4, a new $\Delta\mu$ can be defined as

$$
\Delta\mu = \Delta\mu_{\text{Si}} - \frac{1}{2}\Delta H_f^{\text{SiC}} = -\left(\Delta\mu_C - \frac{1}{2}\Delta H_f^{\text{SiC}}\right) \ ,
\tag{A.9}
$$

leading to the relation

$$
\Delta\mu_{\text{Si}} - \Delta\mu_C = 2\Delta\mu \ .
\tag{A.10}
$$

Substituting this difference in the second term of Eq. A.9 and reordering some terms leads to the final expression for the formation energy:

$$
\begin{aligned}
E_{\text{form}} &= E_{\text{tot}} - \frac{1}{2}(n_{\text{Si}} - n_C)\left(\mu_{\text{Si}}^{\text{bulk}} - \mu_C^{\text{bulk}}\right) - \frac{1}{2}(n_{\text{Si}} + n_C)\mu_{\text{SiC}}^{\text{bulk}} \\
&\quad - (n_{\text{Si}} - n_C)\Delta\mu \ .
\end{aligned}
\tag{A.11}
$$

Only the last term contains the energy's dependence on the environmental conditions, expressed in form of the chemical potentials of the silicon- and carbon–atoms, united in the variable $\Delta\mu$. All other terms are independent from the environment and just correct for the different numbers of atoms of either sort in the supercells used for the calculation of different defects.

Varying $\Delta\mu$ means, thus, varying the C/Si ratio, as can experimentally be done during growth. During growth the conditions can range from carbon–rich, i. e. $\mu_C = \mu_C^{\text{bulk}}$, to silicon–rich, i. e. $\mu_{\text{Si}} = \mu_{\text{Si}}^{\text{bulk}}$. If stepping across these limits the silicon carbide phase is no longer the most stable phase. If for example the silicon chemical potential becomes higher than that of the silicon bulk, $\mu_{\text{Si}} \geq \mu_{\text{Si}}^{\text{bulk}}$, silicon will grow instead of SiC.

Using the definition of $\Delta\mu_{\text{Si}}$ and $\Delta\mu_C$, it follows from Eq. A.9 that $\Delta\mu$ can be varied in the range

$$
\frac{1}{2}\Delta H_f^{\text{SiC}} \leq \Delta\mu \leq -\frac{1}{2}\Delta H_f^{\text{SiC}} \ .
\tag{A.12}
$$

If the crystal contains any impurities i, the formation energy has the same form as in Eq. A.12, but the term $\sum_i n_i\mu_i$, as explained in Eq. A.1, has to be added. The chemical potential and the range in which it can be varied has to be considered in each special case.

Appendix B

Calculation of the Gibbs Free Enthalpy

In section 2.6, the calculation of the Gibbs free energy based on the calculation of vibrational spectra is discussed. Based on the Einstein model of harmonic oscillators, the vibrational part of the internal energy

$$U_{\text{vib}} = \sum_{i=1}^{3N} \left\{ \frac{\hbar\omega_i}{exp(\hbar\omega_i/k_B T) - 1} + \frac{1}{2}\hbar\omega_i \right\} \tag{B.1}$$

was derived. From Eq. B.1, we can, following simple thermodynamics, derive an expression for the vibrational entropy S_{vib}. Assuming constant volume V and number of particles N, we have

$$\left(\frac{\partial S}{\partial U} \right)_{\text{V,N}} = \frac{1}{\left(\frac{\partial U}{\partial S} \right)_{\text{V,N}}} = \frac{1}{T(S(U,V,N),V,N)} = \frac{1}{T(U,V,N)} \tag{B.2}$$

By solving Eq. B.1 for $1/T$ we obtain

$$\frac{1}{T} = \sum_{i=1}^{3N} \frac{k_B}{\hbar\omega_i} \cdot \ln\left(\frac{U_i + \frac{1}{2}\hbar\omega_i}{U_i - \frac{1}{2}\hbar\omega_i} \right) = \left(\frac{\partial S}{\partial U} \right) = \sum_{i=1}^{3N} \left(\frac{\partial S_i}{\partial U_i} \right) \tag{B.3}$$

Integration of the expressions for the S_i over U_i' ranging from the zero point energy $U_i = \hbar\omega_i/2$ to U_i yields

$$S_i = \frac{k_B}{\hbar\omega_i} \left[(U_i + \frac{1}{2}\hbar\omega_i) \cdot \ln(U_i + \frac{1}{2}\hbar\omega_i) - (U_i - \frac{1}{2}\hbar\omega_i) \cdot \ln(U_i - \frac{1}{2}\hbar\omega_i) - \hbar\omega_i \cdot \ln(\hbar\omega_i) \right] , \tag{B.4}$$

and finally substituting U_{vib} from Eq. B.1 and summation over i results in

$$S_{\text{vib}} = k_B \sum_{i=1}^{3N} \left\{ \frac{\hbar\omega_i}{k_B T} \left[exp\left(\frac{\hbar\omega_i}{k_B T} \right) - 1 \right]^{-1} - \ln\left[1 - exp\left(-\frac{\hbar\omega_i}{k_B T} \right) \right] \right\} . \tag{B.5}$$

For high temperatures T, the term $\hbar\omega_i/k_B T$ becomes small, and a linear approximation can be made for the exponential function. This results in the high temperature expressions

$$U_{\text{vib}} = \sum_{i=1}^{3N} \left\{ k_B T + \frac{1}{2}\hbar\omega_i \right\} \tag{B.6}$$

for the internal energy U_{vib} and

$$S_{\text{vib}} = k_B \sum_{i=1}^{3N} \left\{ 1 - \ln\left(\frac{\hbar\omega_i}{k_B T} \right) \right\} \tag{B.7}$$

for the vibrational entropy. The formation entropy of a defect, $S_{\text{vib}}^{\text{defect}} - S_{\text{vib}}^{\text{ideal\,bulk}}$, becomes in this limit temperature independent.

For the application to defect formation and migration in SiC, this high temperature approximation can, though, not be used, since it first becomes valid for temperatures clearly above the Debye temperature of the material. The temperatures used in common annealing processes, and thus the temperature range connected to most of the processes discussed in this work, are, however, close to or below the Debye temperature of SiC[1]. Therefore, the exact expressions of Equations B.1 and B.5 have been used throughout the work.

As the phonon spectrum should be rather continuous, a broadening of the calculated frequencies may be senseful. Then, the summation over the $3N$ frequencies turns to an integration. We can rewrite Eq. B.1 as

$$U_{\text{vib}} = \int_0^{\omega_{\max}} g(\omega) \left\{ \frac{\hbar\omega}{exp(\hbar\omega/k_B T) - 1} + \frac{1}{2}\hbar\omega \right\} d\omega \tag{B.8}$$

with the partition function

$$g(\omega) = \sum_{i=1}^{3N} \delta(\omega - \omega_i) \ . \tag{B.9}$$

The δ-function in this expression can be substituted by a Gauß-broadening, which smoothens it and achieves a better numerical stability:

$$g(\omega) = \sum_{i=1}^{3N} \frac{1}{\sigma\sqrt{2\pi}} \cdot e^{-\frac{(\omega-\omega_i)^2}{2\sigma^2}} \ . \tag{B.10}$$

The summation in Eq. B.5 can then be transformed into an integration similarly. In the case of the applications discussed in this work, a sensitive broadening between 10 cm^{-1} and 20 cm^{-1} did, though, not change the results for the entropy or the internal energy notably.

---

[1] Literature values range from 1200°C to 1600°C [70]

Appendix C

Basic Properties of Strain Fields

In chapter 2 some formulas derived within elasticity theory are needed to calculate the corrections to the formation entropy. Only these elementary equations are sketched in the following.

The strained material can be described by a displacement field

$$\vec{u}(\vec{r}) = \vec{r}\,' - \vec{r} \,, \tag{C.1}$$

where $\vec{r}$ are the positions in the unstrained, $\vec{r}\,'$ in the strained lattice. The distance $\vec{a}$ of two points in the material changes accordingly by

$$d\vec{a} = \vec{u}(\vec{r} + \vec{a}) - \vec{u}(\vec{r}) \,, \tag{C.2}$$

which can in components be linearly expanded to

$$
\begin{aligned}
da_i &= \sum_j \left(\frac{\partial u_i}{\partial x_j} \right) a_j \\
&= \sum_j \left[\frac{1}{2} \left(\frac{\partial u_i}{\partial x_j} + \frac{\partial u_j}{\partial x_i} \right) + \frac{1}{2} \left(\frac{\partial u_i}{\partial x_j} - \frac{\partial u_j}{\partial x_i} \right) \right] \\
&= \sum_j (\varepsilon_{ij} + \pi_{ij}) \,.
\end{aligned} \tag{C.3}
$$

The π_{ij} only cause a rotation, no displacement, while the ε_{ij} are the components of the symmetrical strain tensor ε, which can be shown to have six independent components [77]. Considering the material to be built up of small cubes, the diagonal elements of ε represent the length changes of the edges while twice the off diagonal elements represent the change in angle.

The volume change is, therefore, characterized by the dilatation

$$\delta = \frac{\delta V}{V} = \varepsilon_{11} + \varepsilon_{22} + \varepsilon_{33} \,. \tag{C.4}$$

With Hooke's Law the stress tensor σ is obtained from ε as

$$\sigma = c \cdot \varepsilon \quad \text{with} \quad \sigma_{ij} = \sigma_{ji}$$

$$
\begin{pmatrix} \sigma_{11} \\ \sigma_{22} \\ \sigma_{33} \\ \sigma_{23} \\ \sigma_{31} \\ \sigma_{12} \end{pmatrix}
=
\begin{pmatrix}
c_{11} & c_{12} & c_{12} & 0 & 0 & 0 \\
c_{12} & c_{11} & c_{12} & 0 & 0 & 0 \\
c_{12} & c_{12} & c_{11} & 0 & 0 & 0 \\
0 & 0 & 0 & c_{44} & 0 & 0 \\
0 & 0 & 0 & 0 & c_{44} & 0 \\
0 & 0 & 0 & 0 & 0 & c_{44}
\end{pmatrix}
\cdot
\begin{pmatrix} \varepsilon_{11} \\ \varepsilon_{22} \\ \varepsilon_{33} \\ 2\varepsilon_{23} \\ 2\varepsilon_{31} \\ 2\varepsilon_{12} \end{pmatrix}
\tag{C.5}
$$

The bulk modulus K and the shear modulus γ can be obtained from the components of $\mathbf{c}$ as

$$K = \frac{1}{3}(c_{11} + 2c_{12}) \qquad \text{and} \qquad \gamma = c_{44} \tag{C.6}$$

For an isotropic solid, the relation

$$c_{44} = \frac{1}{2}(c_{11} - c_{12}) \tag{C.7}$$

holds, furthermore. The Lamé-constants λ and μ used in chapter 2 relate to the components of c like

$$c_{11} = \lambda + 2\mu \; , \qquad c_{12} = \lambda \; , \qquad c_{44} = \mu \; , \tag{C.8}$$

so that the elements of the stress tensor σ can be written as

$$\sigma_{ij} = 2\mu\,\varepsilon_{ij} + \lambda\,\delta\,\delta_{ij} \tag{C.9}$$

with the dilatation δ and the Kronecker delta function δ_{ij}.

A point defect inhomogeneously strains the crystal lattice. The stress σ_{ij} changes over a distance $\delta x_j = a$ (the edge of a small cube) by $a(\partial\sigma_{ij}/\partial x_j)$, and, as in equilibrium the total forces must vanish, we get

$$\sum_i \frac{\partial\sigma_{ij}}{\partial x_j} = 0 \; . \tag{C.10}$$

Expressing ε_{ij} in Eq. C.9 by the derivatives of the displacement field $\vec{u}(\vec{r})$ as defined by Eqns. C.3 yields

$$\mu\nabla^2\vec{u} + (\lambda + \mu)\nabla(\nabla \cdot \vec{u}) = 0 \tag{C.11}$$

or, since $\nabla \times (\nabla \times \vec{a}) \equiv \nabla(\nabla\vec{a}) - \nabla^2\vec{a}$ holds for any vector $\vec{a}$,

$$(\lambda + 2\mu)\,\nabla(\nabla \cdot \vec{u}) - \mu\,\nabla \times (\nabla \times \vec{u}) \; . \tag{C.12}$$

Operating with $\nabla\cdot$ on this equation yields (as $\nabla \cdot (\nabla \times \vec{a}) \equiv 0$)

$$\nabla^2(\nabla \cdot \vec{u}) = \nabla^2\delta = 0 \; . \tag{C.13}$$

Under the assumptions of isotropy the dilatation δ has, thus, to solve a Laplace equation, for which the boundary conditions are given by the special problem, as e. g. a force free surface of the surrounding material.

Appendix D

Summary: Activation Energies

To give a better overview and facilitate the comparison, the values calculated for the activation energies and migration energies that are discussed in Chapters 3, 4 and 5 are summarized in Table D.1 for processes of intrinsic defects only and in Table D.2 for those processes that involve also nitrogen or phosphorus.

Values are sorted, so that the energy gain listed in the last column is always positive. The recombination barriers, describing the inverse processes, can be obtained by adding the energy barriers in the second and the energy gain in the fourth column.

Table D.1: Summary of the calculated activation energies for intrinsic defects.

Initial structure	Energy barrier [eV]	Final structure	Energy gain [eV]
C_{Si}	11.7	C_{Si} next site	–
Si_C	11.6	Si_C next site	–
Si-C	10.5	$C_{Si} Si_C$	4.5
V_C	5.8	$C_{Si} Si_C + V_C$	3.5
$V_C C_{Si}$	4.7	$C_{Si} Si_C + V_C C_{Si}$	2.0
$Si_C + V_C$	4.1	$V_C + Si_C$	–
$C_{Si} + V_{Si}$	2.0	$V_{Si} + C_{Si}$	–
V_C	4.7	V_C next site	–
V_{Si}	4.1	V_{Si} next site	–
V_{Si}	1.7	$V_C C_{Si}$	1.8
$(CC)_C$	2.9	$(CC)_C$ next site	–
$(CC)_C$	0.6	$(CC)_C$ turned	–

In cases where varying activation energies were obtained for the different lattice sites or orientations of the pair defects, only an average value has been given in the table. Sometimes the nomenclature does not clearly describe the mechanism. In that case, the reader is referred to the respective chapters for more information.

Table D.2: Summary of the calculated activation energies for processes that involve dopant atoms.

Initial structure	Energy barrier [eV]	Final structure	Energy gain [eV]
$V_{Si} + N_C$	3.5	$V_{Si} N_C$	2.0
$(CC)_C + N_C$	2.0	$(NC)_C$	1.4
$(CC)_C + C_{Si} N_C$	1.8	$C_{Si} (NC)_C$	1.9
$(CC)_C + V_{Si} N_C$	1.9	$C_{Si} N_C$	9.7
$(CC)_C + V_{Si} (N_C)_2$	2.4	$C_{Si} (N_C)_2$	7.5
$(NC)_C$	2.5	$(NC)_C$ $^{\text{next site}}$	–
$(NC)_C$	0.8	$(NC)_C$ $^{\text{turned}}$	–
$(NC)_C + V_{Si}$	2.0	$C_{Si} N_C$	10.6
$(NC)_C + V_C C_{Si}$	0.3	$C_{Si} N_C$	8.8
$(NC)_C + V_{Si} N_C$	1.6	$C_{Si} (N_C)_2$	9.3
$(NC)_C + V_{Si}$	2.9	$V_{Si} N_C + (CC)_C$	1.8
$(NC)_C + V_{Si} (N_C)_3$	2.9	$V_{Si} (N_C)_4 + (CC)_C$	2.0
$(NC)_C + V_C V_{Si}$	0.2	$V_{Si} N_C$	7.4
$(NC)_C + V_{Si} V_C$	1.0	$V_C N_{Si}$	8.0
$(NC)_C + V_C V_{Si} (N_C)_3$	1.0	$V_{Si} (N_C)_4$	8.9
$V_C N_{Si}$	2.5	$V_{Si} N_C$	0.8
$(PC)_C$	2.9	$(PC)_C$	–
$(PSi)_{Si}$	1.4	$(PC)_C$	0.8
$(PC)_C + V_C$ $^{\text{2nd neighbor}}$	<0.3	P_C	8.7
$(PC)_C + V_{Si}$ $^{\text{5nd neighbor}}$	<0.9	P_{Si}	14.5
$(PC)_C + V_C C_{Si}$ $^{\text{2nd neighbor}}$	<1.0	$P_C C_{Si}$	12.5

Bibliography

[1] BeyArs GmbH, St. Gilgen, Austria, *http://www.beyars.com*.

[2] Infineon Technologies AG, München, *http://www.infineon.com*, "thinQ!™ SiC Schottky Diodes".

[3] T. Wimbauer, B. Meyer, A. Hofstaetter, A. Scharmann, and H. Overhof, Phys. Rev. B 56, 7384 (1997).

[4] A. Zywietz, J. Furthmüller, and F. Bechstedt, Phys. Status Solidi B 210, 13 (1998).

[5] A. Zywietz, J. Furthmüller, and F. Bechstedt, Phys. Rev. B **59**, 15 166 (1999).

[6] A. Zywietz, J. Furthmüller, and F. Bechstedt, Phys. Rev. B **62** (11), 6854 (2000).

[7] L. Torpo, R. M. Nieminen, K. E. Laasonen, and S. Pöykkö, Appl. Phys. Lett. 74, 221 (1999).

[8] P. Deák, J. Miró, A. Gali, L. Udvardi, H. Overhof, N. T. Son, App. Phys. Lett. 75, 2103-2105 (1999).

[9] E. Rauls, Th. Lingner, Z. Hajnal, S. Greulich–Weber, Th. Frauenheim, J.-M. Spaeth, phys. stat. sol. (b), 217/2 (2000), p. R1.

[10] Th. Lingner, U. Gerstmann, E. Rauls, S. Greulich-Weber, J.-M. Spaeth, H. Overhof, and Th. Frauenheim, Phys. Rev. B, **64**, 245212, 2001.

[11] L. Torpo, T.E.M.Staab, and R. Nieminen, Phys. Rev. B **65**, 085202 (2002).

[12] A. Mattausch, M. Bockstedte and O. Pankratov, Mat. Sci. Forum **353-356**, 323 (2001).

[13] M. Bockstedte, M. Heid, A. Mattausch, and O. Pankratov, Mater. Sci. Forum 389-393, ???(Tsukuba) (2002).

[14] H. Itoh, A. Uedono, T. Ohshima, Y. Aoki, M. Yoshikawa, I. Nashiyama, S. Tanigawa, H. Okumura, and S. Yoshida, Appl. Phys. A **65**, 315 (1997).

[15] Recently it has been realized that the assignment of the early EPR centers to vacancies was in error.

[16] B. Aradi, A. Gali, P. Deák, J. E. Lowther, N. T. Son, E. Janzén, and W. J. Choyke, Phys. Rev. B, 6 3, 245202 (2001).

[17] A. Kawasuso, H. Itoh, and S. Okada, J. Appl. Phys. **80**, 5639 (1996).

[18] N. T. Son, E. Sörman, W. M. Chen, C. Hallin, O. Kordina, B. Monemar, and E. Janzén, Phys. Rev. B **55** (5), 2863 (1997).

[19] E. Sörman, N. T. Son, W. M. Chen, O. Kordina, C. Hallin, and E. Janzén, Phys. Rev. B **61** (4), 2613 (2000).

[20] M. Wagner, B. Magnusson, W. M. Chen, E. Janzén, E. Sörman, C. Hallin, and J. L. Lindström, Phys. Rev. B **62** (24), 16555 (2000).

[21] N. T. Son, Mat Sci. Forum, Proceedings of ECSCRM2002, in print.

[22] C. Wang, J. Bernholc, R. F. Davis, Phys. Rev. B 38, 12752 (1988).

[23] L. Torpo, S. Pöykkö, R. M. Nieminen, Phys. Rev. B **57** (1998), p. 6243.

[24] L. Torpo, R. M. Nieminen, Mat. Sci. Eng. B **61-62** (1999), p. 593.

[25] E. Rauls, Z. Hajnal, A. Gali, P. Deák, and Th. Frauenheim, Mat. Sci. Forum, Vol. 353-356, 435-439 (2001).

[26] F. Gao, W. J. Weber, W. Jian, Phys. Rev. B **63**, 214106 (2001).

[27] N. T. Son, P. N. Hai, E. Janzén, Phys. Rev. Lett. 87, 045502 (2001).

[28] L. Patrick and W. J. Choyke, Phys. Rev. B **5**, 3252 (1972).

[29] T.A.G. Eberlein, C.J. Fall, R. Jones, P.R. Briddon, and S. Öberg, Phys. Rev. B **65**, 184108 (2002).

[30] A. Gali, P. Deák, E. Rauls, N. T. Son, I. G. Ivanov, F. H. C. Carlsson, E.Janzén, and W. J. Choyke, Phys. Rev. B, **67**, 155203 (2003).

[31] M. Laube, F. Schmid, G. Pensl, and G. Wagner, Mat. Sci. Forum **389-393**, 791 (2001).

[32] D. Åberg, A. Hallén, P. Pellegrino, and B. G. Svensson, Appl. Phys. Lett. **78**, 2908 (2001).

[33] D. Åberg, A. Hallén, P. Pellegrino, and B. G. Svensson, Appl. Surf. Sci. **184**, 263 (2001).

[34] M.Bockstedte, A. Kley, J. Neugebauer and M. Scheffler, Comput. Phys. Commun. **107** (1997), p. 187.

[35] R. Jones, Philos. Trans. R. Soc. Ser. A **341**, 351 (1992).

[36] O. Gunnarsson, O. Jepsen, and O. K. Andersen, Phys. Rev. B **27**, 7144 (1983).

[37] U. Gerstmann, H. Overhof, Physica B **308**, 561 (2001).

[38] G. L. Harris (Hrsg.), *Properties of Silicon Carbide*, EMIS Datareview Series 13, IN-SPEC (1995).

[39] E. Rauls, R. Gutierrez, J. Elsner, and Th. Frauenheim, Sol. State Comm. **111**, 459 (1999).

[40] E. Rauls, Z. Hajnal, A. Gali, P. Deák, and Th. Frauenheim, Mat. Sci. Forum, Vol. 353-356, 435-439 (2000).

[41] E. Rauls, Diplomarbeit, Universität Paderborn, (1999).

[42] E. Rauls, Z. Hajnal, P. Deák, and Th. Frauenheim, Phys. Rev. B **64**, 245323 (2001).

[43] M. Lannoo and J. C. Bourgoin, Solid State Commun. **32**, 913 (1979).

[44] D. Porezag, Th. Frauenheim, T. Köhler, G. Seifert, R. Kaschner, Phys. Rev. B **52**, (1995) p. 11837.

[45] Th. Frauenheim, G. Seifert, M. Elstner, Z. Hajnal, G. Jungnickel, D. Porezag, S. Suhai, R. Scholz, phys. stat. sol. (b), **217**, 41 (2000).

[46] M. Sternberg, Dissertation, Universität Paderborn, (2001).

[47] M. Elstner, D. Porezag, G. Jungnickel, J. Elsner, M. Haugk, Th. Frauenheim, S. Suhai, G. Seifert, Phys. Rev. B **58** (1998) p. 7260.

[48] K. Ohno, K. Esfarjani, and Y. Kawazoe, *Computational Materials Science*, Springer Verlag, Berlin (1999).

[49] P. Hohenberg and W. Kohn, Phys. Rev. **136**, B864 (1965).

[50] W. Kohn and L.J. Sham, Phys. Rev. **140**, A1133 (1965).

[51] D.M. Ceperley and B. J. Alder, Phys. Rev. Lett. **45**, 566 (1980).

[52] J.P. Perdew and Y. Wang, Phys. Rev. B **33**, 8800 (1986).

[53] J.P. Perdew, K. Burke, and M. Enzerhof, Phys. Rev. Lett. **77**, 3865 (1996).

[54] F. Beeler, O.K.Andersen, and M. Scheffler, Phys. Rev. B **41**, 1603 (1990).

[55] G.A. Baraff, E.O.Kane, and M. Schlüter, Phys. Rev. B **21**, 5662 (1980).

[56] F. Jensen, *Introduction to Computatinal Chemistry*, John Wiley & Sons, Chichester, New York (2001).

[57] W.M.C. Foulkes and R. Haydock, Phys. Rev. B **39**, 12520 (1989).

[58] J.C. Slater and G.F. Koster, Phys. Rev. B **94**, 1498 (1954).

[59] H. Eschrig, *The Optimized LCAO Method and Electronic Structure of Extended Systems*, Akademie-Verlag, Berlin (1988).

[60] J. Elsner, Dissertation, Universität Paderborn, (1999).

[61] U. Gerstmann, E. Rauls, H. Overhof, and Th. Frauenheim, Phys. Rev. B **65**, 195201 (2002).

[62] U. Gerstmann, E. Rauls, Th. Frauenheim, and H. Overhof, Proceedings of ECSCRM2002, Physica B, in print, (Oct. 2002).

[63] U. Gerstmann, E. Rauls, Th. Frauenheim, and H. Overhof, Phys. Rev. B **67**, in press, (2003).

[64] M. J. Puska, S. Pöykkö, M. Pesola, and R. M. Nieminen, Phys. Rev. B **58**, 1318 (1998).

[65] H. J. Monkhorst and J. K. Pack, Phys. Rev. B **13**, 5188 (1976).

[66] M. Kaukonen, T. Frauenheim et al., Phys. Rev. B **57**, 9965 (1998).

[67] G. T. Barkema and N. Mousseau, Phys. Rev. Lett. **77**, (1996) p. 4358.

[68] A. Gali, private communication (2003).

[69] A. Mattausch, private communication (2003).

[70] Landolt-Börnstein, New Series III/41 A1α, 2001 and references therein.

[71] Ch. Kittel *Physik der Wärme*, R. Oldenbourg Verlag, (1973).

[72] H. Kuchling, Taschenbuch der Physik, (1986).

[73] R.D. Hatcher, R. Zeller, and P.H. Dederichs, Phys. Rev. B **19**, 5083 (1979).

[74] J. R. Fernández, A.M. Monti, and R. C. Pasianot, Phys. Stat. Sol.(b) **219**, 245 (2000).

[75] Y. Mishin, M.R. Sorensen, and A. F. Voter, Phil. Mag. A **81**, 2591 (2001).

[76] L. D. Landau, E. M. Lifschitz, *Lehrbuch der theoretischen Physik, Band VII, Elastizitätstheorie*, Akademie-Verlag Berlin (1975).

[77] C. P. Flynn, *Point defects and diffusion*, Clarendon Press Oxford (1972).

[78] Cox, J. D., Wagman, D. D., and Medvedev, V. A., *CODATA Key Values for Thermodynamics*, Hemisphere Publishing Corp., New York, (1989).

[79] M. Lannoo and G. Allan, Phys. Rev. B **25** (6), 4089 (1982).

[80] M. Scheffler, J. Dabrowski, Phil. Mag. (1988).

[81] D. Morgan, A. van de Walle, G. Ceder, J.D. Althoff, and D. de Fontaine, Modelling Simul. Mater. Sci. Eng. **8**, 295 (2000).

[82] U. Gerstmann, E. Rauls, H. Overhof, Th. Frauenheim, Physica B, 308-310, 497-501, 2001.

[83] Th. Lingner, S. Greulich-Weber, J.-M. Spaeth, U. Gerstmann, E. Rauls, and H. Overhof, Physica B **308**, 625 (2001).

[84] H. Itoh, M. Yoshikawa, I. Nashiyama, S. Misawa, H. Okumura, and S. Yoshida, IEEE Trans. Nucl. Sci. **37**, 1732 (1990).

[85] V. S. Vainer and V. A. Il'in, Sov. Phys. Solid State **23**, 2126 (1981)

[86] Th. Lingner, Dissertation, Universität Paderborn, (2001).

[87] N. T. Son, P. N. Hai, M. Wagner, W. M. Chen, A. Ellison, C. Hallin, B. Monemar, E. Janzén, Semicond. Sci. Technol.**14** , 1141 (1999).

[88] N. T. Son, private communication (2003).

[89] L. Torpo, M. Marlo, T. E. M. Staab, and R.M. Nieminen, J. Phys. C **13**, 6203 (2001).

[90] K. C. Pandey, Phys. Rev. Lett. **57** (18) (1986), p. 2287.

[91] E. Rauls, A. Gali, P. Deák, and Th. Frauenheim, in Proceedings Vol., Mat. Sci. Forum (ECSCRM2002), in print.

[92] J. J. Sumakeris, L. B. Rowland, R. S. Kern, S. Tanaka, and R. F. Davis. *Thin Solid Films*, 225:219, 1993.

[93] D. G. J. Sutherland, L. J. Terminello, J. A. Carlisle, I. Jimenez, Himpsel F. J., K. M. Baines, D. K. Shuh, and W. M. Tong. *J. Appl. Phys.*, 82:3567, 1997.

[94] T. Fuyuki, T. Yoshinobu, and H. Matsunami. *Thin Solid Films*, 225:225, 1993.

[95] H. Nagasawa and Y. Yamaguchi. *Thin Solid Films*, 225:230, 1993.

[96] S. Hara, T. Meguro, Y. Aoyagi, M. Kawai, S. Misawa, E. Sakuma, and S. Yoshida. *Thin Solid Films*, 225:240, 1993.

[97] T. Lohner, Nguyen Quoc Khanh, private communication.

[98] A. Ellison, B. Magnusson, C. Hemmingsson, W. Magnusson, T. Iakimov, L. Storasta, A. Henry, N. Henelius, and E. Janzén, Mat. Res. Soc. Symp. 640, (2001), p. H1.2

[99] V. S. Ballandovich and G. N. Violina, Cryst. Lattice Defects Amorphous Mater. **13**, 189 (1987).

[100] G. Davies, S.C. Lawson, A. T. Collins, A. Mainwood, and S. J. Sharp, Phys. Rev. B **46**, 13157 (1992).

[101] A. Mainwood, Phys. Rev. B **49**, 7934 (1994).

[102] S. Greulich-Weber, phys. stat. sol. (a) **162**, 95 (1997).

[103] S. Greulich-Weber, phys. stat. sol. (b) **210**, 415 (1998).

[104] M. Laube, Erlangen, private communication (2002).

[105] T. Evans, *The properties of natural ans synthetic diamond*, ed. J.E. Field (Academic Press: London), 259 (1992).

[106] M. Laube, F. Schmid, G. Pensl, G. Wagner, M. Linnarsson, M. Maier, J. Appl. Phys. **92**, 549 (2002).

[107] A. I. Veinger, A. G. Zabrodskii, G. A. Lomakina, and E. N. Mokhov, Sov. Phys. Solid State **28**, 917 (1986).

Acknowledgment

First of all I would like to thank my thesis advisor Prof. Th. Frauenheim for his support and for allowing me to pursue my own research interests. For several advises and for writing one of the certificates for this work, I am grateful to Prof. H. Overhof.

For his interest in my work on antisites and also on surface structures, which are, though, not included in this thesis, I want to express special thanks to Prof. Peter Deák, TU Budapest, — also for his invitations to Budapest which I followed a few times. Our intensive discussions during his regular stays at Paderborn as well as during my stays at Budapest always helped keeping an eye on the correlation of our theoretical studies to experiment.

He was also the one who initiated my stay in the group of E. Janzén at Linköping, Sweden, during last spring. For interesting discussions about e. g. the annealing behavior of vacancies or the origin of the D_I center during this time and afterwards, I would like to thank Nguyen Tien Son, especially for giving me some new insight on these topics from the point of view of an experimentalist.

For providing me with reference calculations with the FHI-code or AIMPRO I would like to thank Alexander Mattausch, Universität Erlangen, who calculated the vibrational spectra cited in this work with the FHI-code, and Ádám Gali, TU Budapest, who did the same with AIMPRO and performed all other calculations of selected defect structures with the FHI-code.

For several articles we wrote together and for sharing his experience in defect physics with me, I am especially grateful to Uwe Gerstmann. He has also performed all LMTO-ASA calculations cited in this work, which e. g. helped to understand the origin of the differences between the formation and migration energies of vacancies calculated within SCC-DFTB and ab initio LDA methods.

Furthermore, I want to thank all members of the group of Th. Frauenheim and all other "inhabitants" of the N3-floor that have not been named yet. This includes Zoltán Hajnal, who provided me with the parameters for nitrogen and phosphorus, and the system administration, in the first time in person of Michael Sternberg, and in the last two years in person of Christof Köhler and Peter König, for keeping our machines in order and, thus, providing us with the necessary computing facilities.

Last but not least, my warmest thanks to my mother and to Bobby for their patience during the last years!